

ABSTRACT

SRIDHAR, KARTHIK. A Computational Study of Inhaled Droplet-Spray Formation and Subsequent Drug Transport, Deposition and Uptake in Human Nasal and Lung-Airway Models. (Under the direction of Dr. Clement Kleinstreuer).

Spray inhalers are commonly used devices to deliver medication *via* the oral and the nasal routes for the treatment of pulmonary and systemic diseases. Examples include severe asthma, chronic obstructive pulmonary disorder, allergic reactions such as rhinitis, as well as solid tumors and diabetes. Pressurized metered-dose inhalers (pMDIs) and nasal spray pumps are typical spray inhalers, employed to deliver suspended drug-droplets into oral and nasal cavities, respectively. The pMDI is characterized by a short burst of high-velocity droplets containing a propellant and the drug particles, while the nasal pumps deliver larger diameter aerosols ($> 50\mu\text{m}$).

Experimental evidence has shown that the high velocity and larger particles result in elevated drug depositions in the oral region as well as in the anterior part of the nasal cavity; thus, preventing effective treatment at diseased target sites downstream. Using the open-source software OpenFOAM (<https://openfoam.com>), the validated spray dynamics of a commercial pMDI with the subsequent transport and deposition of inhaled spray droplets were simulated and analyzed for a representative lung-airway geometry using conventional and pulsed injection methods. The novel pulsed injection method improved drug delivery to the distal airways significantly.

Drug deposition in the nasal cavity as well as dissolution in the mucus layers with absorption by the epithelium are important process results. They are useful for determining the amount of drug needed and the time taken for drug uptake to treat local as well as systemic diseases. Specifically, a customized solid particle dissolution and diffusion solver called *dissolutionTransportFoam* was

developed in OpenFOAM to study the dissolution and uptake of depositing drug particles in a realistic 3D mucus layer geometry. Realistic injection parameters of a commercial nasal spray pump were incorporated to simulate and analyze drug deposition followed by dissolution and absorption in the nasal epithelium.

Such a complete characterization of drug-aerosol sprays emanating from drug delivery devices, with subsequent transport, deposition, and dissolution of drug particles, will aid in improved drug formulation as well as realistic direct drug delivery approaches.

© Copyright 2020 by Karthik Sridhar

All Rights Reserved

A Computational Study of Inhaled Droplet-Spray Formation and Subsequent Drug Transport,
Deposition and Uptake in Human Nasal and Lung-Airway Models

by

Karthik Sridhar

A thesis submitted to the Graduate Faculty of
North Carolina State University
in partial fulfillment of the
requirements for the degree of
Master of Science

Mechanical Engineering

Raleigh, North Carolina

2020

APPROVED BY:

Dr. Alexei Saveliev

Dr. Gregory Buckner

Dr. Clement Kleinstreuer
Chair of Advisory Committee

DEDICATION

To my parents and grandparents for showering me with unconditional love and support

In loving memory of my late grandmother, Mrs. Lalitha Srinivasan

BIOGRAPHY

Karthik Sridhar was born on October 17, 1996 to Mr. Sridhar Srinivasan and Mrs. Vasanthi Sridhar in Chennai, Tamil Nadu, India. After completing his high school education, Karthik pursued a Bachelor's degree in Mechanical Engineering at SSN College of Engineering, Anna University, India and graduated in 2018. He then moved to Raleigh in 2018 to pursue a Master of Science degree in Mechanical Engineering at North Carolina State University. He will be graduating in the Fall of 2020, having conducted research under Dr. Clement Kleinstreuer.

ACKNOWLEDGMENTS

I would like to express my sincere gratitude towards my advisor, Dr. Clement Kleinstreuer, for giving me this opportunity to work in the Computational Multi-Physics Laboratory (CMPL) at North Carolina State University. His constant guidance and encouragement throughout my Master's journey have shaped me into a better researcher. His extensive knowledge of the subject and a passion for teaching have helped me gain a better understanding of fluid-particle dynamics.

I would like to thank my committee members, Dr. Alexei Saveliev and Dr. Gregory Buckner, for the time served and for graciously agreeing to supervise my defense amidst their busy schedules.

I would like to thank Sriram Chari of CMPL for giving me the opportunity to be a co-investigator on the nasal mucus layer project. The project would not have reached the publication stage if not for his research vision and inputs. I would also like to thank my other lab members, Sujal Dave, Shantanu Vacchani, Nilay Kulkarni and Adithya Gurumurthy for being excellent colleagues who were ready to help with any issue. I would like to express my gratitude to the NCSU High performance Computing group who gave me the opportunity to run simulations with many processors and for helping me navigate technical issues.

This thesis would not have been possible if not for the unconditional support from my parents. Their constant motivation helped me at various times when I hit roadblocks in the project. Last but certainly not the least, I would like to thank my roommates, Adityan Suresh and Anand Srinivasan, without whose support, I would not have been able to cross hurdles during my stay in Raleigh.

TABLE OF CONTENTS

List of Tables	vii
List of Figures	viii
1 Introduction.....	1
1.1 Background Information	1
1.2 Literature Review	4
1.2.1 Pressurized Metered Dose Inhalers.....	4
1.2.2 Application to Drug Dissolution and Nasal Mucociliary Clearance	12
1.3 Research Objectives and Justification	18
2 Mathematical Models.....	20
2.1 Airflow Equations	20
2.1.1 Navier-Stokes Equations.....	20
2.1.2 Turbulent Flow.....	22
2.1.3 Scalar Transport	27
2.2 Aerosol Dynamics.....	27
2.2.1 Particle Trajectory Equation	27
2.2.2 Turbulent Dispersion	29
2.2.3 Boiling and Evaporation of Droplets	30
2.2.4 Solid Particle Dissolution	33
2.2.5 Epithelial Absorption	34

3	Numerical Solvers and Model Validation.....	36
3.1	Introduction to OpenFOAM	36
3.2	Case Structure in OpenFOAM.....	38
3.3	Droplet Evaporation Model	49
3.4	Nasal Spray Lagrangian Particle Tracking	54
3.5	Solid Particle Dissolution Model.....	56
3.6	Drug Absorption Boundary Condition.....	60
4	Results and Discussion	65
4.1	Pressurized Metered Dose Inhaler – Ventolin	65
4.1.1	Spray Characteristics	66
4.1.2	Oral Cavity Drug Deposition.....	77
4.1.3	Pulsed Spray Injection	86
4.2	Nasal Epithelial Drug Uptake	91
4.2.1	Airway Surface Liquid Layers Mesh.....	91
4.2.2	Velocity Fields.....	92
4.2.3	Drug Dissolution and Absorption	96
4.2.4	A Basic Nasal-Spray Application Study.....	106
5	Conclusions and Future Work	113
	References.....	118

LIST OF TABLES

Table 1. Commonly used schemes for numerical discretization	47
Table 2. Commonly used iterative solvers in OpenFOAM	48
Table 3. Parameters used in the evaporation experiment	50
Table 4. Parameters used in the nasal spray computer experiment	55
Table 5. Comparison of results with the nasal spray computer experiment	55
Table 6. Parameters used in the dissolution experiment.....	57
Table 7. Parameters used in the epithelial absorption experiment.....	60
Table 8. Parameters used in the spray simulations	67
Table 9. Average droplet diameter values	70
Table 10. Droplet velocities downstream of the spray	70
Table 11. Droplet temperature near the centerline.....	75
Table 12. Comparison of the mass remaining in nasal cavity with experimental results.....	95
Table 13. Parameters used in the drug absorption simulations.....	96
Table 14. Nasal spray deposition percentages	109

LIST OF FIGURES

Figure 1. Pressurized Metered-Dose Inhaler	4
Figure 2. A metered dose inhaler spray	6
Figure 3. In vitro set up using the Alberta Idealized Throat model	11
Figure 4. Computer generated geometry of nasal cavity	13
Figure 5. Schematic of the airway surface liquid	14
Figure 6. Case structure in OpenFOAM	38
Figure 7. The different types of boundary conditions.....	42
Figure 8. Commonly used particle models in OpenFOAM.....	45
Figure 9. Evaporation of a water micron droplet.....	51
Figure 10. Evaporation of a HFA134a micron droplet.....	53
Figure 11. Computational domain for the dissolution simulation	58
Figure 12. Dissolution and permeation of Fluticasone Propionate (FP).....	59
Figure 13. Computational domain (shaded area) for the absorption simulation.....	62
Figure 14. Profile of mass of the drug permeated into the receptor with time	64
Figure 15. Computational domain for the spray characteristics study.....	67
Figure 16. Rosin-Rammler distribution functions	69
Figure 17. (a) Droplet velocity along centerline (b) Distance travelled by the spray.....	71

Figure 18. Velocity profiles in the radial direction.....	72
Figure 19. Velocity of droplets after (a) 16 ms (b) 30 ms (c) 46 ms (d) 60 ms.....	73
Figure 20. Recirculatory airflow at 15 mm inside the mouthpiece.....	74
Figure 21. Temperature profiles in the radial direction	76
Figure 22. Temperature distribution at 60 ms.....	77
Figure 23. 3D computational model of the oral cavity	78
Figure 24. Inhalation waveforms	79
Figure 25. Origin and the orientation of the spray	79
Figure 26. Comparison of the drug deposition between simulations and <i>in vitro</i> study	81
Figure 27. Velocity fields for a) 30 LPM b) 60 LPM.....	82
Figure 28. Deposition pattern for a) 30 LPM b) 60 LPM.....	83
Figure 29. Segments in the oral cavity geometry	83
Figure 30. Segmental deposition of the drug in the oral cavity	84
Figure 31. Temperature of deposited aerosol for a) 30 LPM b) 60 LPM.....	85
Figure 32. Segmental variation of temperature of deposited aerosol in the oral cavity	86
Figure 33. Comparison of lung deposition fractions of drug with pulsed injection	88
Figure 34. Segmental temperature of aerosol with 4 injections for a) 30 LPM b) 60 LPM..	89
Figure 35. Segmental temperature of aerosol with 8 injections for a) 30 LPM b) 60 LPM..	90

Figure 36. a) Airway surface liquid lining around the nostrils b) Magnified section.....	92
Figure 37. Wall-driven velocity vectors in the posterior region.....	92
Figure 38. The different segments on the nasal cavity slice.....	93
Figure 39. Axial variation of velocity for the segments in a) right and b) left cavity	94
Figure 40. Validation of the nasal mucus layer velocity field	95
Figure 41. Effect of partition coefficient on the drug uptake	97
Figure 42. Temporal evolution of the drug on the epithelial surface.....	99
Figure 43. Concentration profiles in the segments on the chosen slice for $k_{ow} = 0.005$	100
Figure 44. Concentration profiles in the segments on the chosen slice for $k_{ow} = 2$	101
Figure 45. Mass flux at the epithelium for partition coefficients a) 2 b) 0.005	102
Figure 46. Evolution of concentration within the first 10 minutes for $k_{ow} = 2$	103
Figure 47. Effect of solubility on the drug uptake	104
Figure 48. Mass flux for the partition coefficient of 0.005 and solubility 0.2 mg/ml	104
Figure 49. Effect of particle size on the rate of uptake.....	105
Figure 50. Diameter distribution of droplets from Flonase at 15 mm from nozzle	107
Figure 51. Diameter distribution of particles with angle a) 65° b) 45° in sagittal plane.....	109
Figure 52. Fluticasone Propionate uptake using realistic deposition sites and diameters	111

CHAPTER 1: INTRODUCTION

1.1 Background Information

Respiratory diseases such as asthma, chronic obstructive pulmonary disorder (COPD) and cystic fibrosis are affecting a large number of the human population each year. Studies of the causes of these ailments and possible treatments have been important topics of scientific research for decades. Such respiratory diseases can be genetic, but may also result from adverse interactions between airborne toxic pollutants and the human respiratory system (1). Excessive mucus secretion and obstruction of airways are common symptoms of these diseases.

Treatment for respiratory diseases can involve administration of drugs either orally or parenterally. However, such treatment relies on systemic circulation of the drug to reach the diseased lung site, often in very low concentrations. In contrast, the pulmonary delivery, which involves inhalation of therapeutic aerosols, offers several advantages (2, 3). The pulmonary route offers a 'needle-free' approach that ensures that a high concentration of drug is delivered to the diseased site inside the lungs, thereby reducing the amount of drug required for maximum therapeutic effectiveness. This is especially useful for drugs with lower gastrointestinal absorption (3). Another potential benefit of pulmonary administration of drugs is that the lungs boast a large surface area which could be used for absorption of dissolved drug particles into the blood stream through the epithelial cell barrier for treating a diseased site located somewhere else (2).

Inhalers are used for alleviating the symptoms of respiratory diseases. Among the different types of treatment devices, spray inhalers are quite commonly used as they are typically hand-held devices and hence portable. Depending on the disease or the allergic reaction being treated, spray inhalers can be used to deliver medication in the oral or the nasal cavity. For instance, pressurized

metered dose inhalers (pMDI) are used to spray liquid aerosols into the oral cavity for treating asthma or COPD (4), while nasal spray pumps are used to spray drug suspended droplets in the nasal cavity for treating rhinitis or sinusitis (5). Complex aerodynamic and heat transfer processes govern the aerosolization of the drug solution or suspension as the evolving spray leaves the nozzle. These devices spray polydisperse droplets at a high velocity which then traverse the tortuous path inside the nasal cavity or lung airways.

When particles are released into the airstream such as during passive inhalation of pollutants, they deposit by different mechanisms in the lung; specifically *via* impaction, interception, sedimentation and diffusion, largely depending on the aerodynamic diameter (6). Particles with diameters greater than 5 μm deposit in the bronchial regions in the upper airways by impaction. Sedimentation is the process by which particles with diameters between 1 μm and 5 μm settle due to dominant gravitational forces. Nanoparticles, which have diameters less than 1 μm deposit mainly *via* diffusion, where the particles collide with the molecules in the air due to Brownian motion. Interception generally results in particle deposition in the smaller airways when the pathlines move very close to the airway walls. Spray inhalers are typically characterized by a short burst of high-velocity droplets or solid particles (7). In such cases, the velocity of the particles together with their size govern the mechanisms of deposition in the lungs.

Understanding local drug depositions and related particle-release maps are important for direct drug delivery (8, 9). Once the aerosols deposit on the walls, they may dissolve and be absorbed into the epithelium. For example, the human nasal cavity offers a highly vascularized epithelial layer and blood flow with a relatively thin and porous endothelial membrane (10). This makes the nasal cavity highly suitable for topical as well as systemic treatment of diseases (11). The study of drug dissolution in the mucus layers and absorption into the epithelium helps in understanding the

time it takes for the maximum amount of drug to be available at the target sites. The data from such a study can be used as input for more comprehensive systemic drug transport simulations, using detailed pharmacokinetic models.

Accurate description of the mass of the drug that deposits, the deposition locations inside the lung airways and the proportion of the drug absorbed by the epithelium all aid in effective disease treatments as well as design improvements of inhalers and drug formulations. Generation of such data sets is traditionally accomplished by conducting experiments with realistic (or idealistic) casts of the lung airways, commercially available inhalers, and cell cultures. In some cases, experiments are performed on human volunteers using radiolabeled aerosols to identify regions of deposition. However, such *in vitro* and *in vivo* experiments may pose a health risk and are cumbersome and expensive to conduct. In contrast, mathematical modeling, and computer simulations, ie, *in silico* approaches, is a valuable alternative, being relatively inexpensive and have the potential to provide more insight into the transport and conversion phenomena. Using such computational tools, spatial and temporal predictions of the various processes including initial spray-droplet formation, deposition, dissolution, and absorption in the human cell layers can be made (12).

In this work, an open-source computational fluid dynamics software, OpenFOAM, was employed with customized solvers and boundary conditions to simulate the spray of aerosols emitted from Ventolin (GlaxoSmithKline), a commercial pressurized metered dose inhaler (pMDI), and subsequently deposited in a representative oral cavity model. A second application is a nasal spray simulation, followed by the dissolution and absorption of a generic drug across the nasal epithelial cell layer using customized solver, *dissolutionTransportFoam*, and the coded absorption boundary condition.

1.2 Literature Review

1.2.1 Pressurized Metered Dose Inhalers

Among the many inhalers that deliver medication through the oral cavity, the pMDIs are the most widely used. Introduced in 1956 by Riker Laboratories Inc. (now 3M Drug Delivery Systems), the pMDI is a portable and convenient device for treating various respiratory diseases such as asthma and COPD (13). A thorough understanding of the operation and droplet-spray formation is necessary to gain realistic oral inlet conditions and to bring about device improvements in the future. Various authors have studied the characteristics of pMDI-sprays and subsequent depositions using experimental and computational techniques. Previous work has shown that while the general principles of operation remain the same, devices produced by different manufacturers can have large variations in the spray parameters such as droplet diameter and velocity (14, 15).

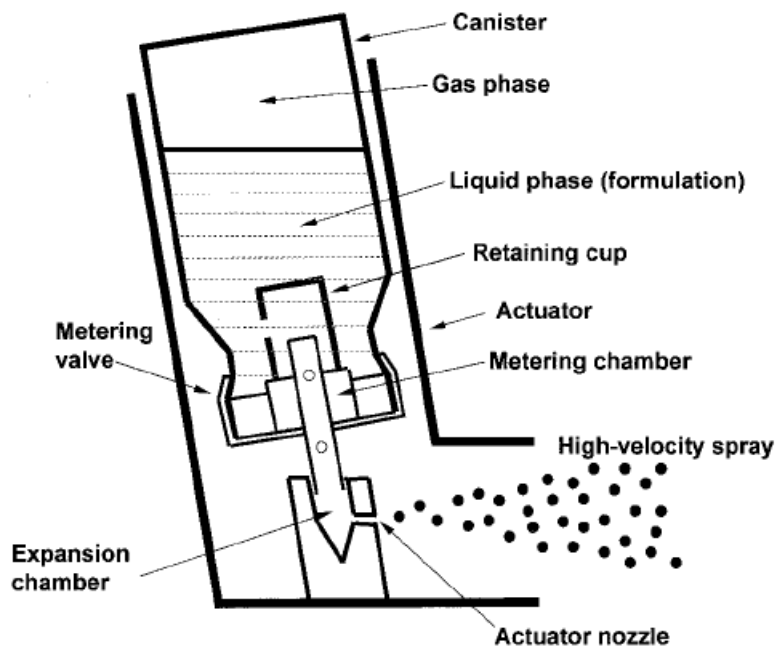


Figure 1. Pressurized Metered-Dose Inhaler (4)

A schematic of the pMDI is shown in Figure 1. The drug formulation, which consists of the drug, propellant, surfactant, and other excipients is maintained under pressure inside the canister. The high pressure ensures that the propellant, which has a very low boiling point, does not vaporize. A fixed dose of the drug formulation is administered during each actuation with the help of the metering valve. When the inhaler is actuated, the fixed volume of the drug formulation enters the expansion chamber through the metering valve. The expansion chamber is maintained at atmospheric pressure and hence the drug formulation which was earlier in the sub-cooled state becomes superheated. This flash boiling process results in pockets of vapor bubble being continuously formed and destroyed and the resulting two-phase flow is accelerated through the nozzle orifice (16).

For long, Chlorofluorocarbons (CFC) had been the choice for the propellant. However, adverse environmental effect of CFCs led to the search for another suitable propellant. Today, Hydrofluoroalkanes (HFA) namely, HFA-134a and HFA-227, are the widely used propellant for the manufacturing of pMDIs. HFA-134a has a very low boiling point (245 K) which makes it suitable to atomize via flash boiling in the expansion chamber when the pressure drops to normal levels. There are two types of drug formulations, ie, solution and suspension formulation (17). The solution formulation is prepared by completely dissolving the drug in the propellant. Typically, ethanol is used to increase the drug solubility in the propellant and this addition of a cosolvent influences the characteristics of the spray. A suspension formulation is prepared when the drug is available in the solid state and it is crushed to form micronized powder, which is then suspended in the propellant. The propellant droplets, after atomization, may contain any number of suspended solid drug particles.

Droplet Size and Velocity

The characteristics of a spray, such as the droplet sizes, velocities, plume shape and temperature, have been analyzed and reported by various researchers. Techniques employed range from simple high-speed video recording to the more sophisticated Phase Doppler Anemometry (PDA). Barry and O'Callaghan (18) used high-speed video recording at a high frame rate to study the distance travelled by the aerosol plume (see Figure 2), the speed of the plume front and the volume of the cloud from two different pMDIs. They argued that such an analysis should be used to design the spacers that are the currently used add-ons to reduce the speed of the aerosol spray. Crosland et al. (19) used particle image velocimetry (PIV) to obtain planar velocity measurements for commercially available pMDIs. They observed that the axial velocity was the maximum at the centerline of the spray which then decreases downstream as the spray decelerates. The authors also noted temporal variations in the spray geometry and the velocity with the flow exhibiting two velocity peaks over time.



Figure 2. A metered dose inhaler spray (18)

Smyth et al. (20) investigated the geometry of the spray cross-section and was the first to report droplet sizes at different locations along the length of the spray. They observed that the cross-section of the spray was predominantly elliptical in the vertical direction and the droplets reduced in size downstream due to evaporation, especially for smaller droplets occurring at the edges. Liu

et al. (15) studied the centerline droplet velocities, diameters and the impaction force of a comprehensive list of commercially available inhalers using phase doppler anemometry (PDA). In particular, they noted that Ventolin HFA (GlaxoSmithKline) displayed an 8% decrease in the centerline velocity between 3 cm and 6 cm along the length of the spray. The arithmetic mean diameter (D10) was found to be $4 \mu\text{m}$ at 3 cm. A more recent study by Alatrash and Matida (21) found that the centerline velocity of droplets from Ventolin HFA exhibited a 70% decrease between the location of the mouthpiece and 75 mm in front of it. Additionally, the authors also observed that the Rosin-Rammler distribution (18) better fits the droplet sizes characterized at the location of the mouthpiece with a mean diameter of $4 \mu\text{m}$ for Ventolin HFA inhaler. While these studies reported the characteristics of the spray downstream from the mouthpiece exit (typically beyond 25 mm from position of the nozzle orifice), Wigley et al. (22) managed to successfully obtain the diameter and velocity distributions of the droplets at 3 mm from the nozzle orifice. Similar to the observations of Crosland et al. (19), the authors also noted the bimodal peak in droplet velocity. Clark (23) attributed the initial spike in the velocity to the production of subsonic, two-phase mixture of the propellant inside the expansion chamber and the subsequent decrease to the choking of the flow due to the mass imbalance created between the incoming liquid-rich and outgoing vapor-rich propellant mixture.

The complex nature of the flow and the difficulty in obtaining data pertaining to the flow of the propellant mixture inside the expansion chamber has limited the use of numerical models to predict droplet sizes and velocity. Successful efforts include the studies conducted by Gavtash et al. (24, 25) in which the authors used two-phase flow and atomization models to numerically predict the velocity and size of the droplets, respectively. The authors observed that the Homogenous Flow Model (HFM), which assumes no mass transfer between the liquid and the vapor phases, matched

the experimental data for near orifice droplet velocity measurements better than the other models. Using the velocity predicted by HFM and the linear instability sheet analysis (LISA) atomization model, the authors further attempted to predict the temporal variation in the sizes of the droplets produced using two models of internal flow (annular and core) of the propellant mixture. The numerically predicted sizes agree with experimental data to an extent for near-orifice droplets. Clearly, more information about the nature of the complex two-phase flow dynamics is required in order to develop a more robust model.

Plume Temperature

The atomization of the drug formulation into smaller droplets relies on flash boiling of the propellant mixture inside the expansion chamber. The low boiling point of the HFA propellant at atmospheric pressure (at 245 K) and the wet bulb temperature (211 K), which is the lowest equilibrium temperature of the propellant, helps in achieving the required degree of atomization as well as the high velocity of the droplets. However, apart from the high deposition in the throat region, the low temperature of the impacting aerosols results in the ‘cold-freon’ effect which makes patients feel uncomfortable (14). The evaporation of the HFA droplet has been characterized both theoretically and experimentally (26, 27). For example, Gabrio et al. (14) evaluated the temperature of the plume in the air of 28 commercially available inhalers along the centerline, starting at 5 cm from the mouthpiece exit. The investigated products included bronchodilators, steroids, and nasal inhalers, which contained both HFA and CFC as propellants. In general, the authors noted that the HFA products resulted in warmer and softer spray plumes. In particular, the temperature reported for the Ventolin HFA product was 244 K. However, in a more recent study, Brambilla et al. (28) analyzed the temperatures of both commercial and placebo pMDI

formulations inside a tubular geometry and found that the values follow the order: HFA suspension < CFC suspension < HFA solution, with CFC suspension formulation temperatures higher than the HFA products due to its higher boiling point. The HFA solution formulations generally contain ethanol which increases the boiling point of the mixture. Hence, with increasing ethanol content the authors observed an increase in the temperature of the plume. Gavtash et al. (29) simulated the spray evolving from the pMDI orifice and plotted the temperature of the droplets along the centerline, although no validation with experimental data was provided.

Spray Angle

Another important parameter of a spray is its angle. The wider the spray, the higher is the deposition of aerosols in the throat segment which, in most cases, will not be the desired target. The angle of the spray is controlled by geometrical aspects of the nozzle and the fluid dynamic processes inside the expansion chamber. Chen et al. (30) investigated the effects of both nozzle shape and the addition of a co-solvent, such as ethanol, on the plume angle. They observed that a flat inner surface of the nozzle resulted in a larger spray angle while the addition of ethanol decreased the spray angle due to the lower vapor pressure of the evaporating droplets. In general, for a pMDI formulation without ethanol, the spray angle was found to be between 10° and 15°. Moraga-Espinoza et al. (31) noted that the addition of airflow resulted in a narrower spray when compared to no-airflow conditions. This helps in understanding the changes in the plume characteristics inside the oral cavity during inhalation.

Aerosol Deposition

Various researchers have experimentally studied the deposition of aerosols emanating from pMDIs, with and without spacers. A common observation is the high deposition in the oropharynx which reduces the effectiveness of the inhaled drugs. Newman et al. (32) conducted *in vivo* studies to estimate the mass of drug deposited in the lungs of ten healthy volunteers. They observed that the absence of a spacer add-on resulted in a mere 11% deposition in the lungs while its addition yielded an increase of 5%. One of the early *in vitro* studies conducted by Swift et al. (33) involved the spraying of pMDI aerosols into an oropharyngeal model and subsequently sized by a cascade impactor. They found that, with increasing inspiratory flow rates, the mass of drug penetrating the oropharyngeal segment increased, contrary to the observation of higher oropharyngeal deposition due to impaction in experiments involving passive inspiration. The authors attributed this finding to the greater possibility of mixing of aerosols with the air stream. Cheng et al. (34) compared the deposition pattern of pMDIs with HFA and CFC as propellants in a more realistic cast of the oral cavity. The pMDI with HFA as the propellant resulted in a higher lung deposition (24 %) compared to the CFC based inhaler (16%) due to a lower initial spray velocity and droplet sizes. The authors also observed that a smaller orifice diameter produced a softer plume as reported by others (14), resulting in lower oropharyngeal deposition. In contrast, Zhang et al. (35) noted that the commercial inhaler QVAR yielded a 30% deposition in an *in vitro* mouth-throat model, indicating that the deposition in the lungs would be comparatively higher. A possible explanation for this is that QVAR has a smaller orifice diameter (28) and a longer spray duration, i.e. over 270 ms, which reduce the aerosol impact force (14). The inhalation flowrate during normal breathing does not remain constant but rather exhibits an acceleration and a deceleration phase. The time of actuation of the pMDI during the inhalation cycle is therefore an important parameter to study as it influences

the relative velocity between the flow and the spray. Biswas et al. (36) used the Alberta Idealized Throat model (see Figure 3) and observed that higher flow rates, i.e. 60-90 L/min. It resulted in greater *in vitro* lung deposition (> 40%) when the Ventolin pMDI was actuated in the first half of the inhalation, which was approximated using trapezoidal waveforms. A higher peak flow rate and actuation during the acceleration phase of inhalation lowers the relative velocity between the flow and the spray which helps in reducing recirculatory flow of aerosols and in guiding the drug droplets or solid particles to the distal regions of the lungs.

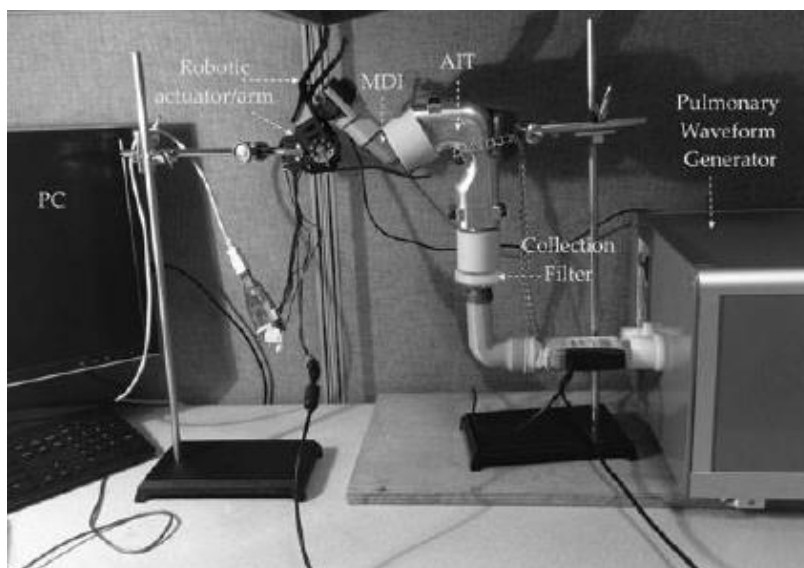


Figure 3. In vitro set up using the Alberta Idealized Throat model (36)

As mentioned, the presence of a co-solvent such as ethanol can influence the characteristics of a spray (28, 37) and hence lung deposition. Gupta et al. (38) studied the effect of increasing concentrations of ethanol on the deposition in a simple *in vitro* USP throat model. They noticed that the presence of the cosolvent increased deposition in the throat segment and hence reduced deposition in the lungs as the addition of ethanol retards the evaporation rate of the propellant mixture and produces larger droplets which deposit by impaction.

Numerous articles describe the efforts taken to predict the deposition of pMDI aerosols in the lung airways using CFD. Kleinstreuer et al. (8) compared the deposition of aerosols from inhalers using HFA and CFC as propellants in a human upper airway model. The authors found that the use of HFA, smaller orifices and spacers generate smaller droplets and hence improves aerosol penetration into the lower airways (74.5%). The computational study included validated models for breakup and evaporation of the droplets post exiting the orifice. Yousefi et al. (39) conducted one-way coupled simulations of pMDI-spray in an upper airway model and noted that the deposition of aerosols was sensitive to changes in the spray-cone angle, injection velocity and the initial particle size distribution. Their results showed that the change in spray-cone angle resulted in the greatest change in deposition; for example, the oropharyngeal deposition reduced by more than 20% as the angle increased from 2° to 10°. Delvadia et al. (40) analyzed the effect of inhaler insertion angle on the deposition of aerosols emitted from a metered dose inhaler and validated their results with *in vitro* data.

1.2.2. Application to Drug Dissolution and Nasal Mucociliary Clearance

Inhaled medication has to travel through tortuous paths inside the nasal cavity before depositing onto the mucus layer. The conditions for the subsequent transport, dissolution and absorption is not the same across the entire nasal cavity. Typically, the nasal cavity can be divided into three major segments, i.e. the nasal vestibule, posterior region, and olfactory bulb (see Figure 4).



Figure 4. Computer generated geometry of nasal cavity

The airway surfaces of the nasal cavities are lined with two liquid layers (see Figure 5) (41). The first layer, which is in direct contact with the epithelial cells, is the watery periciliary sol layer. This layer houses a mesh of cilia which are 5 to 10 μm long and 250 nm thick (42). The second layer on top of the periciliary sol layer is the gel-like mucus layer which contains water (90%) and proteins. The low viscosity of the sol layer allows the free movement of the cilia, which beating in unison move the mucus layer away from the nostril at a velocity of 2 – 25 mm/min (42). The high viscosity of the mucus layer helps in trapping foreign particles and the coordinated strokes of the cilia transport them to the mouth (41).

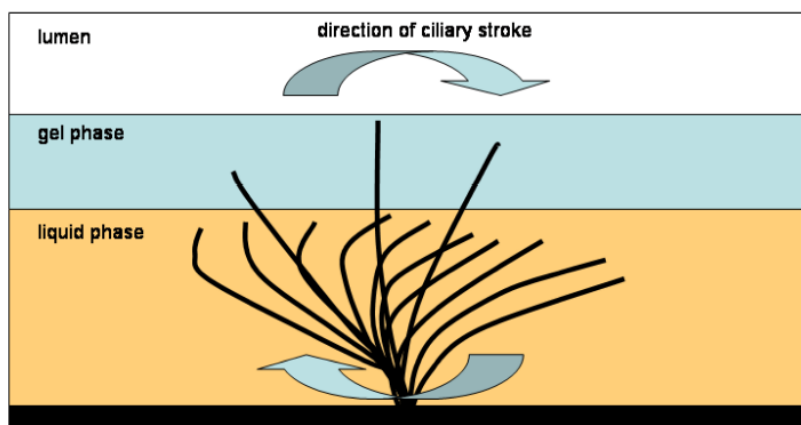


Figure 5. Schematic of the airway surface liquid (42)

The nasal vestibule surface is covered by keratinized and stratified squamous epithelial cells (43). The keratin coating prevents the effective absorption of the drugs in the anterior region of the nasal cavity. Cilia are absent in this region and hence mucociliary clearance is not effective (10). The posterior region contains cilia and columnar epithelial cells. One in every five columnar cells is a goblet cell which secretes mucins and replenishes the mucous blanket above the cilia (41). The olfactory region contains cilia but not goblet cells and hence contributes to ciliary clearance but does not secrete mucus (44).

The nasal cavity offers the advantage of providing both topical and systemic treatment with minimal side effects. However, before the drug is available for systemic circulation, it has to dissolve in the mucus layer, diffuse and cross the epithelial barrier (45). The epithelium contains lipids, as opposed to the aqueous mucus layer, and hence facilitates the absorption of lipophilic (lipid-loving) drugs more than the hydrophilic (water-loving) drugs. A higher solubility for the drug ensures that dissolution is completed well before the cilia can propel the trapped particles towards the mouth.

Drug Dissolution

The first point of entry for the drug into the systemic circulation is the gel-like mucus layer. The high viscosity of the mucus makes it difficult for the particles penetrate further. Hence, the drug particle needs to rely on dissolution to break down and be advected through the layers of the airway surface liquid. Several authors have experimentally studied the dissolution of solid drug particles in a limited volume of fluid to establish the mucus environment. The subsequent permeation of the dissolved drug through a porous membrane helps to understand the time the drug takes to dissolve and diffuse through the medium. Clearly, a drug with high solubility will dissolve and diffuse faster than a drug with a low solubility. In the human nasal mucus layer, the high solubility can help to escape mucociliary clearance.

Arora et al. (46) conducted an *in vitro* study to assess the kinetics of respirable aerosol drug particles such as Flunisolide (FN), Budesonide (BD) and Fluticasone Propionate (FP) produced from inhalers. The particles collected from the Andersen cascade impactor had sizes in the ranges of 2.1 – 3.3 μm and 4.7 – 5.8 μm . Additionally, the authors conducted similar diffusion tests using a solution of a pre-dissolved drug. FN exhibited the fastest dissolution and diffusion in Phosphate Buffered Saline (PBS) due to its high solubility, with the total mass permeated nearly 100%. In particular, the mass transported profiles looked indistinguishable for FN particles and solution, indicating that the dissolution of FN occurs spontaneously without any regard to the limited fluid volume. FP dissolved very slowly due to the low solubility, with the total mass permeated reaching only 2% at the end of 5 hours. The authors also found that the smaller particles dissolved and diffused faster than larger particles due to a higher surface area per weight.

Rohrschneider et al. (47) assessed the dissolution behavior of orally inhaled drug products such as Ciclesonide, Budesonide and Fluticasone Propionate (FP) in a medium containing PBS and 0.5%

SDS. Among the drugs studied, Budesonide exhibited the highest rate of mass transportation, followed by FP, which was later confirmed by another study as well (48). The authors also conducted a study in a medium containing only PBS i.e. without the surfactant, and found that the dissolution process became very slow for FP. Although SDS is not generally used as a biological surfactant, the results indicate that the addition of a surfactant has the potential to affect the dissolution behavior drastically and that it should be considered in future studies.

Drug Absorption

The drug particle, after dissolution, encounters the epithelial barrier. The epithelium has a high affinity for the lipid phase and hence favors the transport of lipophilic drug more than a hydrophilic drug. The lipophilicity or the hydrophilicity of a drug is described by the octanol/water partition coefficient (k_{ow} or P). It represents the ratio of the concentration of a substance in the lipid and aqueous phases respectively at equilibrium. Log P values are typically between -3 (very hydrophilic) and +10 (very lipophilic) (49). While it is difficult to obtain *in vivo* data, numerous authors have conducted *in vitro* studies using epithelial cell monolayers cultured on a membrane.

Bur et al. (50) studied the uptake of Budesonide and Salbutamol Sulfate across the Calu-3 epithelial cell monolayer. Budesonide is more lipophilic than Salbutamol Sulfate but the former is less soluble than the latter. Due to the higher lipophilicity, Budesonide exhibits a faster absorption rate, with the mass transported reaching over 20% at the end of 4 hours. Additionally, the authors evaluated the effect of the volume of the dissolution medium on the rate of mass transport. They noticed that the rate of mass transport decreased as the volume for dissolution increased from 3.4 μl and settled at a constant value as the volume reached 12.5 μl . However, the mass permeated

in this study was lower than the reported values in the dissolution studies described in the previous section. The reason is the extra resistance to mass transfer due to the epithelial cell layer. Thus, these values are expected to provide a better picture of the *in vivo* scenario. In a similar manner, Sadler et al. (45) analyzed the deposition, dissolution and absorption behavior of Salmeterol Xinafoate using an epithelial cell monolayer. The particles which deposited on stage 3 of the Andersen cascade impactor were used for the absorption studies. The dissolution happened in a limited volume (3.4 μ l) of fluid and the dissolved drug permeated across the cell layer and into the receptor compartment. The authors noted a steep increase in the mass of the drug transported in the first 5 minutes owing to the high lipophilicity of the drug, followed by a plateau at around 70% because of equilibrium in concentration. Hagi et al. (51) assessed the absorption profiles of Salbutamol Sulfate, a highly soluble (250 mg/ml) and a highly hydrophilic ($\log P = -1.58$) drug. The mass transported reached around 60% at the end of 4 hours and the percentage uptake remained constant for varying values of mass of the drug deposited indicating that permeation, and not dissolution, was the rate-limiting step.

Very few articles describe efforts made to model the drug absorption process using computational resources, which make it an important problem to analyze. Longest et al. (52) first attempted to model the uptake process on a surface mesh generated by cutting open the nasal cavity. A perfect sink condition was imposed at the epithelial interface in the posterior region indicating that the drug reaching the interface will be taken up instantly and the mucus injection was modeled using an adjusted mass source in the domain. The authors validated the dissolution model and translated the positions of the particles from the nasal cavity to the surface mesh before the start of the simulation. The results showed a sharp increase in the uptake in the first 5 minutes followed by a gradual increase in the concentration. The authors concluded that the drug from the nasal vestibule

region needed to be pulled into the posterior region for them to be taken up and hence a greater inter-subject variability can be expected. Additionally, an increase in the velocity of the mucus layer resulted in a greater rate absorption. In another study, Longest et al. (53) improved the uptake prediction by employing a robin boundary condition which includes the octanol/water partition coefficient. The authors studied the effect of particle size and solubility on the cumulative drug uptake at the epithelial interface and observed that the smaller particles with a higher solubility and a higher partition coefficient resulted in faster absorption compared to the other cases.

1.3 Research Objectives and Justification

As indicated in the literature review, a realistic and accurate computational description of droplet sprays from, say pMDIs or nasal spray pumps is lacking. Hence, a comprehensive computer simulation model which includes the spray characteristics, as well as the deposition, dissolution, and absorption of aerosols from the airway walls is necessary to provide useful insight into the operational aspects of the device. A predictive tool can aid in direct drug delivery as well as in the design and development of spray inhalers and drug formulations. Such a computational study is the focus of this thesis of which the major research objectives are listed below.

Spatial Description of pMDI Sprays

Although it is difficult to provide a general picture of any pMDI spray because of its dependence on inhaler-specific parameters, an effort was made to simulate the spray of Ventolin (GSK), a commercial inhaler. Using the droplet size and velocity obtained from the literature as initial

conditions, the spatial variations of droplet diameter, velocity, and temperature in the plume due to evaporation of the propellant were analyzed.

Pulsed Injection Technique

After validating the spray characteristics with available experimental data, the deposition in an oral upper airway geometry was analyzed. As observed from the literature, the aerosol penetration into the lungs for pMDI is well below 50%. Given the constraints of formulation dependent spray parameters, a realistic method of pulsed injection was simulated, where the spray is broken up into pulses of shorter duration with a time delay in-between. As a result, a maximum increase of 20% in lung deposition was achieved. Such an operational technique can help in improving Ventolin as well as other inhalers, given the appropriate set of initial conditions for the inhaled aerosols.

Dissolution and Absorption of Inhaled Aerosol Particles

As noted in the previous sections, the drug particles dissolve and are absorbed into the epithelium for topical and systemic treatment. For the first time, the dissolution and absorption of solid drug particles was simulated using a customized solver in C++ as part of the open source CFD software, OpenFOAM. Considering a representative 3D nasal mucus layer geometry, the Robin boundary condition was enforced to simulate the uptake of drug at the epithelium, while a wall-driven and a normal velocity was imposed to account for the mucus movement and secretion respectively. The effect of octanol/water partition coefficient, particle size and solubility were analyzed. Realistic injection parameters were used to simulate the nasal spray deposition and the actual deposition sites were used to analyze the dissolution and absorption across the cell layers.

CHAPTER 2: MATHEMATICAL MODELS

2.1. Airflow Equations

2.1.1. Navier-Stokes Equations

Fluid flow problems are generally described using a set of non-linear partial differential equations called the System of Navier-Stokes Equations. They describe the conservation of mass, momentum, and energy for flow of fluids with constant properties.

Continuity

$$\frac{\partial \rho}{\partial t} + \frac{\partial}{\partial x_i} (\rho u_i) = 0 \quad (2.1)$$

Here, u_i represents the components of the velocity and ρ is the density of the fluid. The continuity equation (see Equation 2.1) ensures the conservation of mass when the fluid moves. It states that the difference between the rates of mass entering and the mass leaving the control volume is always equal rate of accumulation or reduction of the mass inside the control volume.

Momentum

$$\frac{\partial(\rho u_j)}{\partial t} + \frac{\partial}{\partial x_i} (\rho u_i u_j) = -\frac{\partial p}{\partial x} + \mu \frac{\partial}{\partial x_i} \left(\frac{\partial u_j}{\partial x_i} \right) + \frac{1}{3} \mu \left(\frac{\partial}{\partial x_j} \left(\frac{\partial u_i}{\partial x_i} \right) \right) + \rho \vec{g} \quad (2.2)$$

Here, p is the pressure, μ is the laminar dynamic viscosity, \vec{g} is the gravitation acceleration. The Equation 2.2 is used to describe the momentum of the fluid in the X, Y and Z Cartesian directions. This set of equations encapsulate Newton's 2nd law of motion which states that the sum of all the external unbalanced forces is always equal to the product of mass and acceleration. Here, the forces considered are the pressure gradient, the viscous forces, and the force of gravity.

Energy

$$\frac{\partial(\rho E)}{\partial t} + \frac{\partial(\rho E + p)u_j}{\partial x_j} + \frac{\partial q_j}{\partial x_j} = 0 \quad (2.3)$$

Here, E is the internal energy, q_j is the external heat supplied. Equation 2.3 deals with the conservation of energy for a fluid. In simpler terms, it states that the sum of external heat added, and the work done on the fluid is always equal to the increase in the internal energy. The effect of viscous heating is considered negligible and hence has been ignored in Equation 2.3.

As described in their extended forms, the Navier-Stokes equations can be applied for both compressible and incompressible flows. Most sprays are highly subsonic flows and hence the assumption of incompressibility is valid. For an incompressible fluid, they simplify to the forms given Equations 2.4-2.6. The spray particles have very high velocity and hence, there is transfer of momentum from the particles to the gaseous phase which is accounted for by M_p . Here, ν is the kinematic viscosity.

$$\frac{\partial u_i}{\partial x_i} = 0 \quad (2.4)$$

$$\frac{\partial(u_j)}{\partial t} + \frac{\partial}{\partial x_i}(u_i u_j) = -\frac{1}{\rho} \frac{\partial p}{\partial x} + \nu \frac{\partial}{\partial x_i} \left(\frac{\partial u_j}{\partial x_i} \right) + \vec{g} + \frac{M_p}{\rho} \quad (2.5)$$

$$\rho \frac{DE}{Dt} + \frac{\partial q_j}{\partial x_j} = 0 \quad (2.6)$$

2.1.2. Turbulent Flow

Smooth layers of fluid flowing in an ordered fashion characterize laminar flow. However, when the flow transitions to the turbulent regime, chaotic fluctuations in the pressure and velocity start increasing which results in the formation of eddies. The onset of turbulence can be predicted using a non-dimensional parameter called the Reynolds number which gives the relative dominance of the inertial forces over the viscous forces. The value for transition to the turbulent regime in a pipe is 2300, while it is 5×10^5 for a flat plate. The Navier-Stokes momentum equations described in Equations 2.2-2.4 are applicable for laminar flow. Following the Reynolds decomposition, in the turbulent regime the instantaneous velocity $u = \bar{u} + u'$, being the sum of a time-smoothed velocity component and a fluctuating component to describe the turbulence effect. The momentum equations are modified as shown in Equation 2.7, which are known as the Reynolds Averaged Navier Stokes (RANS) equations.

$$\begin{aligned}
& \frac{\partial(\rho\bar{u}_j)}{\partial t} + \frac{\partial}{\partial x_i}(\rho\bar{u}_i\bar{u}_j) \tag{2.7} \\
& = -\frac{\partial p}{\partial x} + \mu \frac{\partial}{\partial x_i} \left(\frac{\partial \bar{u}_j}{\partial x_i} \right) + \frac{1}{3} \mu \left(\frac{\partial}{\partial x} \left(\frac{\partial \bar{u}_i}{\partial x_i} \right) \right) + \rho g_x \\
& \quad - \frac{\partial(\rho\overline{u'_i u'_j})}{\partial x_i}
\end{aligned}$$

The terms involving the mean component of the velocity are similar in appearance to those in the laminar flow equations. However, the term $\rho\overline{u'_i u'_j}$, called the apparent, or Reynolds, stresses introduces additional constraints for solving the problem. Joseph Valentin Boussinesq introduced in XYZ the concept of turbulent kinematic viscosity to model the Reynolds stresses and find a closure for this problem. According to Boussinesq, the Reynolds stresses can be modeled as given in Equation 2.8.

$$-\overline{u'_i u'_j} = \nu_t \left(\frac{\partial \bar{v}_i}{\partial x_j} + \frac{\partial \bar{v}_j}{\partial x_i} \right) - \frac{2}{3} k \delta_{ij} \tag{2.8}$$

Here ν_t is the turbulent kinematic viscosity, δ_{ij} is the Kronecker delta and $k = \frac{1}{2} \overline{u'_i u'_j}$ is the turbulence kinetic energy. To compute the value of ν_t , various researchers have formulated different turbulence models. The most prominent ones are the *k-epsilon*, *k-omega* and the *k-omega SST* models and they are described in this chapter. Zhang and Kleinstreuer (54) have compared the various models available for simulating turbulence with respect to airflow and nanoparticle deposition in the oral airway.

***k-epsilon* model**

The *k-epsilon* model is the most popularly used model to simulate turbulent flow, especially recirculating flows, and planar shear layers. This model relies heavily on the use of wall functions to obtain the flow field near the wall in the viscous sublayer and hence a coarser mesh will suffice. Zhang and Kleinstreuer (55) found that this model fails to capture the laminar flow behavior at low Reynolds Numbers. It attempts to solve two transport equations: one for the turbulent kinetic energy (k) and one for the rate of dissipation of turbulent kinetic energy (ε) as shown in Equations 2.9 and 2.10. The turbulent kinematic viscosity is then computed as shown in Equation 2.11.

$$\frac{\partial(\rho k)}{\partial t} + \frac{\partial(\rho k u_i)}{\partial x_i} = \frac{\partial}{\partial x_j} \left[\left(\mu + \frac{\mu_t}{\sigma_k} \right) \frac{\partial k}{\partial x_j} \right] + P_k + P_b - \rho \varepsilon - Y_M + S_k \quad (2.9)$$

$$\begin{aligned} \frac{\partial(\rho \varepsilon)}{\partial t} + \frac{\partial(\rho \varepsilon u_i)}{\partial x_i} & \quad (2.10) \\ & = \frac{\partial}{\partial x_j} \left[\left(\mu + \frac{\mu_t}{\sigma_\varepsilon} \right) \frac{\partial \varepsilon}{\partial x_j} \right] + \frac{C_{1\varepsilon} \varepsilon}{k} (P_k + C_{3\varepsilon} P_b) - \frac{C_{2\varepsilon} \rho \varepsilon^2}{k} \\ & + S_\varepsilon \end{aligned}$$

$$\mu_t = \rho C_\mu \frac{k^2}{\varepsilon} \quad (2.11)$$

Here,

$$P_k = \rho \overline{u'_i u'_j} \frac{\partial u_j}{\partial x_i} \quad (2.12)$$

$$P_b = -\frac{1}{\rho} \left(\frac{\partial \rho}{\partial T} \right)_p g_i \frac{\mu_t}{Pr_t} \frac{\partial T}{\partial x_i} \quad (2.13)$$

Here Pr_t is the turbulent Prandtl number, $C_{1\varepsilon} = 1.44$, $C_{2\varepsilon} = 1.92$, $C_\mu = 0.09$, $\sigma_k = 1$, $\sigma_\varepsilon = 1.3$

***k-omega* model**

The *k-omega* model is a low-Reynolds-number model that can be used in conjunction with wall functions. Generally, this model warrants the use of a denser mesh if wall functions are not used. It solves two transport equations: one for the turbulence kinetic energy (k) and one for the specific dissipation (ε), as shown in Equations 2.14 and 2.15. The turbulent kinematic viscosity is then computed as shown with Equation 2.16.

$$\frac{\partial k}{\partial t} + U_j \frac{\partial k}{\partial x_j} = \tau_{ij} \frac{\partial U_i}{\partial x_j} - \beta^* k \omega + \frac{\partial}{\partial x_j} \left[(v + \sigma^* \nu_T) \frac{\partial k}{\partial x_j} \right] \quad (2.14)$$

$$\frac{\partial \omega}{\partial t} + U_j \frac{\partial \omega}{\partial x_j} = \alpha \frac{\omega}{k} \tau_{ij} \frac{\partial U_i}{\partial x_j} - \beta^* \omega^2 + \frac{\partial}{\partial x_j} \left[(v + \sigma \nu_T) \frac{\partial \omega}{\partial x_j} \right] \quad (2.15)$$

$$\nu_t = \frac{k}{\omega} \quad (2.16)$$

Here, $\alpha = 0.555$, $\beta = 0.075$, $\beta^* = 0.09$, $\sigma = 0.5$, $\sigma^* = 0.5$

k-omega SST model

The *k-omega SST* model is a combination of the *k-epsilon* model in the free stream region and *k-omega* near the walls. Thus, this model requires a dense mesh only at the walls and can yield convergence in reasonable time with good accuracy. It solves for the turbulent kinetic energy and the specific dissipation using the Shear Stress Transport (SST) formulation. Zhang and Kleinstreuer (54) found that the RANS models were less computationally expensive than Large Eddy Simulations (LES) and the *k-omega SST* model provided better predictions in some cases in the lung airway geometry. This model has also been shown to accurately predict mean velocity distributions and turbulence kinetic energy in the transitional regime (56). For these reasons, this model was used to simulate pMDI and nasal sprays. To determine the best turbulence model to use, the non-dimensional distance from the wall is a useful parameter to analyze.

$$y^+ = \frac{u_\tau y}{\nu} \quad (2.17)$$

$$u_\tau = \sqrt{\frac{\tau_w}{\rho}} \quad (2.18)$$

Here, u_τ is the friction velocity, τ_w is the wall shear stress, ρ is the density of the fluid. The domain can be divided into the following regions based on the y^+ value.

- Viscous sublayer, $y^+ < 5$
- Buffer layer, $5 < y^+ < 30$
- Log-law layer, $30 < y^+ < 200$

2.1.3. Scalar Transport

$$\frac{\partial(c)}{\partial t} + \frac{\partial}{\partial x_i}(u_i c) = D \frac{\partial}{\partial x_i} \left(\frac{\partial c}{\partial x_i} \right) \quad (2.19)$$

Here c is the scalar of interest such as concentration or temperature, D is the diffusion coefficient. The Equation 2.19 describes the passive transport of a scalar quantity in a flow field. The driving forces for its transport are convection and diffusion. In this research, the customized solver, which was developed in OpenFOAM for solving the drug dissolution and absorption problem, is capable of handling the transport of concentration.

2.2 Aerosol Dynamics

2.2.1. Particle Trajectory Equation

Generally, the Eulerian approach is preferred for the analysis of fluid motion. As the fluid is a continuous medium, the analysis is based on the motion of fluid through a fixed volume, known as the control volume. The motion of particles in a flow field, on the other hand, is analyzed by tracking the fixed mass of the particle in the flow field. This approach is called Lagrangian Particle Tracking (LPT) and follows Newton's 2nd law of motion as shown in Equation 2.20.

$$m_p \frac{\partial^2 x_p}{\partial t^2} = \sum F_p \quad (2.20)$$

Here x_p is the position of the particle, m_p is the mass of the particle, F_p represents the various forces acting on the particle's center. Various forces such as the drag force, gravity, lift forces,

electrostatic force, and Brownian force may act on the particle. In this study, as most of the non-rotating particles were in the micron range, only the drag force and gravity were considered.

Drag Force

The drag force is the resistance offered by the fluid to the motion of the particles and its formulation is given in Equation 2.21.

$$F_D = \frac{1}{2} C_D \rho A v_{rel}^2 \quad (2.21)$$

Here, C_D is the coefficient of drag force, ρ is the density of the fluid, A is the projected area normal to the direction of the drag force, v_{rel} is the relative velocity between the particle and the fluid. The formulation for the coefficient of drag force depends on numerous factors including the particle shape. For a spherical particle, the drag coefficient's variation with the Reynolds number is expressed in Equation 2.22 (57).

$$C_D \approx \frac{24}{Re_p} + \frac{6}{1 + \sqrt{Re_p}} + 0.4, 0 \leq Re_p \leq 2 \times 10^5 \quad (2.22)$$

$$Re_p = \frac{\rho |\vec{v} - \vec{v}_p| d_p}{\mu}$$

The source term M_p in Equation 2.5 can now be written as shown in Equation 2.23 (7).

$$M_p = -\frac{1}{dV} \sum_1^{NP} \left(\frac{1}{8} \pi d_p^2 C_D (v - v_p) |v - v_p| \right) \quad (2.23)$$

Here, NP is the total number of particles in a cell, dV is the volume of the cell. Equation 2.23 represents the reaction of the drag force on the particles which serves to slow down down the flow due to the momentum exchange. For systems involving high-speed and high-concentration aerosol in which the flow field will be affected by the presence and the motion of the particles, two-way coupling needs to be enforced with M_p defined as given in Equation 2.23.

Gravitational Force

The gravitational force (see Equation 2.24) includes the effects of the weight of the particle and the buoyant forces acting on the particle opposing its weight. In the context of lung airway fluid-particle dynamics, these forces become important for particles of size between $1 \mu m$ and $5 \mu m$ which deposit by sedimentation.

$$F_p = m_p g \left(1 - \frac{\rho_f}{\rho_p} \right) \quad (2.24)$$

Here, g is the gravitational acceleration, ρ_f and ρ_p are the densities of the fluid and the particle.

2.2.2. Turbulent Dispersion

Turbulence in the flow affects the motion of particles as well. The random fluctuating component of the velocity of the fluid influences the particles trajectory in addition to the mean velocity

component. To account for the effect of turbulence on the particles, the stochastic dispersion model is used in this research. In this model, a random component is added to the velocity of the flow field to obtain the instantaneous velocity and to compute the position of the particle. The particle is assumed to be inside an eddy with a fluctuating velocity u_g' , lifetime t_e and characteristic length l_e . As long as the eddy lifetime is greater than the residence time of the particle inside, the present eddy's characteristics can be used to compute the particle motion. The various characteristics of the eddy are described in Equations 2.25-2.27 (7, 58).

$$u_g' = \tau \left(\frac{2k}{3} \right)^{0.5} \quad (2.25)$$

$$l_e = \frac{C_\mu^{0.75} k^{1.5}}{\varepsilon} \quad (2.26)$$

$$t_e = \frac{l_e}{\left(\frac{2k}{3} \right)^{0.5}} \quad (2.27)$$

Here, k and ε are the local turbulence kinetic energy and dissipation, C_μ is an empirical constant and τ represents random numbers with normal distribution and zero-mean, variance of one.

2.2.3. Boiling and Evaporation of Droplets

Mass transfer from the droplets to the surroundings can happen due to boiling and evaporation. In this study, the flash boiling and evaporation of the propellant droplets were simulated to study the spray characteristics of a pressurized metered dose inhaler. In OpenFOAM, the

liquidEvaporationBoil model simulates the boiling of droplets when the vapor pressure is higher than the surrounding air pressure and evaporation when it is lower.

The boiling process is simulated based on the model developed by Zuo et al. (59). According to the authors, the mass transfer rate due to flash evaporation is given by Equation (2.28).

$$G_f = \frac{\alpha_s(T_p - T_b)A}{L(T_b)} \quad (2.28)$$

Here, G_f is the drop flash vaporization rate, A is the droplet surface area, α_s is an overall heat transfer coefficient from the droplet interior to the surface as shown in Equation 2.29.

$$\begin{aligned} \alpha_s &= 0.76(T_L - T_b)^{0.26} & (0 \leq T_L - T_b \leq 5) \\ &= 0.027(T_L - T_b)^{2.33} & (5 \leq T_L - T_b \leq 25) \\ &= 13.8(T_L - T_b)^{0.39} & (T_L - T_b \geq 25) \end{aligned} \quad (2.29)$$

Considering the rate of vaporization due to external heat transfer, we obtain Equation 2.30.

$$G = 4\pi \frac{k}{c_p} r_0 \frac{Nu}{1 + \frac{G_f}{G}} \ln \left[1 + \left(1 + \frac{G_f}{G} \right) \frac{h_\infty - h_b}{L(T_b)} \right] \quad (2.30)$$

Thus, the total mass transfer rate is,

$$\dot{m} = (G + G_f) \quad (2.31)$$

This model accounts for the following scenarios:

- Droplet surface temperature is equal to the boiling point and the surface mass fraction approaches 1. This causes the Spalding mass transfer number (B_M) to be infinitely large.
- At superheated conditions, all the heat transferred from external surroundings is used to vaporize the liquid near the surface.
- The flash boiled vapor near the surface will reduce the amount of heat transferred from the surrounding gas.

When the temperature drops below the boiling point, the OpenFOAM model switches to the evaporation process based on the Spalding evaporation model (see Equation 2.32) (60).

$$\dot{m} = -\pi d_p Sh \rho_g D_F \ln(1 + B_M) \quad (2.32)$$

B_M is the mass Spalding number and is given by,

$$B_M = \frac{(Y_s - Y_\infty)}{(1 - Y_s)} \quad (2.33)$$

Here, Y_s is the vapor mass fraction near the surface, Y_∞ is the vapor mass fraction in the far field, D_F is the vapor diffusivity, ρ_g is the density of the gaseous mixture, d_p is the droplet diameter.

The Sherwood number (Sh) is modelled in OpenFOAM as,

$$Sh = 2 + 0.06 Re_p^{0.5} Sc^{0.33} \quad (2.34)$$

The Schmidt number (Sc) is defined as the ratio of the dynamic viscosity of the surrounding gas and the diffusivity of the vapor in the gas.

$$Sc = \frac{\nu}{D_F} \quad (2.35)$$

2.2.4 Solid Particle Dissolution

The dissolution of a solid particle depends on a variety of factors such as the surface area of the particle, height of the diffusion layer, solubility, the concentration of the dissolved phase in the bulk medium and the diffusion coefficient of the dissolved phase. These factors are included in the Noyes-Whitney equation (see Equation 2.36) which is used to describe the rate of dissolution.

$$\frac{dm}{dt} = \frac{DA(C_s - C_b)}{h} \quad (2.36)$$

Here, m is the mass of the solid particle, D is the diffusion coefficient of dissolved phase in the bulk medium, C_s is the solubility of the dissolved phase, C_b is the concentration of the dissolved phase in the bulk medium, h is the thickness of the diffusion layer which is approximately equal to the radius for particles of radius $< 30 \mu m$.

There is no provision in the official release of OpenFOAM, to simulate solid particle dissolution and its subsequent advection in the bulk flow. Thus, a customized solver, *dissolutionTransportFoam*, was developed by combining the scalar transport solver with the dissolution model, which was created by modifying the existing phase change model. The new diameter of the particle was used to compute the surface area (A) and the diffusion layer thickness

(*h*) and the mass of the particle that has dissolved was added to the bulk phase at the end of each time step thus ensuring a dynamic change in the rate of mass dissolved.

2.2.5 Epithelial Absorption

In this research, the drug dissolution and absorption at the nasal epithelium were studied. The drug dissolution and its advection were simulated using a customized OpenFOAM solver that combined the Noyes-Whitney equation and the passive scalar transport equation. The drug absorption process at the epithelium was handled using a C++ code for the boundary condition.

The epithelium is flanked by the airway surface liquid layer on one side and the cell membrane on the other. At the epithelial interface, the mass transfer condition can be written as shown in Equation 2.37.

$$D_{mucus} \left. \frac{\partial c}{\partial x} \right|_{mucus,i} = D_{mem} \left. \frac{\partial c}{\partial x} \right|_{mem,i} \quad (2.37)$$

Here, D_{mucus} is the diffusion coefficient of the drug in the airway surface liquid layer, D_{mem} is the diffusion coefficient of the drug in the cell membrane. Assuming a linear concentration gradient across the cell membrane and a perfect sink condition inside the cell, we get Equation 2.38.

$$D_{mucus} \left. \frac{\partial c}{\partial x} \right|_{mucus,i} = D_{mem} \frac{C_{mem}}{t_{mem}} \quad (2.38)$$

Here, C_{mem} is the concentration at the epithelium on the side of the membrane and t_{mem} is the thickness of the membrane. The airway surface liquid is mainly composed of water while the cell

membrane contains lipids. In such case, the drug will not be uniformly dispersed on both sides of the interface. The octanol/water partition coefficient (kow) is defined as the ratio of the concentration of the drug in the lipid phase and the aqueous phase (see Equation 2.39).

$$kow = \frac{C_{mem}}{C_{mucus}} \quad (2.39)$$

Inserting Equation 2.39 into 2.38, we get Equation 2.40 for the concentration gradient which was coded in C++ and integrated with the solver separately as a dynamic library.

$$\left. \frac{\partial c}{\partial x} \right|_{mucus,i} = \left(\frac{D_{mem} kow}{D_{mucus} t_{mem}} \right) C_{mucus} \quad (2.40)$$

CHAPTER 3: NUMERICAL SOLVERS AND MODEL VALIDATION

3.1 Introduction to OpenFOAM

The open-source computational fluid dynamics (CFD) toolbox OpenFOAM (<https://openfoam.com>) was employed for all project simulations. Developed and managed by the OpenFOAM Foundation, the toolbox is being widely used by academicians and industry experts alike for simulating physical phenomena ranging from multiphase flow to fluid-structure interaction problems. In addition to its CFD-application versatility, OpenFOAM is cost-free, portable, accessible, and open to user-defined functions. The software is written in C++ and hence relies on the practices of Object-Oriented Programming (OOP) which emphasizes on segmenting a numerical code into blocks, called classes. Such features enhance the readability of the software that in turn make it highly suitable for developing customized solvers and integrating the libraries existing modules. This high-level functionality of OpenFOAM was taken advantage of in this research at various points.

There are three stages in the process of numerically solving CFD problems:

- Preprocessing
- Solution
- Postprocessing

The preprocessing stage is concerned with meshing the geometry and assigning appropriate values to the scalar and vector fields. OpenFOAM has built-in meshing capabilities (blockMesh and snappyHexMesh) which can be used to manually discretize the computational domain into elements of finite sizes. It can also be ported with external meshing software such as ICEM and Gambit (see Ansys software). The solution stage is when the governing equations, such as the

Navier-Stokes equations for flow, Basset-Boussinesq-Oseen equation for particle tracking, and/or advection-diffusion equation for species-mass transfer, are solved numerically using various schemes. OpenFOAM boasts a plethora of numerical programs for simulating various processes, compiled as C++ dynamic libraries. The main program then calls on the functionalities in these libraries during the simulation and thus solves for the fields of interest in all the discretized cells. Postprocessing is the stage when results of the simulation are visualized using contours and graphs to obtain insight into the spatial and temporal variations of key dependent variables such as velocity, pressure, concentration, and temperature. While OpenFOAM does not feature visualizing tools, it comes with various functionalities to write the data in a raw format. This data can be loaded to other third-party visualization toolboxes, eg, Tecplot, Paraview or CFD-Post, for performing a wide variety of postprocessing operations in order to enhance the understanding of the physics involved. Additionally, the raw data also makes it easy for writing custom-postprocessing programs, say, using C++ or Python, to observe the trend in the spatial and temporal data. In fact, Python scripts were used extensively for this project to better understand the spray dynamics and mucus layer velocity fields after postprocessing.

Large and complex geometries containing millions of computational cells often take a very long time to solve. Such large cases can be sped up if the geometry is divided into subdomains and computation happens in parallel in all the parts. This feature is called parallel computing and OpenFOAM provides a neat way to achieve parallelization. The division of the geometry can be accomplished either by manually specifying the number of parts in the three Cartesian directions or by using an in-built algorithm to automatically divide the geometry with parts having an equal number of cells. The advantage of the latter method is that the lag in data transfer between the subdomains is minimized if they have approximately the same number of cells. Specifying the

method of division in the *decomposeParDict* file and running the *decomposePar* command will help achieve parallelization in OpenFOAM. Typically, for the nasal and oral airway geometries, the number of subdomains used was over 50.

3.2 Case Structure in OpenFOAM

Unlike other software which offer an interactive graphics interface to set up a simulation, OpenFOAM does not have such a feature. Instead, OpenFOAM relies on different files to specify boundary conditions, mesh, properties, etc. Although such an approach is primitive, it helps in understanding the flow of the open-source CFD code better. OpenFOAM primarily has three folders with various files as shown in Figure 6. The files required inside these folders vary depending on the solver used.

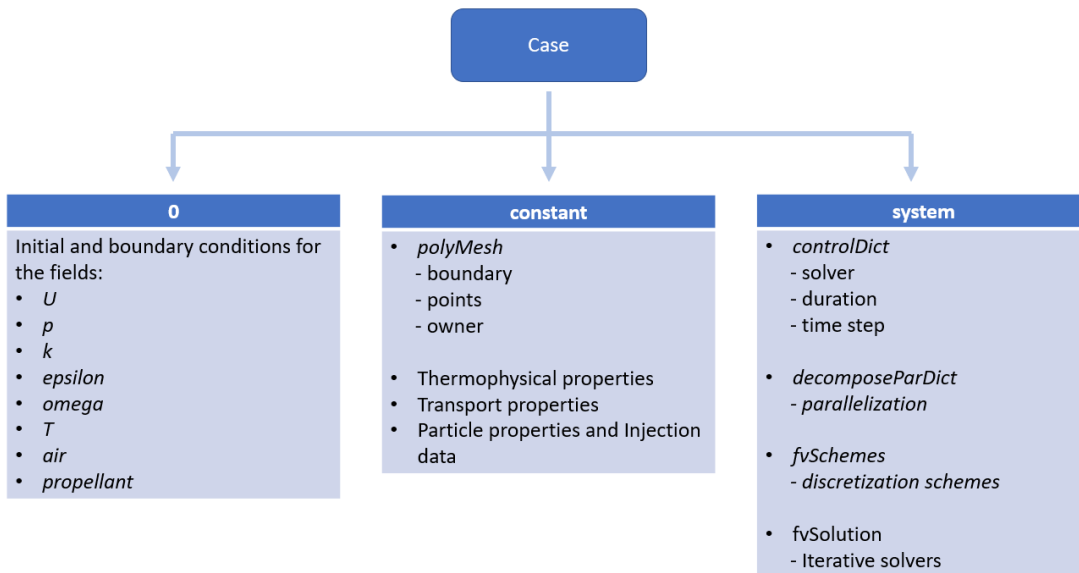


Figure 6. Case structure in OpenFOAM

The 0 folder

The 0 folder contains the files with the initial and boundary conditions. The parameters to be solved are decided based on the type of solver and the flow problem. These can be either vectors such as velocity (U) or scalars such as pressure (p) and temperature (T). The initial condition is imposed at all the internal cells and can be specified as either a single value or a list of values. The syntax for specifying the initial condition as a single value for all cells is:

```
internalField uniform ( < value > );
```

and for specifying the initial condition as an array of values for the internal cells is:

```
internalField nonuniform List<vector>;
```

```
< number of cells >
```

```
(
```

```
    < value 1 >
```

```
    ...
```

```
);
```

The boundary conditions are specified for each of the patches specified in the mesh files. In general, there are 3 types of boundary conditions used in solving differential equations. They are Dirichlet, Neumann and Robin boundary conditions. The Dirichlet condition is used to impose a fixed value for the entire boundary and is specified in OpenFOAM as shown below.

```
< patch name >
```

```
{
```

```

    type          fixedValue;

    value         uniform ( < value > );

}

```

The Neumann boundary condition is used at the boundary where the derivative of a field is known. Such conditions are used to specify a heat flux condition on a heated surface. The syntax in OpenFOAM is shown below.

```

< patch name >

{

    type          fixedGradient;

    gradient      uniform ( < value > );

}

```

The Robin, or mixed, boundary condition is a combination of the Neumann and Dirichlet conditions. An example of a Robin condition is given in Equation 3.1. A customized code snippet is generally compiled as a dynamic C++ library which then interfaces with the solver code when the simulation starts.

$$\frac{\partial c}{\partial x} = -Kc \quad (3.1)$$

Numerically, Equation 3.1 can be discretized as shown in Equation 3.2:

$$c_f = \frac{c_{int}}{(1 + K \Delta x)} \quad (3.2)$$

Here, c_f is the value of the field at the boundary, c_{int} is the value of the field in the internal field near the boundary, K is a constant, Δx is the distance of the cell center of the internal cell to the boundary. The C++ syntax used to specify the Robin boundary condition in OpenFOAM is shown below.

```
{  
  
    const scalarField& invDeltaX = patch().deltaCoeffs();  
  
    const scalar K = 10;  
  
    scalarField& field = *this;  
  
    field = patchInternalField() / (1 + (K / invDeltaX));  
  
}
```

The `deltaCoeffs()` function returns the inverse of the distance between the internal cell and the patch in an array. The code block is added under the name of the patch for which the Robin boundary condition needs to be imposed. The Robin condition was used in this work to simulate the shift in the concentration at the nasal epithelial surface.

Figure 7 shows a file inside the `0` folder displaying the various boundary conditions.

```

/*-----* C++ -*-----*/
FoamFile
{
  version      2.0;
  format       ascii;
  class        volScalarField;
  location     "0";
  object       conc;
}
// *****

dimensions      [1 -3 0 0 0 0 0];

internalField   uniform 0;

boundaryField
{
  "(NOSTRIL|NV_AIR|NV_EPI|NASAL_AIR)"
  {
    type          zeroGradient;
  }

  NASAL_EPI
  {
    type          codedFixedValue;
    value         uniform 0;
    name          robinBC;
    codeInclude
    #{
      #include "fvCFD.H"
      #include <iostream>
    #};

    codeOptions
    #{
      -I$(LIB_SRC)/finiteVolume/lnInclude \
      -I$(LIB_SRC)/meshTools/lnInclude
    #};

    codeLibs
    #{
      -lmeshTools \
      -lfiniteVolume
    #};

    code
    #{
      const fvPatch& boundaryPatch = patch();
      const vectorField& Cf = boundaryPatch.Cf();

      const scalar Dmuc = 4.2e-6;
      const scalar Dmem = 1.4e-6;
      const scalar tmem = 1e-5;
      const scalar kow = 5000;
      const scalar K = (Dmem*kow)/(Dmuc*tmem);

      scalarField& field = *this;

      field = patchInternalField()/(1 + (K/boundaryPatch.deltaCoeffs()));
    #};
  }

  NASOPHARYNX
  {
    type          fixedValue;
    value         uniform 0;
  }
}
// *****

```

Figure 7. The different types of boundary conditions

The constant folder

The *constant* folder contains files pertaining to the mesh, thermo-physical properties, turbulence and particle injection data. The mesh data is contained within the *polyMesh* folder inside the *constant* folder. Typically, the mesh is created using a third-party software like ICEM and the *fluent3DmeshToFoam* command is run to generate the files in the *polyMesh* folder which are written in the OpenFOAM format. To completely describe the mesh, OpenFOAM primarily generates the following files.

- Boundary
- Points
- Owner

The *Boundary* file contains the names of the boundaries, number of faces and the ID of the starting face written in the following format.

```
< patch name >  
  
{  
  
    type          wall;  
  
    nFaces        < value 1 >;  
  
    startFace     < value 2 >;  
  
}
```

The *Points* file lists the Cartesian coordinates of all the nodes in the mesh. Each face, internal and boundary, is owned by 1 or more cells in the mesh. The IDs of the cells which own the faces in

the mesh are listed in the *Owner* file. These mesh data, although generated by OpenFOAM, was used extensively in this study to perform certain operations to generate and segment the nasal mucus layer mesh into the anterior and posterior regions.

For each simulation, the thermo-physical and transport properties need to be specified at the beginning of the numerical analysis. The transport properties include the density and viscosity of the fluid. For simulations involving phase change of a component, the thermo-physical properties such as the Prandtl number and molecular weight of the gaseous phase also need to be provided. OpenFOAM also offers a range of apparent viscosity models such as the *Power law* and the *Bird-Carreau* model besides the Newtonian fluid model. Similarly, for simulations involving phase change, the density can be computed assuming the perfect gas law or by providing coefficients of the fitting polynomial. Depending on the models chosen for the transport and the thermo-physical properties, the constants that need to be provided vary. The appropriate keywords or constants can be specified by referring the support documentation available online or by perusing the open-source code of the model, if the user has a good grasp on C++.

OpenFOAM can also be used for studying the interaction of droplets or particles with fluid. In such cases, the properties of the particles and the injection data need to be specified before the start of the simulation. Particles can be injected from an entire patch or at a cone angle from a small nozzle by selecting the appropriate injection models. Breakup and evaporation of droplets, and solid particle collision and turbulent dispersion can also be simulated by choosing from a variety of in-built models and providing the required values for the constants. Figure 8 shows the commonly used models in OpenFOAM for simulating various fluid-particle dynamics processes.

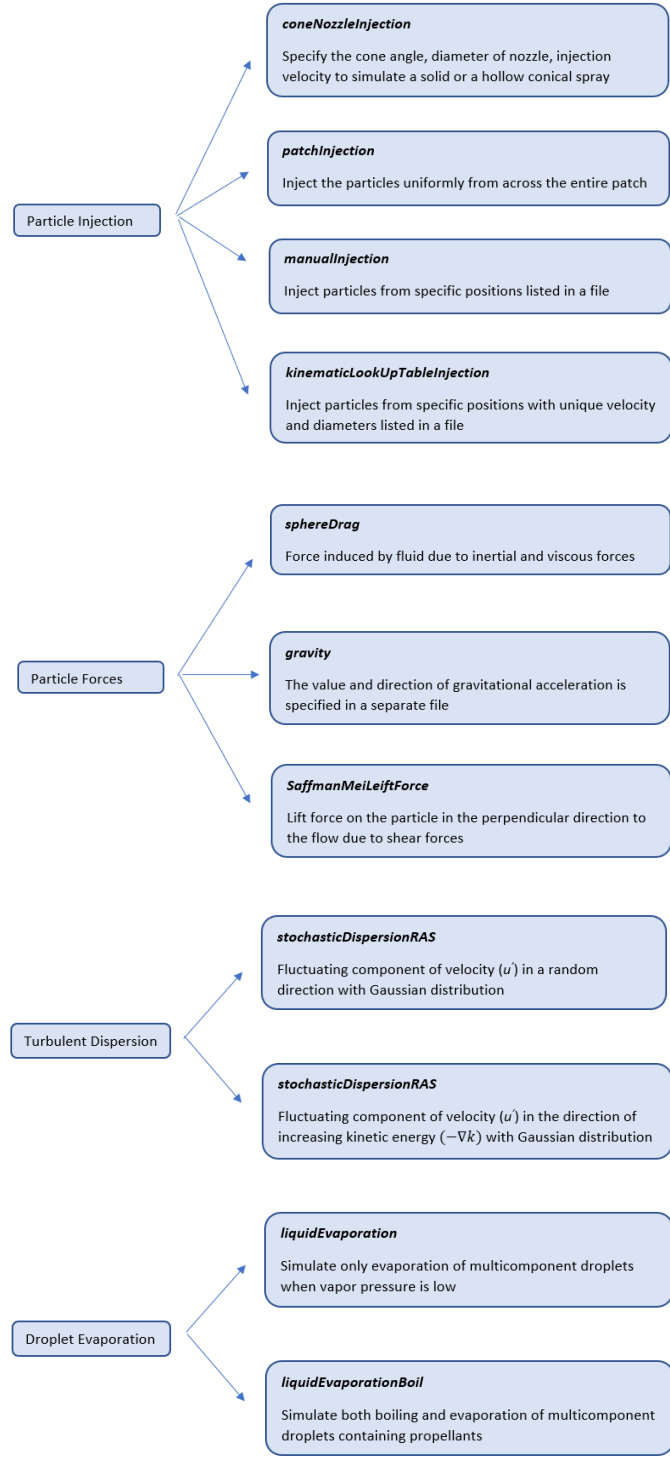


Figure 8. Commonly used particle models in OpenFOAM

The system folder

The *system* folder contains information regarding the simulation time, parallelization and numerical schemes. The name of the solver, total time and time step are typed in the *controlDict* file by the user. As mentioned before, the number of subdomains required for parallelization and the algorithm for division of the domain are specified in the *decomposeParDict*.

The Navier-Stokes equations (see Equation 3.3) are a set of non-linear partial differential equations that are used to describe flow fields with constant fluid properties. In CFD, these partial differential equations are discretized to yield the numerical form which will be solved iteratively for the specified time duration. These equations contain temporal, gradient, divergence and Laplacian terms, which can be discretized using numerical schemes.

$$\underbrace{\nabla \cdot \vec{u}}_{Divergence} = 0 \quad (3.3a)$$

$$\underbrace{\frac{\partial \vec{u}}{\partial t}}_{Temporal} + \underbrace{\vec{u} \cdot \nabla \vec{u}}_{Gradient} = - \underbrace{\frac{1}{\rho} \nabla p}_{Gradient} + \underbrace{\frac{\mu}{\rho} \nabla^2 \vec{u}}_{Laplacian} + \vec{g} \quad (3.3b)$$

Over the years, a variety of numerical schemes have been developed to accurately discretize the terms of the partial differential equations. The choice of the scheme needs to be made carefully by considering the various advantages and disadvantages. For instance, higher-order schemes for the divergence term provide greater accuracy than lower-order schemes but may exhibit oscillatory behaviour. These schemes are generally specified by the user in the *fvSchemes* file present in the *system* folder. Some of the commonly used schemes in OpenFOAM are listed in Table 1.

Table 1. Commonly used schemes for numerical discretization

Term	Keyword	Scheme
Temporal	ddtSchemes	<ul style="list-style-type: none"> • Euler • Backward • CrankNicolson
Gradient	gradSchemes	<ul style="list-style-type: none"> • Gauss linear • leastSquares
Divergence	divSchemes	<ul style="list-style-type: none"> • Gauss upwind • Gauss linearUpwind • Gauss linear • Gauss limitedLinear
Laplacian	laplacianSchemes	<ul style="list-style-type: none"> • Gauss linear corrected • Gauss linear orthogonal
Interpolation	interpolationSchemes	<ul style="list-style-type: none"> • Gauss linear

After numerical discretization, OpenFOAM assembles the equations at all the cells into a matrix of the form shown in Equation 3.4 where the unknown X is the solution at the next time step or iteration in a steady state simulation.

$$AX = B \tag{3.4}$$

To solve a system of equations, the most common approach is to use iterative solvers. OpenFOAM provides a variety of solvers built on the Gauss Seidel and Gauss Jacobi methods. Some of the commonly used iterative solvers in OpenFOAM are listed in Table 2.

Table 2. Commonly used iterative solvers in OpenFOAM

Field	Solver	Smoother
p	GAMG	GaussSeidel
U	smoothSolver	symGaussSeidel
k	smoothSolver	symGaussSeidel
epsilon	smoothSolver	symGaussSeidel
omega	smoothSolver	symGaussSeidel

To solve pressure, the geometric-algebraic multi-grid (GAMG) solver is commonly selected in OpenFOAM. This solver maps the set of equations onto a finer grid and obtains the solution which is later translated back onto the original grid. Thus, this iterative solver provides results with greater accuracy during each iteration and as a result, convergence is reached in lesser time. In addition to choosing the iterative solvers and providing tolerance values, relaxation factors can also be specified in the *fvSolution* file. These factors control the fraction of the result at the end of each iteration to be used for the next iteration. Relaxation factors are generally used if the residuals fail to fall below the specified tolerance limit smoothly.

3.3 Droplet Evaporation Model

Evaporation of micron droplets is one of the important mechanisms that contributes to the size reduction of aerosol droplets emitted from, say, a pressurized metered dose inhaler (pMDI) along with secondary atomization. In the present study, the *liquidEvaporationBoil* model in OpenFOAM was selected to simulate the flash evaporation of the propellant in all the cases. This model simulates the boiling of droplets using the method outlined in Zuo et al. (59) and evaporation using the Spalding model (60), both of which are described in Chapter 2. As the propellant droplets exit the nozzle in a superheated state, it was deemed appropriate to use the *liquidEvaporationBoil* model to simulate flash boiling and evaporation processes.

The chosen evaporation model was validated by simulating the evaporation of a water micron droplet as described by Zientara et al. (61), and then comparing the results with their experimental data. The experiment was conducted by suspending a water micron droplet in quiescent air using an electrostatic charge and observing the change in the diameter as time progressed. The authors noted that, considering the relatively small time scale of evaporation of the droplet, the influence of droplet charge on evaporation was negligible. The thermodynamic conditions of the experiment are presented in Table 3.

Table 3. Parameters used in the evaporation experiment

Parameter	Value
Chamber pressure (kPa)	110.6
Chamber temperature (K)	286.3 ± 0.5
Droplet temperature (K)	286.3 ± 0.5 (equal to chamber temperature)
Droplet radius (μm)	11
Relative humidity (%)	90 (from sensors) 98.05 (from evolutionary dynamics)

The parameters listed in Table 3 were used in the simulations as well. The authors also found that the evolution of the droplet was extremely sensitive to the relative humidity. A value of 98% for the relative humidity, which translates to a mass fraction of 0.00898 for water in the surrounding air, was specified as the initial condition for the simulation. Figure 9 shows the results obtained from the simulation and their comparison with the experimental data.

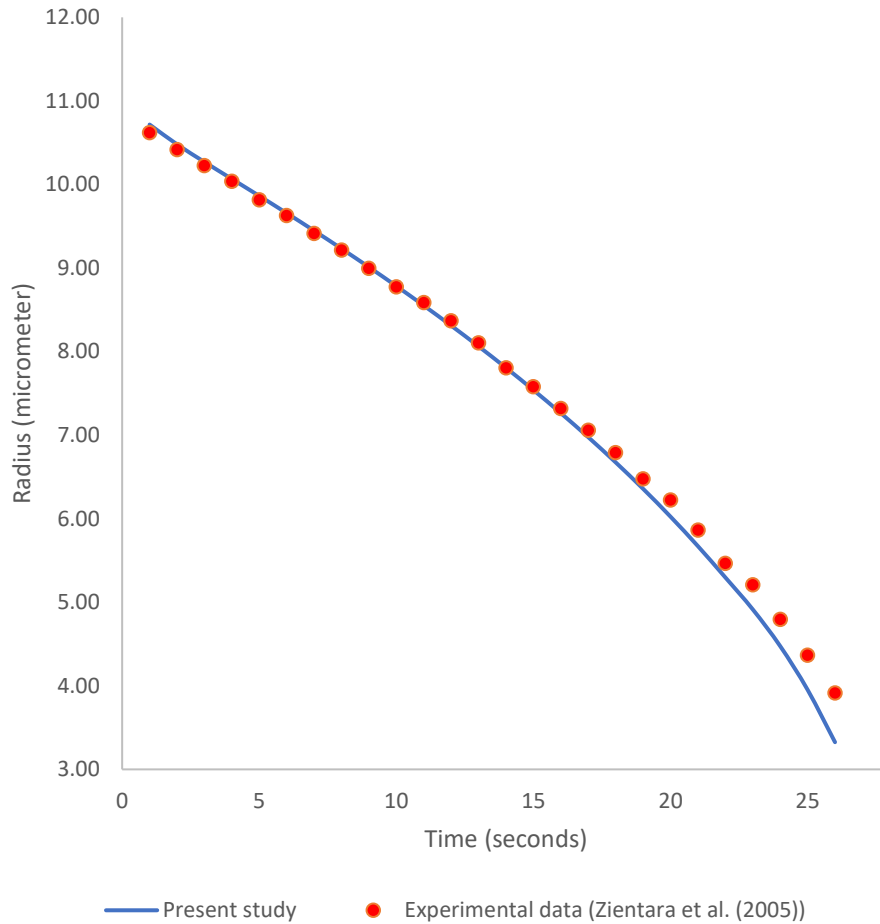


Figure 9. Evaporation of a water micron droplet

The results indicate a non-linear decrease in the size of the droplet with time which is in excellent agreement with the experimental data. The radius of the water droplet reduces from 11 μm to under 4 μm within 26 seconds. The fluctuations in the temperature of the droplet throughout the process was also found to be minimal (< 1 K) as noted in the experiments and hence the model simulates the evaporation process with great accuracy.

The evaporation of a propellant droplet occurs very fast (few milliseconds) and hence there is a dearth of studies focusing on the experimental characterization of the evaporation of a propellant droplet. However, Sheth et al. (27) have derived a theoretical model to describe the reduction in the diameter of a propellant droplet and applied it to compute the decrease in droplet size. The ordinary differential equation obtained by Sheth et al. (27) to predict the rate of change of a HFA propellant droplet diameter is given in Equation 3.5.

$$\frac{dD_D}{dt} = \frac{-4D_{HFA}M_{HFA}p_D}{R\rho_{HFA}D_D T_D} \times \left[\frac{2\lambda + D_D}{D_D + 5.33 \left(\frac{\lambda^2}{D_D} \right) + 3.42\lambda} \right] \quad (3.5)$$

Where D_D is the droplet diameter, t is the time, D_{HFA} is the diffusion coefficient of HFA propellant vapor in air, M_{HFA} is the molecular weight of the propellant, p_D is the vapor pressure of the propellant at the droplet surface, R is the gas constant, ρ_{HFA} is the density of the HFA propellant, T_D is the droplet temperature, λ is the mean free path of the propellant molecule in air.

The authors made the following assumptions when deriving the theoretical model.

- Ambient temperature of 20 °C.
- Evaporations occurs in still air, free of propellant, at the wet bulb temperature.
- Stefan flow and convective heat transfer have negligible effects.

The authors had also extended the model to include the evaporation of the less volatile cosolvent such as ethanol by the considering the evaporation of both the components in 2 successive stages. The evaporation of the HFA134a droplets was simulated using the *liquidEvaporationBoil* model, and the results were compared with the solution of the theoretical model of Sheth et al. (27). Figure

10 shows the evaporation of a HFA134a droplet with an initial diameter of $7.4 \mu\text{m}$ containing 0.3% (w/w) of non-volatile drug.

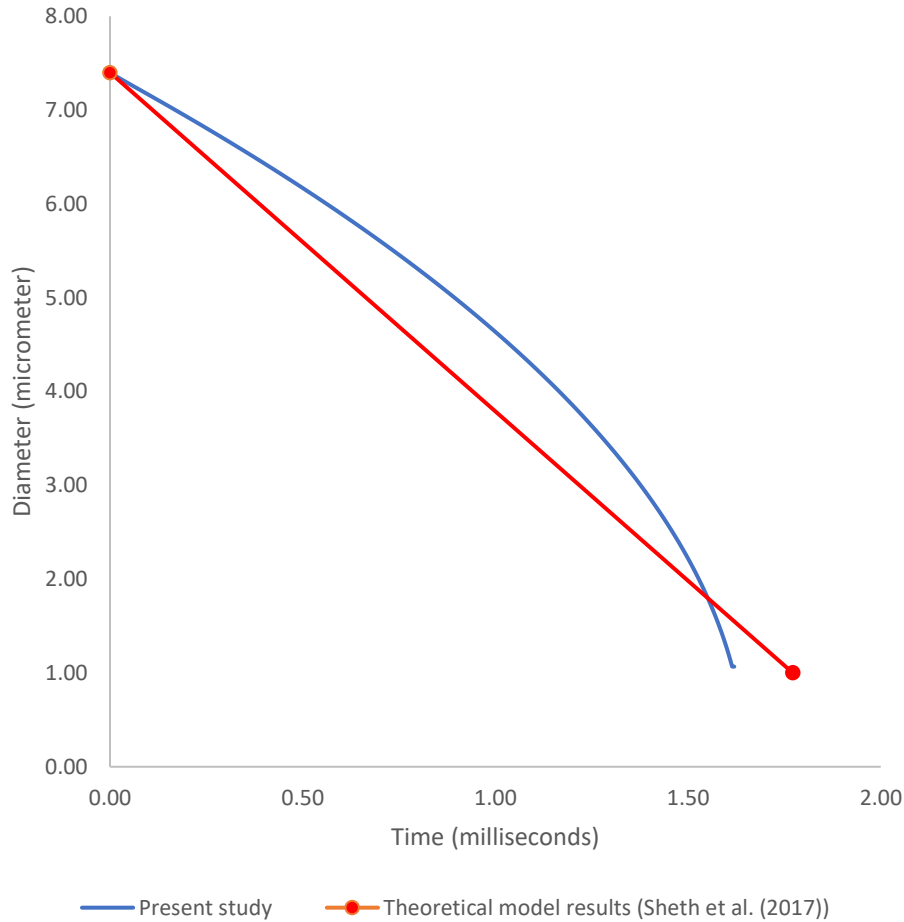


Figure 10. Evaporation of a HFA134a micron droplet

The high vapor pressure of the propellant results in complete evaporation of the volatile substance in less than 2 milliseconds. The evaporation model in OpenFOAM predicts a non-linear decrease in the diameter, whereas the theoretical model yields a quasi-linear size reduction. In any case, given the small time scales, the values obtained from the simulation are very close to the results of the theoretical model. Such accuracy is required in predicting the evaporation rate of a single

droplet as the validity of the model becomes important when the time scales increase and when a larger number of evaporating droplets is present.

3.4 Nasal Spray Lagrangian Particle Tracking

Nasal aerosol spray pumps emit high velocity droplets of relatively large diameters. Such spray systems typically require a two- or even a four-way coupled approach, which include the particle-flow and particle-particle interactions for tracking the Lagrangian particles in a computational domain. However, previous studies, eg, Calmet et al. (62) and Inthavong et al. (63), have shown that the one-way coupled approach suffices for nasal aerosol transport and deposition. Clearly, the one-way coupled approach is less computationally expensive which will enable running a larger number of simulations for a parametric study.

To validate the one-way coupled approach for tracking particles inside the nasal cavity, the CFD solver was validated by comparing the results with the computational study conducted by Kimbell et al. (64). The authors used the commercial software, FIDAP, to simulate airflow of flowrate 15 LPM and developed an algorithm in C++ to track the particles. This study was chosen due to the similarity in the nasal cavity models used, the partition of the geometry into the anterior and the posterior region, and the controlled examination of the parameters such as the spray angle, particle size and velocity. In their computer experiments, the authors conducted a parametric analysis using the specifications listed in Table 4 which cover a general range of observed values in experiments conducted by Southall et al. (65).

Table 4. Parameters used in the nasal spray computer experiment

Flow rate (LPM)	15
Nozzle insertion depths (cm)	0.5, 1, 1.5
Particle sizes (μm)	20, 50
Particle velocities (m/s)	1, 10
Spray angles (degrees)	32, 79

The authors used their validated in-house solver to predict the portion of the dosage that crosses the anterior or the nasal vestibule region (see Figure 4) and concluded that their results compared well with the general trends reported in prior studies. In the present study, the *icoUncoupledKinematicParcelFoam* solver, which is used for simulating one-way coupled particle dynamics, was selected. The results obtained using the OpenFOAM solver in comparison with those reported by Kimbell et al. (64) is presented in Table 5.

Table 5. Comparison of results with the nasal spray computer experiment

No.	Nozzle insertion depth (cm)	Size (μm)	Velocity (m/s)	Spray angle (degrees)	% Passing anterior region	
					Kimbell et al. (64)	Present study
1	0.5	50	1	32	3	1.44
2	0.5	50	1	79	2	2.11
3	0.5	20	10	32	1	1.87
4	0.5	20	10	79	2	3.55
5	1	50	10	79	1	0.15

Table 5 (continued).

6	1	50	1	32	4	0.41
7	1	50	1	79	4	0.92
8	1	20	10	79	1	1.04
9	1	20	1	32	18	27.62
10	1	20	1	79	19	21.22

Given the subtle differences in the geometries, the tracking approach and the high variability in matching the injection position and angle, the results of the present study agree with the data of Kimbell et al. (64) for most of the cases. The solver also predicts the relatively lower deposition in the anterior region for the parameters used in the simulations 9 and 10. Thus, OpenFOAM solver provides reliable predictions of particle deposition in the nasal cavity and can be used in simulating aerosol deposition from nasal sprays with realistic particle diameters and velocities.

3.5 Solid Particle Dissolution Model

After inhaled aerosol deposition, the dissolution of the solid drug particle is the first step towards drug absorption into the epithelium. To simulate this process, a customized model was developed in C++ in OpenFOAM using the Noyes-Whitney equation (see Equation 2.1). The model accounts for the real-time computation of the area and the diffusion layer thickness using the reduced diameter at each time step.

The customized *NoyesWhitney* dissolution model was validated by comparing the results with the experimental results of Franek et al. (48). The authors conducted the experiments by capturing

Fluticasone Propionate (FP) micron particles of mass median diameter (MMD) $2.4 \mu m$ on filter papers inside the cascade impactor. The filter papers were then placed over a Transwell semi-permeable membrane and immersed in a dissolution medium containing Phosphate Buffered Saline (PBS) + 0.5% SDS. The authors then studied the time it took for the drug to dissolve and permeate into the receptor. The parameters used in the experiment are listed in Table 6.

Table 6. Parameters used in the dissolution experiment

Parameter	Value
Drug	Fluticasone Propionate (FP)
Dissolution medium	PBS + 0.5% SDS
Solubility (mg/ml)	0.024
Mass median diameter (μm)	2.4
Donor volume (ml)	0.77
Receptor volume (ml)	2.23
Thickness of filter paper (μm)	250-300
Thickness of Transwell membrane (μm)	10
Porosity of filter paper	0.7 – 0.85
Porosity of Transwell membrane	0.005

For the simulations, a geometrical model was constructed as shown in Figure 11 with the specifications used in the experiment and meshed. The volume of the receptor chamber was significantly higher compared with the donor volume and the drug permeating into the receptor chamber was stirred to achieve uniformity in concentration. Thus, the concentration of the drug in

the receptor chamber was expected to be low, considering the small amount of drug and the large volume of the chamber, and hence was not modeled in the simulations. The porosity of the filter and the Transwell membrane was then used to compute an effective diffusivity for each of the 2 domains.

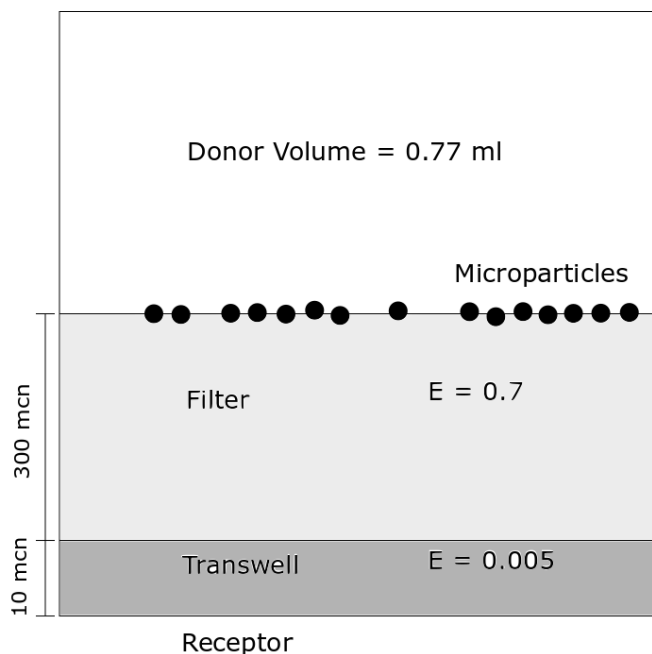


Figure 11. Computational domain for the dissolution simulation

The porosity of the filter paper and the Transwell membrane allows the dissolved drug to seep into the receptor chamber. The customized *dissolutionTransportFoam* was used to simulate the dissolution of the drug and the transport of concentration. The amount of drug permeating into the receptor chamber or leaving the computational domain was then computed as a fraction of the total mass of drug injected and plotted with time as shown in Figure 12. For comparison, the experimental results of Franek et al. (48) at specific time intervals are shown as well.

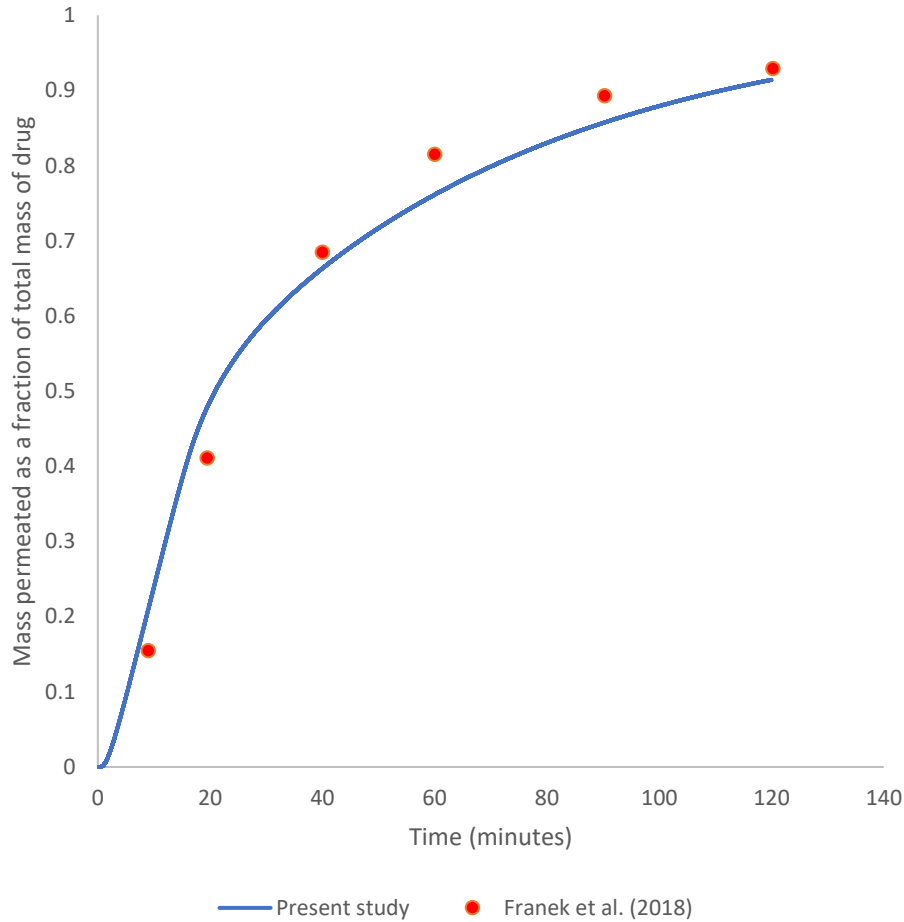


Figure 12. Dissolution and permeation of Fluticasone Propionate (FP)

The dissolution and permeation of FP takes over 2 hours to complete and the rate of permeation decreases as the mass remaining in the system also decreases due to the reduction in the concentration gradient across the membrane. The results from the simulation match well with the experimental data; thus, verifying the accuracy of the customized dissolution model. The aqueous solubility of FP is very low (0.00014 mg/ml) in comparison to the solubility in the dissolution medium used in the experiment. The authors attribute this increase in solubility to addition of an artificial lung surfactant and this necessitates further research with natural surfactants.

3.6 Drug Absorption Boundary Condition

After dissolution, the drug is ready to be absorbed by the epithelium to reach the systemic blood circulation. The uptake boundary condition was validated by comparing the results of mass of drug permeating through the epithelium obtained from CFD simulations with *in vitro* data reported by Sadler et al. (45). The *in vitro* drug absorption study was conducted by allowing Salmeterol Xinafoate solution to permeate through an epithelial cell monolayer grown on a Transwell polyester membrane. The parameters used in the experiment are listed in Table 7.

Table 7. Parameters used in the epithelial absorption experiment

Parameter	Value
Drug	Salmeterol Xinafoate (SX)
Dissolution medium	Bovine serum albumin with additives
Solubility (mg/ml)	0.045
Permeability coefficient (cm/s)	$2.6 \pm 1.0 \times 10^{-5}$
Diameter (μm)	1 - 4
Donor volume (μl)	100
Receptor volume (μl)	500
Thickness of cell monolayer (μm)	~ 10
Thickness of Transwell membrane (μm)	10
Porosity of Transwell membrane	0.005

The octanol-to-water partition coefficient (k_{ow}) of the drug can vary between *in vivo* and experimental conditions and hence can be obtained from the reported permeability coefficient. The

experimental permeability coefficient is $2.6 \pm 1.0 \times 10^{-5}$ cm/s and can be described as shown in Equation 3.6.

$$P = \left(\frac{\dot{m}}{AC_0} \right) \quad (3.6)$$

Here, P is the permeability coefficient, \dot{m} is the rate of mass permeation, A is the area of the cell monolayer, C_0 is the initial concentration in the donor chamber. The relationship between kow and P was theoretically obtained by solving the mass transfer expressions at the epithelial surface and is given by Equation 3.7.

$$kow = \frac{PD_{donor}t_{epi}}{(D_{donor}D_{epi} - Pt_{donor}D_{epi})} \quad (3.7)$$

Where D_{donor} is the diffusivity of the drug in the donor fluid, t_{epi} is the length scale of the cell layer, D_{epi} is the diffusivity of the drug in the cell layer and Transwell membrane, t_{donor} is the length scale of the donor chamber. Using Equation 3.7, the kow of the drug under experimental conditions used in the study was approximated as 1.33.

The drug absorption validation study was carried out using a mesh of only the donor chamber (see Figure 13) with the uptake boundary condition imposed on the bottom surface which is the interface between the donor chamber and the epithelium.

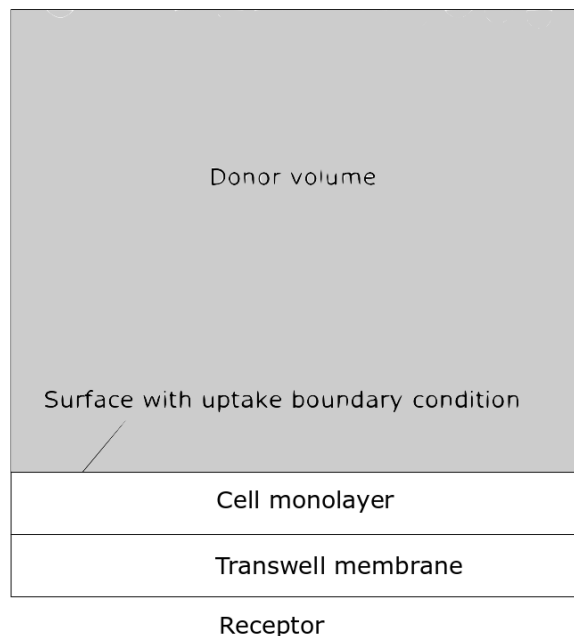


Figure 13. Computational domain (shaded area) for the absorption simulation

The absorption at the epithelial surface was modeled using a Robin boundary condition (see Equation 3.8), taking the octanol/water partition coefficient into account, and the same was discretized and coded in C++ using the functions defined in OpenFOAM as shown in Equation 3.9. The aqueous diffusivity of Salmeterol Xinafoate was calculated as $6\text{e-}10\text{ m}^2/\text{s}$ and applied throughout the domain. Although not geometrically modeled in the simulation, the effects of the cell monolayer, Transwell membrane and the concentration of the drug in the receptor chamber were included in the absorption boundary condition. To account for the low porosity of the Transwell membrane, an effective diffusivity of $3\text{e-}12\text{ m}^2/\text{s}$ was computed for the cell layer and Transwell membrane combination. The concentration in the receptor chamber was computed using the mass leaving the domain and the volume of the chamber at each time step rather than assuming a perfect sink condition.

$$\left. \frac{\partial c}{\partial x} \right|_{donor,i} = \frac{D_{epi}}{D_{donor}} \left(\frac{kow C_{donor,i} - C_{receptor}}{t_{mem}} \right) \quad (3.8)$$

$$C_{donor,i} = \left(\frac{C_{donor,int} + \left(\frac{D_{epi} \Delta x_{donor,i}}{D_{donor} t_{mem}} \right) C_{receptor}}{1 + \left(\frac{D_{epi} \Delta x_{donor,i}}{D_{donor} t_{mem}} \right) kow} \right) \quad (3.9)$$

Here, $C_{donor,i}$ is the concentration of drug at the interface in the donor, $C_{donor,int}$ is the concentration in the internal cell near the epithelium in the donor, $C_{receptor}$ is the concentration in the receptor chamber, kow is the octanol/water partition coefficient, D_{epi} is the effective diffusion coefficient of the drug in the epithelial cell layer and the Transwell membrane, D_{donor} is the diffusion coefficient of the drug in the donor fluid, t_{mem} is the combined thickness of the cell layer and the Transwell membrane, $\Delta x_{donor,i}$ is the distance of the cell center near the epithelium from the interface. Equation 3.9 was coded as a C++ dynamic library in OpenFOAM to simulate the passive transport of the concentration across the dissolution medium and the epithelium.

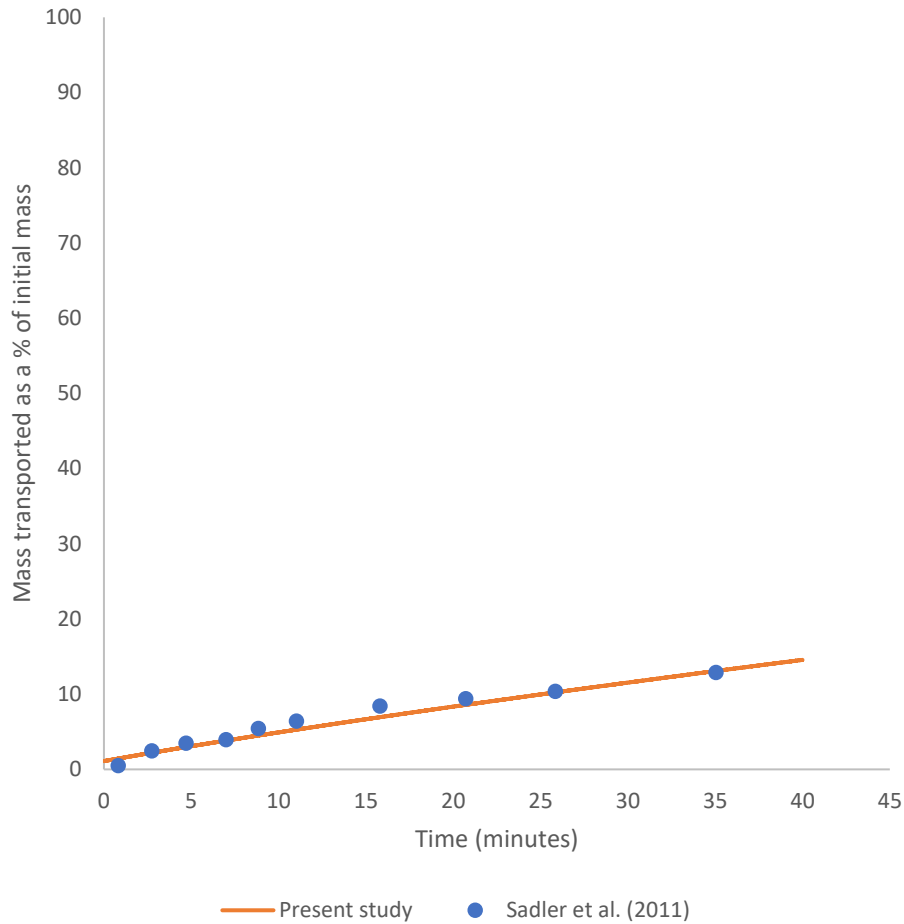


Figure 14. Profile of mass of the drug permeated into the receptor with time

The resulting profile of the mass of the drug leaving the donor and then permeating into the receptor was compared, as a percentage of the total mass (180 ng), with the values reported in the *in vitro* study (see Figure 14). Similar to the experiment, the drug solution exhibits a low permeation rate with less than 20% of the drug permeating in 40 minutes. As the values are in good agreement with those provided in the *in vitro* study, the uptake boundary condition is expected to predict the drug absorption in the nasal cavity with good accuracy.

CHAPTER 4: RESULTS AND DISCUSSION

The main thesis objective is to simulate and analyze the evolution of droplets and the associated spray dynamics when using a representative pressurized metered-dose inhaler (pMDI), eg, the Ventolin from GSK (UK). Modeling realistically polydisperse drug-aerosol inhalation as well as subsequent particle transport and deposition are crucial for targeted drug delivery. In addition to administering drugs orally, the fate of generic drugs from nasal sprays and their uptake in the nasal mucociliar layers are discussed as well.

4.1. Pressurized Metered Dose Inhaler – Ventolin

Ventolin is a pressurized metered dose inhaler manufactured by GlaxoSmithKline. It is primarily used for treating bronchospasm in children and adults. The propellant used is HFA134a and the active pharmaceutical ingredient (API) is 110 μg of Albuterol Sulfate (36). Ventolin is a suspension pMDI and hence the drug is suspended as a solid in the liquid propellant. Since, the suspension formulation is heterogeneous, it does not require a co-solvent such as ethanol. Brambilla et al. (28) reported the nozzle diameter and the metering volume of Ventolin to be 0.5 mm and 63 μl , while Alatrash and Matida (21) reported the length of the mouthpiece to be 25.32 mm. These parameters were used in designing the geometry for the spray characteristics study and in computing the total number of droplets and the mass fraction of the solid drug particles, which are described in the following section.

4.1.1. Spray Characteristics

Various factors such as the initial size distribution and evaporation of droplets influence the operation of a pressurized metered dose inhaler. To obtain reliable deposition characteristics, these factors must be taken into consideration and the various parameters of the spray need to be ascertained and validated using established results. As described in Chapter 1, many authors have succeeded in experimentally analyzing the characteristics of the spray. However, comprehensive evaluation of the spray dynamics may not be easy to accomplish using experimental techniques due to the time and cost involved. Computational tools, such as CFD software can use the parameters determined from the preliminary experimental study as input for CF-PD simulations or for validating the computational models. This approach was employed for all present pMDI-spray simulations.

A typical experimental study of the inhaler involves spraying the aerosol droplets in unbounded, quiescent air and analyzing the parameters downstream from the nozzle. The computational domain for this study is shown in Figure 15. It was meshed with 1.2 million hexahedral cells. The smaller cylinder represents a mouthpiece of diameter 20 mm and length 25 mm while the large one represents the ambient air.

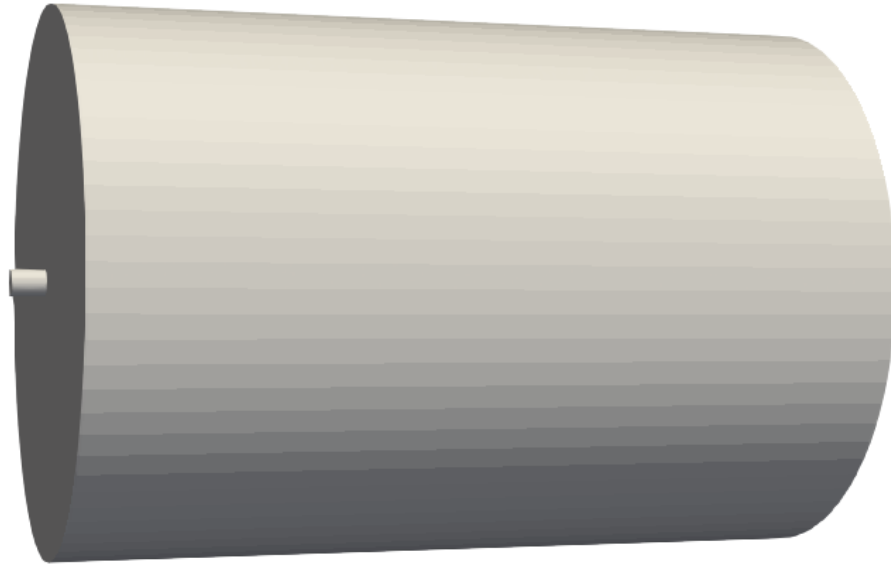


Figure 15. Computational domain for the spray characteristics study

The parameters used in the simulations are listed in Table 8, and their justification is provided in the subsequent sections using validated spray characteristics.

Table 8. Parameters used in the spray simulations

Parameter	Value
Initial diameter distribution	Rosin-Rammler: Mean = $4.5 \mu m$, Spread = 1.315
Initial spray velocity (m/s)	150
Spray angle (degrees)	20
Initial droplet temperature (K)	245
Spray duration (ms)	160 (refer (37))

The metering volume of Ventolin is $63 \mu\text{l}$ for which Finlay (66) noted that 45 % of the mass of the formulation transforms into vapor before exiting the nozzle. Considering the diameter distribution mentioned in Table 8, the number of droplets turns out to be 240 million. Such a high number of droplets makes it unfeasible for effective computational analysis. Thus, 80000 droplets were injected in all the simulations while the source terms due to parcels in the governing equations were amplified by a factor of 3000 to ensure the effect of 240 million droplets. Ventolin contains HFA134a as the propellant and $120 \mu\text{g}$ of the drug, Albuterol Sulfate. For the simulations, each liquid propellant droplet was assumed to contain one solid drug particle with a density of 1200 kg/m^3 and a mass fraction of 0.0024.

Droplet Diameter

In their experimental characterization of the Ventolin pMDI, Alatrash and Matida (21) noted that the Rosin-Rammler distribution fitted the diameters of the droplets much better than other functions. The Rosin-Rammler distribution is used to describe the distribution of crushed coal particles and pharmaceutical aerosols and its probability density function is given by Equation 4.1.

$$PDF = \left(\frac{k}{\lambda}\right) \left(\frac{x}{\lambda}\right)^{k-1} e^{-\left(\frac{x}{\lambda}\right)^k} \quad (4.1)$$

Where x is the diameter of the droplet, λ is the mean diameter of the droplets and k is the spread parameter.

Alatrash and Matida (21) were able to fit a Rosin-Rammler distribution with λ as 4.071 and k as 1.315 for the diameters of the droplets observed along the centerline, at the mouthpiece exit. In a

typical inhaler, the length of the mouthpiece i.e. the distance between the nozzle and the mouthpiece exit is 25 mm. Thus, to simulate the evolution of the spray, the size distribution needs to be translated back from the mouthpiece exit to the nozzle. Such data is not available for the Ventolin inhaler at present and hence, the mean diameter λ was increased from 4.071 to 4.5 μm in the distribution function to account for evaporation and to obtain good agreement with the diameters reported downstream. The Rosin-Rammler distributions used in the present study and by Alatrash and Matida (21) are shown in Figure 16.

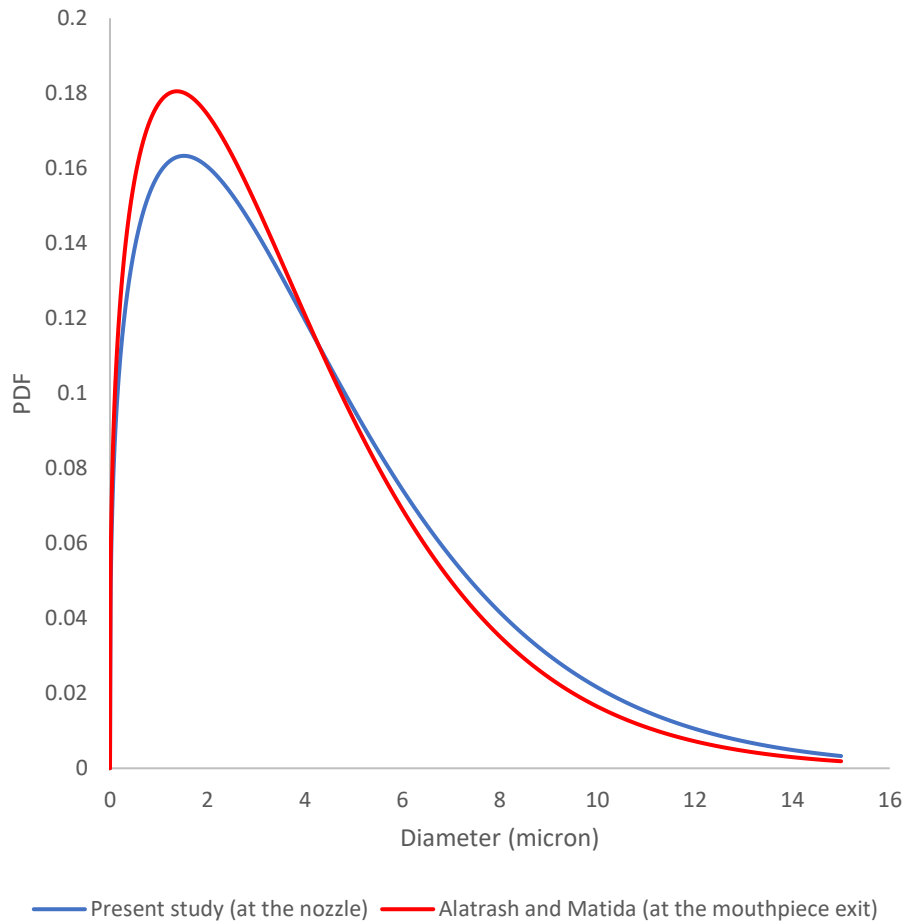


Figure 16. Rosin-Rammler distribution functions

The average diameter (D_{10}) of the droplets obtained from the simulation and those reported in the experimental study are listed in Table 9. The values show reasonable agreement with the experimental results, given the polydispersity of the droplets and the complexities involved in modeling droplets as a mixture of the liquid propellant and the solid drug.

Table 9. Average droplet diameter values

	25 mm from the nozzle (mouthpiece exit)		100 mm from the nozzle	
	Experiment	Present study	Experiment	Present study
D_{10} (μm)	3.75	3.46	1.84	2.54

Droplet Velocity

To fix the injection velocity of the spray, the values were iteratively adjusted to match the values reported downstream. An injection velocity of 150 m/s, which has been used in previous computational studies (8), was deemed suitable after it showed good agreement with the experimental results of Alatrash and Matida (21) (see Table 10).

Table 10. Droplet velocities downstream of the spray

	25 mm from the nozzle (mouthpiece exit)		100 mm from the nozzle	
	Experiment	Present study	Experiment	Present study
Velocity (m/s)	43.20	43.21	13.39	10.62

The velocity of the droplets along the centerline exhibits a sudden decrease in the value when it encounters motionless air and then reduces more gradually as the distance from the nozzle increases and the relative velocity between the droplets and air decreases. Figure 17 shows the trend of the droplet velocity along the centerline and the distance travelled by the spray.

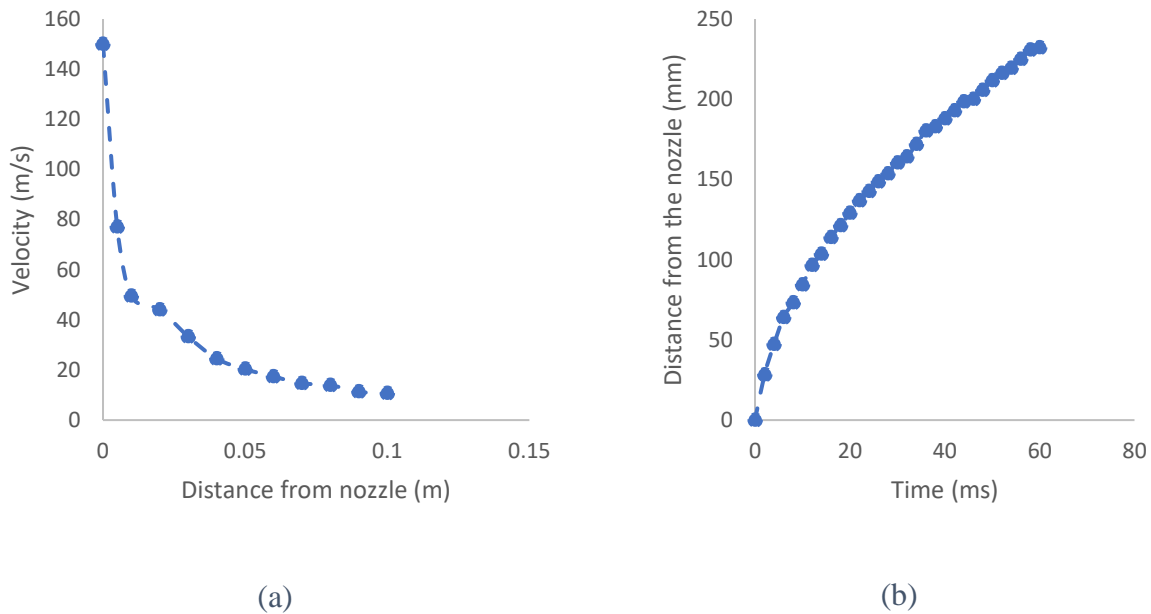


Figure 17. (a) Droplet velocity along centerline (b) Distance travelled by the spray

The radial profiles of the average velocity at various axial locations are presented in Figure 18. The plots also provide a quantitative picture of the increasing height of the plume. The high velocity at the centerline decreases as the distance increases, which is indicated by the flattening of the curve near the centerline. The velocity of the droplets above and below the centerline are low at all the axial distances because of the shear effect of the surrounding still air. As the spray emerges from a small orifice, the droplet density near the centerline is high and as a result, the total momentum contained in the droplets is high. Due to the coupled nature of the flow, this high

momentum is transferred from the droplets to the quiescent air thus, reducing the relative velocity and the rate of deceleration of the droplets.

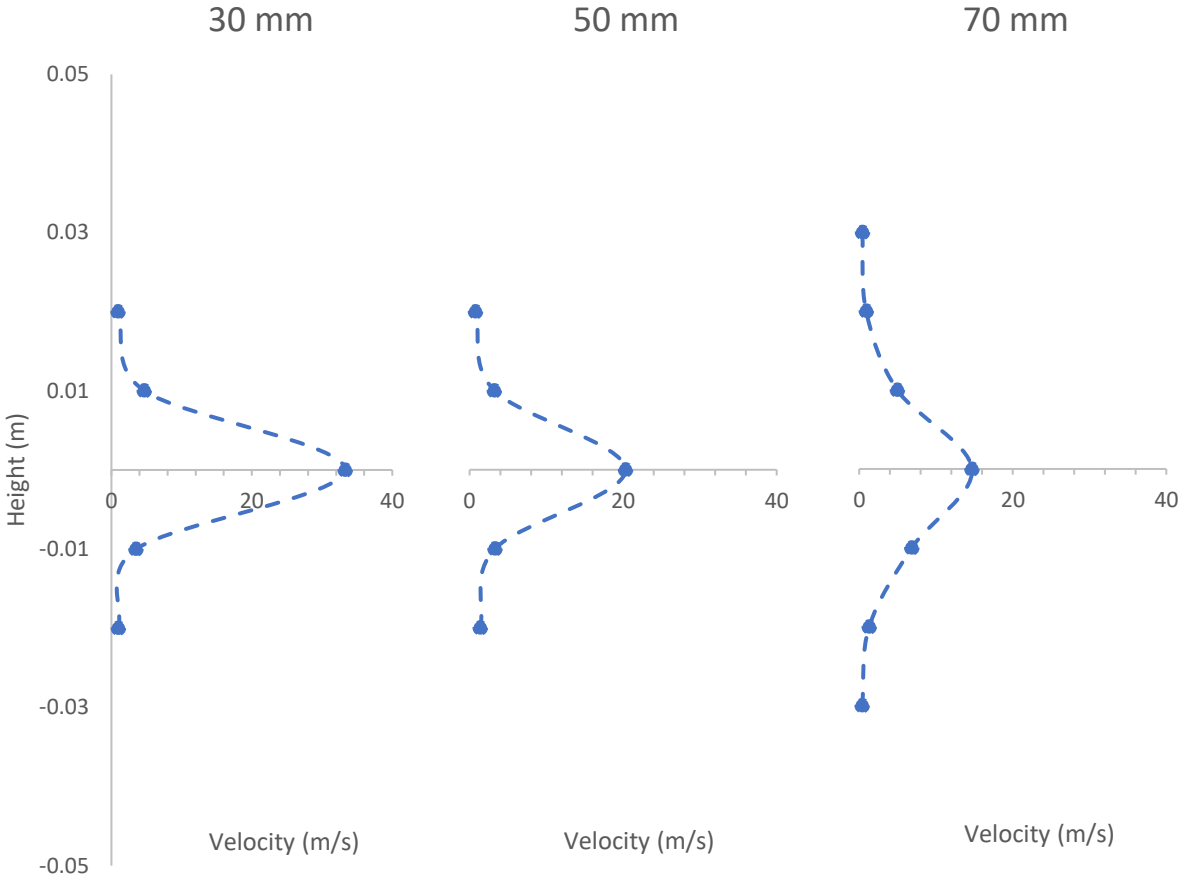


Figure 18. Velocity profiles in the radial direction

Figure 19 shows the expansion of the spray plume at various time levels. The velocity of the spray quickly drops as it exits the nozzle. The spray angle and the enhanced turbulent dispersion of the smaller particles result in the expansion of the spray away from the centerline (67). Thus, as the

droplets move farther away from the centerline, the number density of droplets decreases which was observed in experimental studies as well (68).

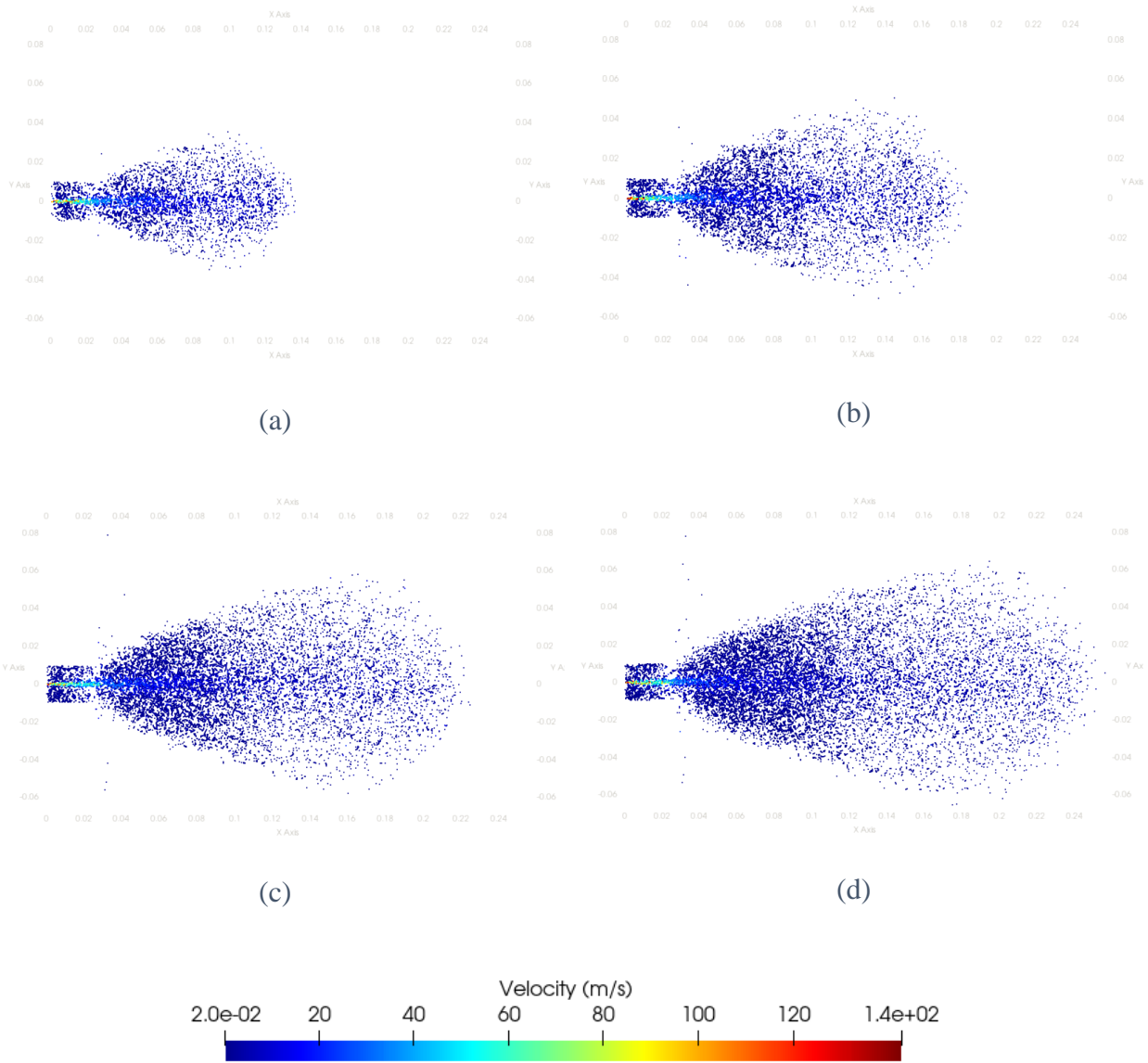


Figure 19. Velocity of droplets after (a) 16 ms (b) 30 ms (c) 46 ms (d) 60 ms

As the high velocity spray expands at an angle from the nozzle, it first traverses the length of the mouthpiece before encountering the much larger volume of ambient air. The mouthpiece provides a highly constricted path for the flow of the aerosols and air and hence is a prominent zone for

recirculatory flow of air outside the path of the expanding spray. The use of the mouthpiece is to position the inhaler in the oral cavity which also has a smaller cross-section. The recirculatory flow in the present simulation at a section at 15 mm from the nozzle is illustrated in Figure 20 that shows a reversed flow of magnitude 5 m/s. Such recirculatory flow aid the backward flow of aerosols, thus resulting in drug wastage.

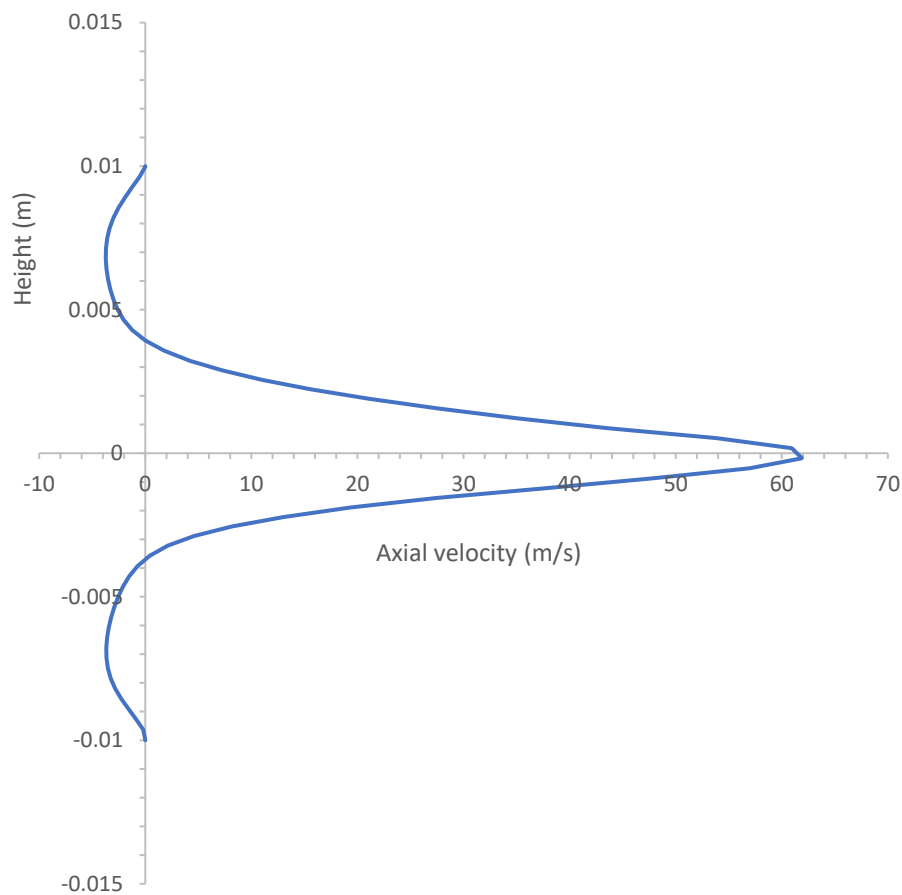


Figure 20. Recirculatory airflow at 15 mm inside the mouthpiece

Droplet Temperature

The droplets exiting the nozzle contain the liquid propellant and the solid drug particle. Due to the high vapor pressure and low boiling point of the propellant, a single droplet evaporates in under 3 ms as described in Section 3.3. Typically, the temperature of the evaporating droplet reduces below the boiling point to the wet bulb temperature, at which point the heat absorbed by the droplet balances the latent energy leaving it. For the HFA134a propellant, the wet bulb temperature is around 214 K. After complete evaporation of the propellant, the temperature of the droplet and the surrounding medium increase to the ambient value. Thus, the temperature of the droplets near the centerline increase as the distance from the nozzle increases. The temperature of the droplets predicted by the simulation was found to be in good agreement with the experimental results reported by Gabrio et al. (14) as shown in Table 11.

Table 11. Droplet temperature near the centerline

	75 mm from the nozzle	
	Experiment	Present study
Temperature (K)	242.8 ± 5.0	237.58

The radial temperature profiles at various axial locations are presented in Figure 21. The increase in the temperature with distance from the nozzle is evident from the flattening of the curve.

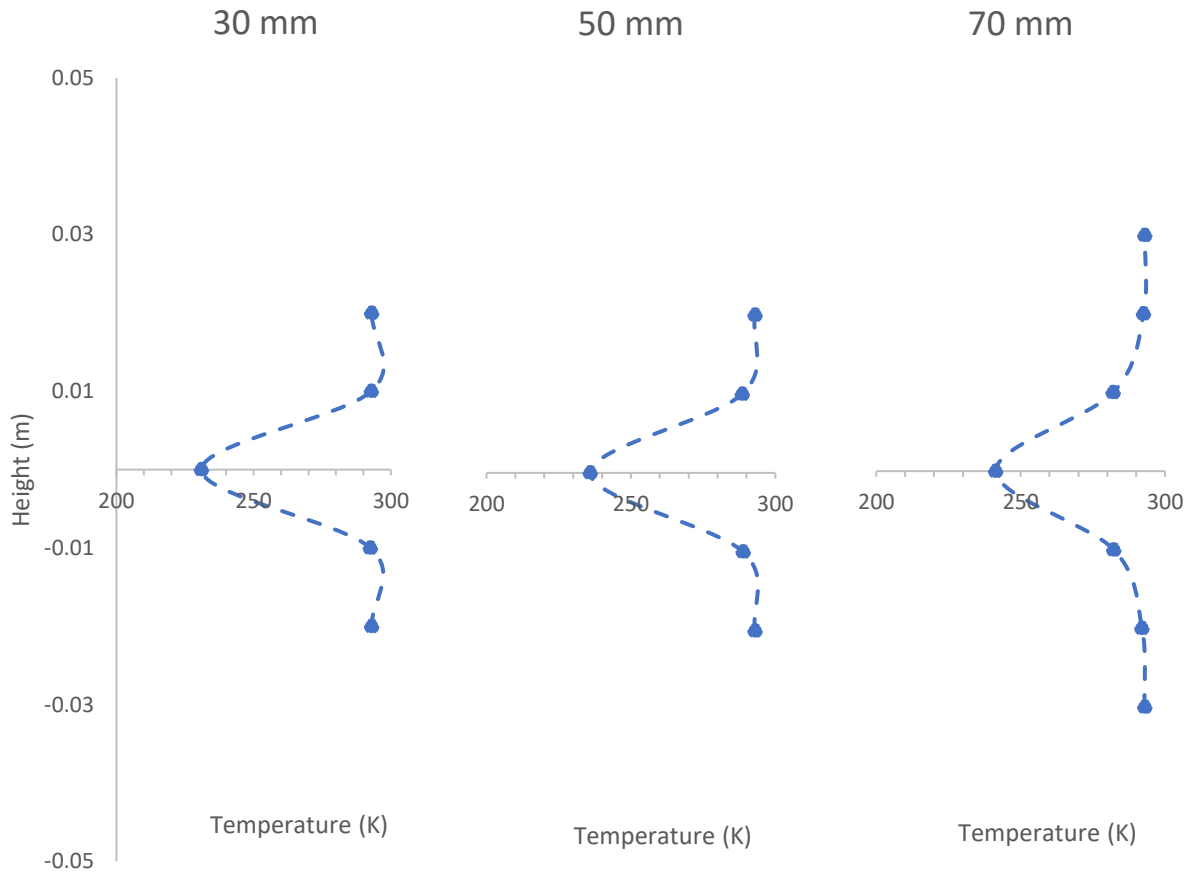


Figure 21. Temperature profiles in the radial direction

As the spray expands, the droplet density decreases which results in lesser propellant concentration in the surrounding air and faster evaporation. Thus, the temperature of the droplets away from the centerline reaches the ambient value very quickly. The faster evaporation of the droplets away from the centerline results in smaller residual drug particles with lesser momentum, which in turn explains the slower velocity of the droplets. The temperature distribution of the aerosol plume after 60 ms is shown in Figure 22.

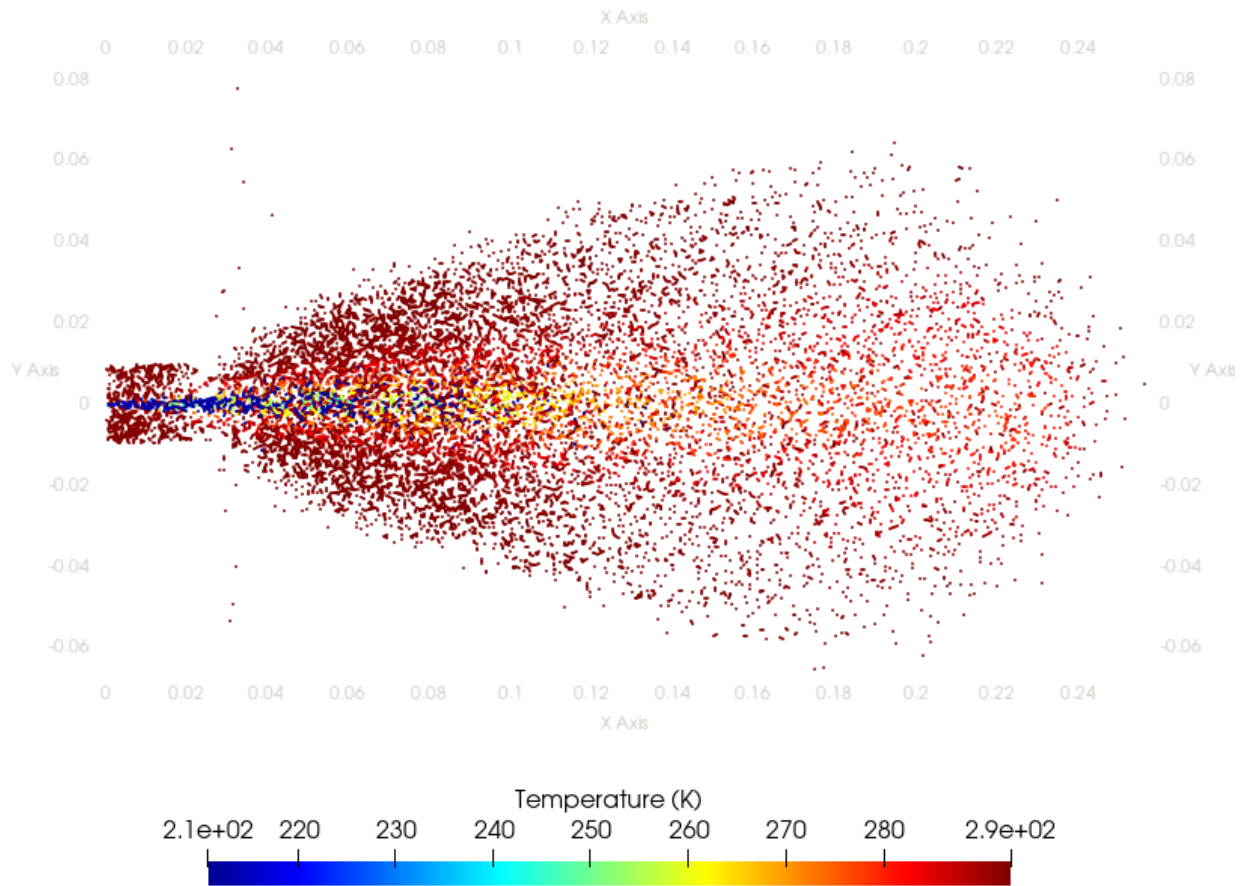


Figure 22. Temperature distribution at 60 ms

4.1.2. Oral Cavity Drug Deposition

After validating the characteristics of the spray from the Ventolin pMDI, deposition studies were conducted in a 3D representative geometry of the mouth-throat segment in accordance with previous *in vitro* testing of pMDIs. The injection parameters that were validated in the previous section were used in the deposition studies. Various researchers have obtained the deposition percentages of the drug from pMDIs using experimental and computational techniques. However, the available experimental studies do not provide deeper insight into the fate of the sprayed aerosol droplets beyond the deposition fraction of the drug on the walls of the oral cavity model.

Computational studies, traditionally, have used unvalidated injection parameters to simulate deposition in a 3D computer generated model of the oral cavity. While such studies are somewhat useful in providing the deposition pattern and in analyzing the effect of the injection parameters, they do not provide additional information regarding the deposited droplets. For instance, the temperature and the mass of the propellant remaining in the deposited droplets are interesting parameters to analyze as previous *in vivo* experiments have shown that the low temperature of the droplets impacting the throat make patients feel uncomfortable. The use of validated and realistic thermo-mechanical parameters of the spray for simulating the deposition of spray aerosols will help in providing additional insights into the behavior of the spray droplets inside the oral cavity. The deposition simulations were first validated with the experimental results of Biswas et al. (36) for selected cases. A 3D computational model of an inhaler attached to the mouth-throat segment of the oral cavity generated from MRI scans (see Figure 23) similar to the model used in the experimental study (see Figure 4), was meshed with 1.2 million tetrahedral elements. The inhaler was tilted at an angle of 20° to prevent impaction on the tongue.



Figure 23. 3D computational model of the oral cavity

Realistic inhalation waveforms were approximated using trapeziums as shown in Figure 24 and used in the experimental and the present computational studies. These waveforms cover the acceleration, breath-hold and deceleration phases generally seen in one cycle of inspiration.

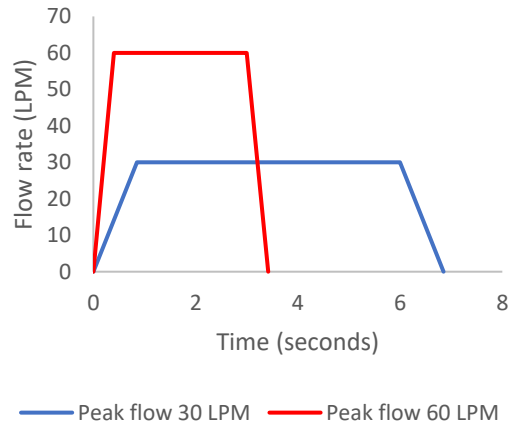


Figure 24. Inhalation waveforms

The flowrate condition was specified on the annular surface at the top of the inhaler. The pMDI was actuated at time $t_a = 0.6 \times t_r$, where t_r is the time taken to achieve peak flowrate. The position of the nozzle and the orientation of the spray fixed in this study are marked in Figure 25. The 3D model and the specifications of the spray nozzle were used in all the simulations conducted.

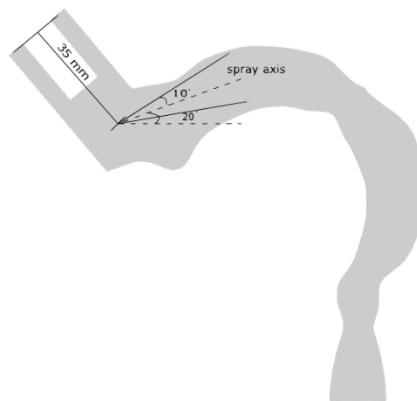


Figure 25. Origin and the orientation of the spray

In these simulations, the air was at 293 K and the lung walls were assumed to be insulated, not considering the mucus layer thermodynamics. The deposited droplets contain a mixture of the evaporating propellant and the drug. The mass fraction of the deposited drug is calculated as shown in Equation 4.2 using the mass of the drug rather than the number of particles deposited which was used in previous studies (8). The mass of the drug was post-processed using the mass fraction of the drug in the deposited aerosol as predicted by the simulations.

$$DF = \frac{\text{mass of drug deposited}}{\text{mass of drug sprayed}} \quad (4.2)$$

Biswas et al. (36) notes that the remainder of the drug would get deposited in the lungs and hence, computes the lung deposition fraction as $1 - DF$. The deposition fractions of albuterol sulfate from Ventolin pMDI obtained from the CFD simulations are presented in Figure 26 along with the experimental results. Considering the complexity of the spray process, the transient inhalation waveforms and possible differences in the geometry, the results obtained from the simulations match well with the experimental data for the cases presented. This validation of the deposition results further improves the credibility of the models used and hence, they can be used in any future work involving spray inhalers containing an evaporating propellant.

As highlighted in the previous sections, the mean diameter of the spray droplets is 4.5 μm . The high velocity of spray reduces the deposition of the drug in the lungs. Contrasting the spray with the deposition of passively inhaled non-evaporating droplets or particles, the latter results in over 80% deposition in the lungs for the same diameter and the flowrates (34). However, at such low velocities, passive inhalation of drug particles may not be able to deliver the same dosage of drug as a spray inhaler in the duration of inhalation, which is a major reason for the popularity of spray

inhalers despite the high oropharyngeal deposition. Clearly, novel systems which reduce the spray momentum without compromising the delivered dosage are required to improve drug delivery. One such technique called ‘pulsed injection’ was developed and analyzed computationally in this research study.

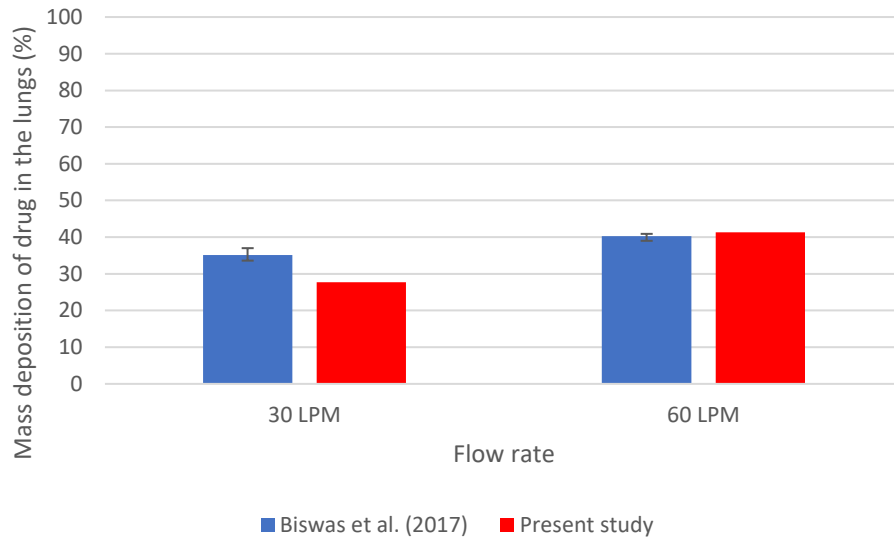


Figure 26. Comparison of the drug deposition between simulations and *in vitro* study

Effect of Flowrate

The experiments conducted by Biswas et al. (36), which were used for validation involves transient inhalation waveforms. To understand the effect of the inspiratory flowrate better, simulations were run for steady inhalation cases. The pMDI was actuated at 0.3 seconds into the inhalation when the flow had become steady in the oral cavity. The velocity contours on the slice taken on the mid-plane of the geometry for flowrates of 30 LPM and 60 LPM are presented in Figure 27. The glottis constriction results in an increase in the flow rate and the turbulence in both the cases.

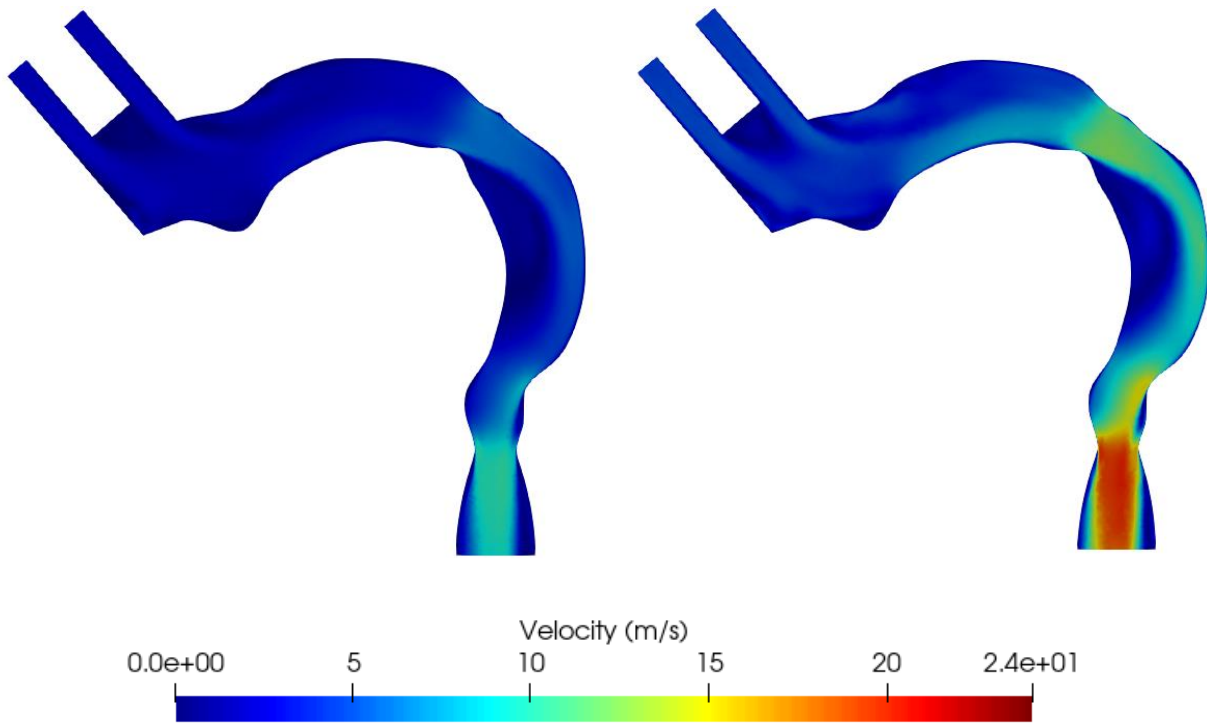


Figure 27. Velocity fields for a) 30 LPM b) 60 LPM

The deposition fractions of the drug in the lungs for the flowrates simulated are reported in Figure 28, which show the pattern of the deposited particles. The increase in the inspiratory flowrate reduces the relative velocity between the spray and the surrounding air and hence, the air guides more spray droplets into the lungs, preventing impaction at the back of the throat. Thus, the fraction of the drug reaching the lungs is higher for the inspiratory flowrate of 60 LPM.

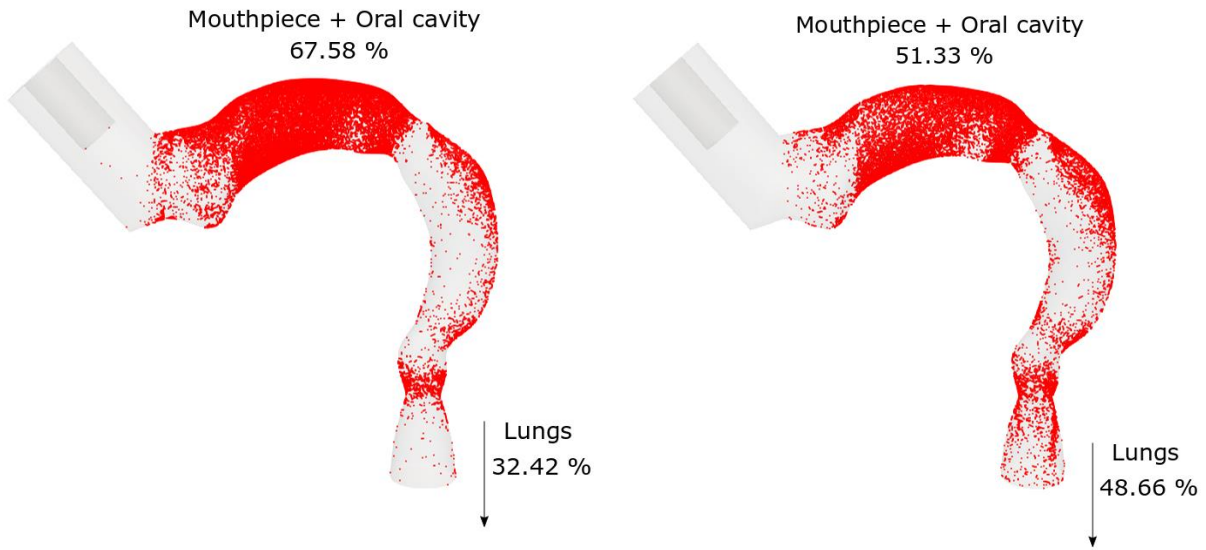


Figure 28. Deposition pattern for a) 30 LPM b) 60 LPM

To analyze further, the oral cavity was segmented into 7 parts as shown in Figure 29. Such segmentation can provide useful deposition data which can later be used for studying drug absorption in the oral mucus layers while providing more insight into the behavior of the spray in a confined geometry. The segments measured 20 mm in the horizontal and vertical directions.

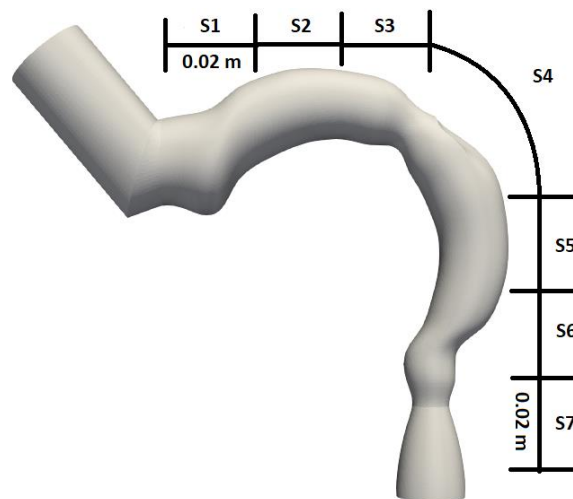


Figure 29. Segments in the oral cavity geometry

The mass deposition fractions of the drug are plotted for each of the segments in Figure 30. The path of the spray makes the segment S3 the target for aerosol impaction and hence, it records the highest deposition of the drug in the oral cavity for both the flowrates. However, the deposition in the segments S1 and S2 is significantly low for the flowrate of 60 LPM. The high velocity of the surrounding air limits the spray expansion inside the oral cavity. Thus, the reduced relative velocity between the flow and the spray at higher flowrates decreases the magnitude of recirculatory flow in the segments closer to the origin of the spray. However, in the case of 30 LPM, the recirculatory flow is strong enough to make large and small particles deposit in high numbers in S1 and S2.

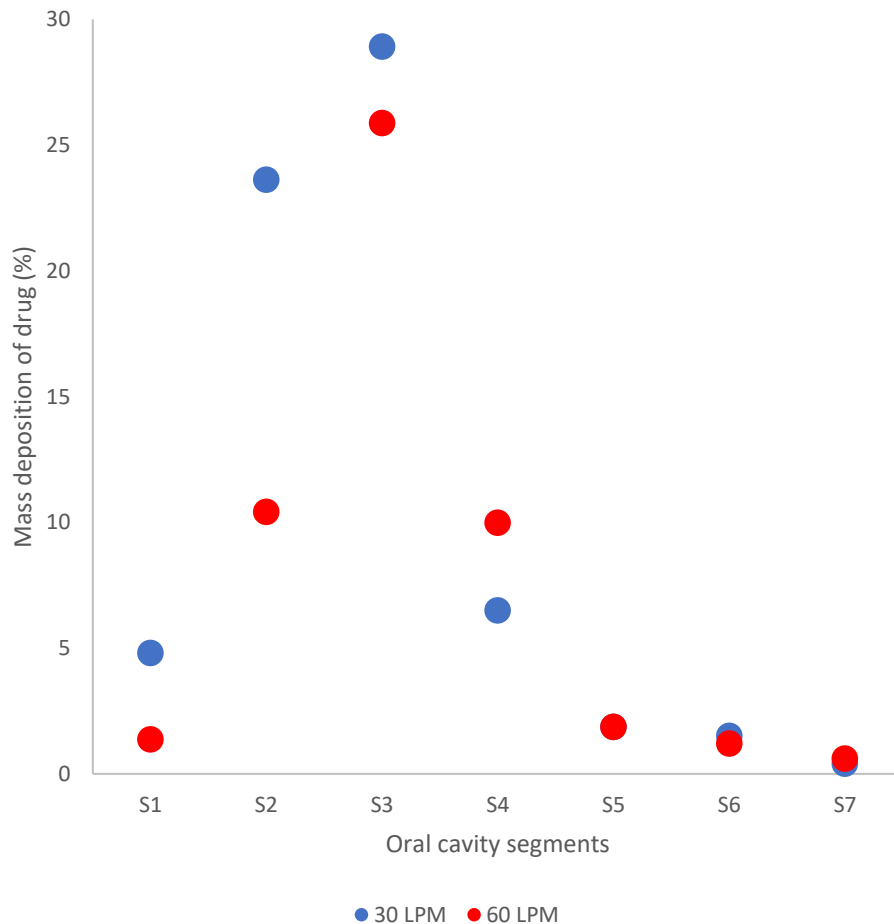


Figure 30. Segmental deposition of the drug in the oral cavity

A common problem with pMDIs is the impaction of cold droplets due to the evaporation of the propellant. In this study, the temperature of the droplets was analyzed as well to understand the influence of flowrate. In general, the temperature of the deposited aerosol increases with an increase in the inspiratory flowrate as shown in Figure 31.

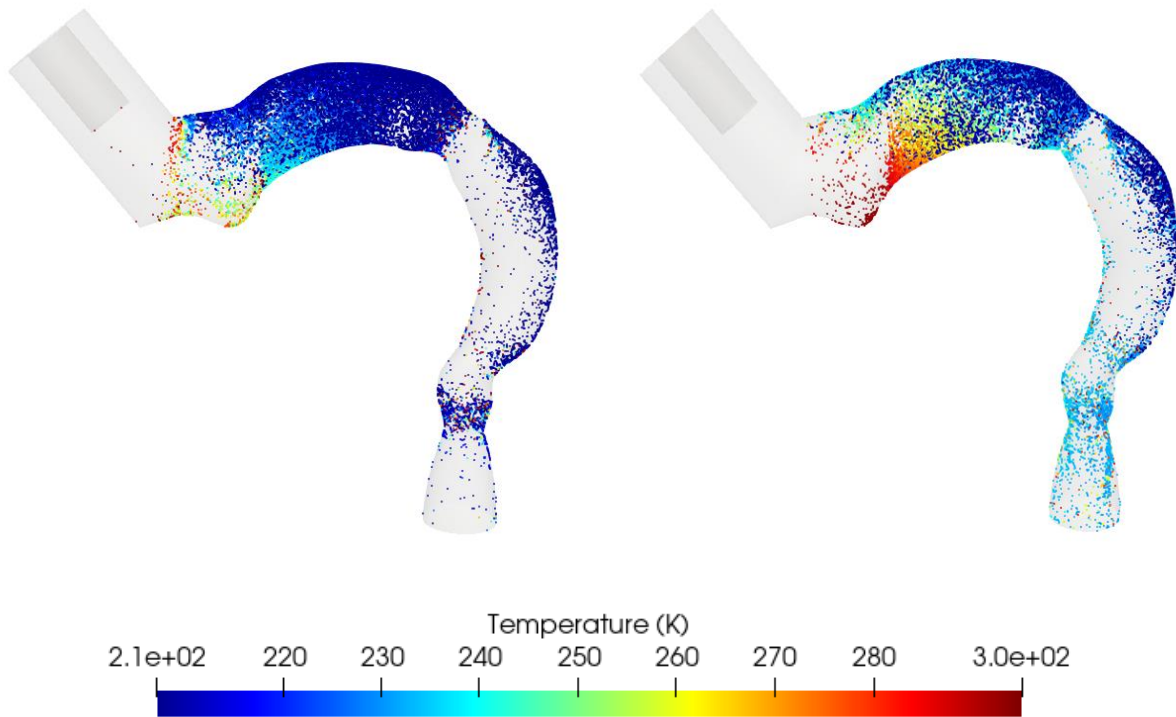


Figure 31. Temperature of deposited aerosol for a) 30 LPM b) 60 LPM

The variation of the temperature of the droplets in the segments is shown in Figure 32. With an increase in the flowrate, the convective flow around the droplets improves and hence, results in faster evaporation and higher temperatures. The increase in the temperature is more significant in the lower segments than S3. This is because the droplets depositing in the lower segments have greater residence times which allow for complete evaporation of the propellant. The temperatures

of the aerosol in the segments S1 and S2 are higher as well for a flowrate of 60 LPM. As mentioned before, the reduced recirculatory flow ensure the deposition of the smaller droplets primarily and provide adequate time for the evaporation of the propellant.

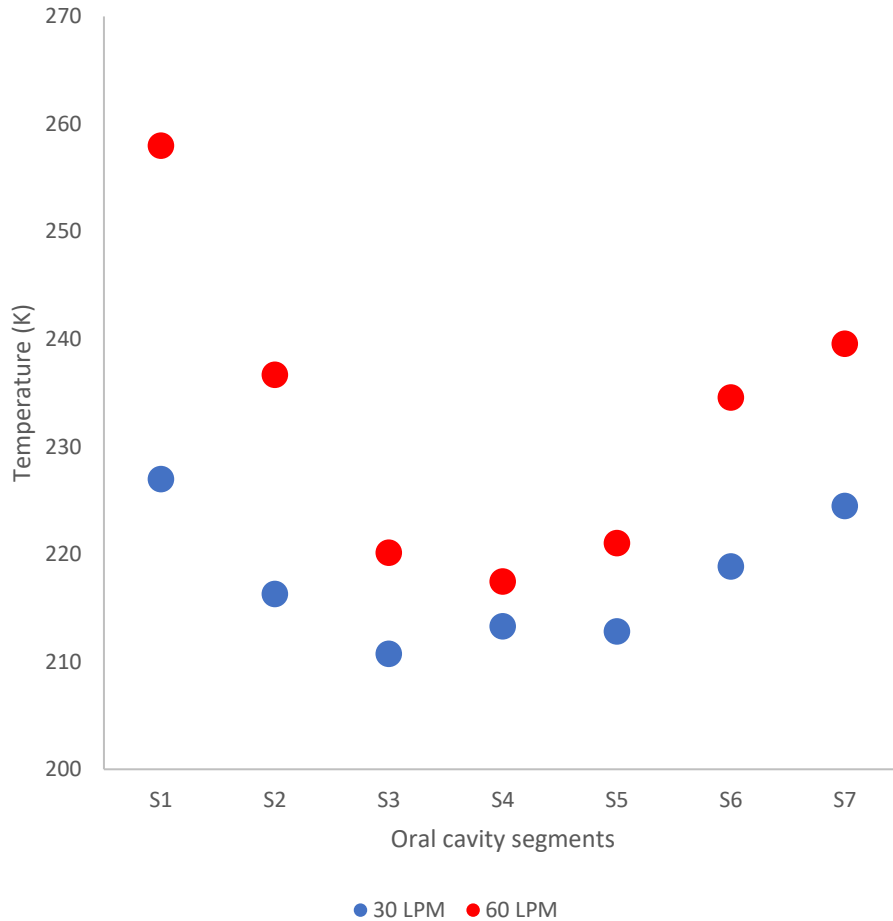


Figure 32. Segmental variation of temperature of deposited aerosol in the oral cavity

4.1.3. Pulsed Spray Injection

Increasing the inspiratory flowrate was shown to be a promising option to reduce the oropharyngeal deposition and the temperature of the droplets by reducing the relative velocity and increasing the residence times. However, a patient with a respiratory problem may not be able to

inhale faster than 60 LPM. The major contributor to the high deposition in the mouth-throat segment is the high momentum of the spray. Thus, reducing the momentum of the spray will result in low oropharyngeal deposition by impaction and provide longer times for the evaporation to complete. A number of parameters such as the spray duration, velocity and droplet sizes can be decreased to reduce the momentum; however, these parameters are heavily dependent on the drug and propellant formulation, as well as complex thermodynamic processes that happen inside the inhaler device. Traditionally, spacer devices have been used to reduce the velocity of the droplets but the deposition in these devices have been known to be high, resulting in the wastage of drug (34, 69).

One useful technique for achieving the target of lesser oropharyngeal deposition without changing the formulation or the addition of spacers is pulsed injection. In this method, the entire spray is broken up into pulses of smaller duration with a delay between 2 consecutive pulses. Traditionally, the entire mass of the drug is sprayed, all at once. This technique will involve redesigning the inhaler device with microelectromechanical actuators to generate pulses of the spray at precise time instants and hence, the experimental viability is yet to be established. However, the computational analysis of the pulsed injection technique was conducted for the purpose of this research.

The number of injections tested were 4 and 8 with delays of 20 ms, 50 ms and 100 ms. The duration of each pulse was 40 ms and 20 ms for 4 and 8 injections, respectively. The spray duration of a single injection of Ventolin pMDI was 160 ms. The deposition results of the pulsed injection cases are presented in Figure 33 in comparison with the conventional single injection.

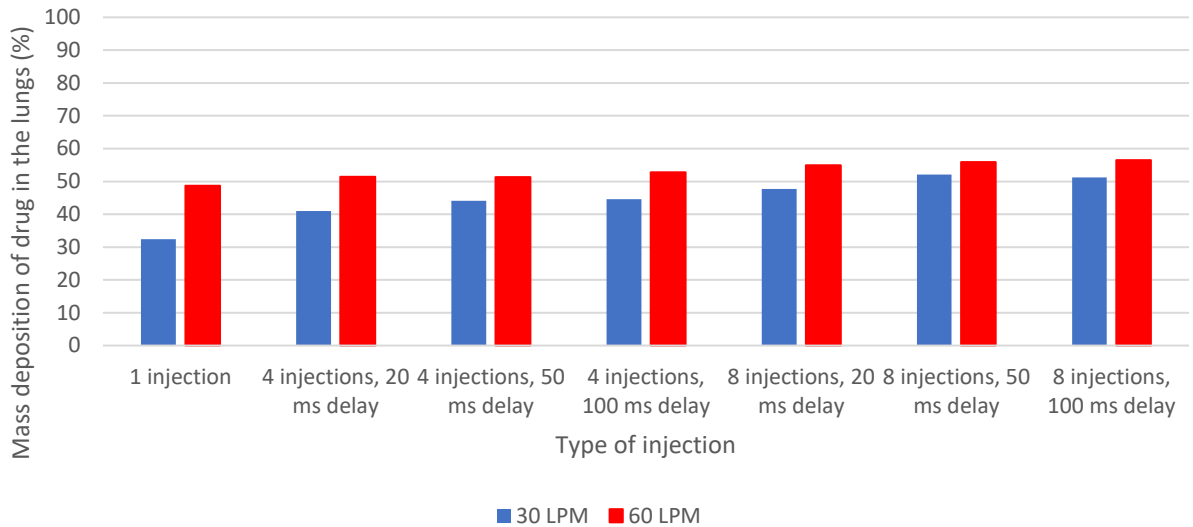


Figure 33. Comparison of lung deposition fractions of drug with pulsed injection

As the number of injections and the delay between the pulses increase, the momentum of the spray reduces even more and hence, results in an increase in the deposition in the lungs as shown in Figure 33. In the case of 30 LPM, an increase of 20% can be seen while the increase is around 10% for 60 LPM. The increase in deposition is not of the same magnitude for 60 LPM as it is for 30 LPM. A possible reason is that the reduction of the momentum results in the gradual increase in dominance of inertial impaction due to the higher flowrate in comparison with the ability of the airflow to blanket and the guide the spray to the distal regions, which was seen in the case of the conventional single injection.

The segmental variation of temperature of the deposited aerosol for the pulsed injection cases are presented in Figures 34 and 35. Pulsed injection results in longer residence times for the droplets which in turn aid the complete volatilization of the propellant. The additional benefit of increased airflow around the evaporating droplets in the case of 60 LPM inspiratory flowrate results in a maximum increase in temperature of 20 °C when the spray is broken into 8 pulses with 100 ms

delay between them. In general, the temperatures are higher with pulsed injection compared with the conventional single injection. The temperature of the droplets in the first 2 segments are higher as well. This is because of the enhanced convective flow due to strong recirculatory flow in this region of the oral cavity.

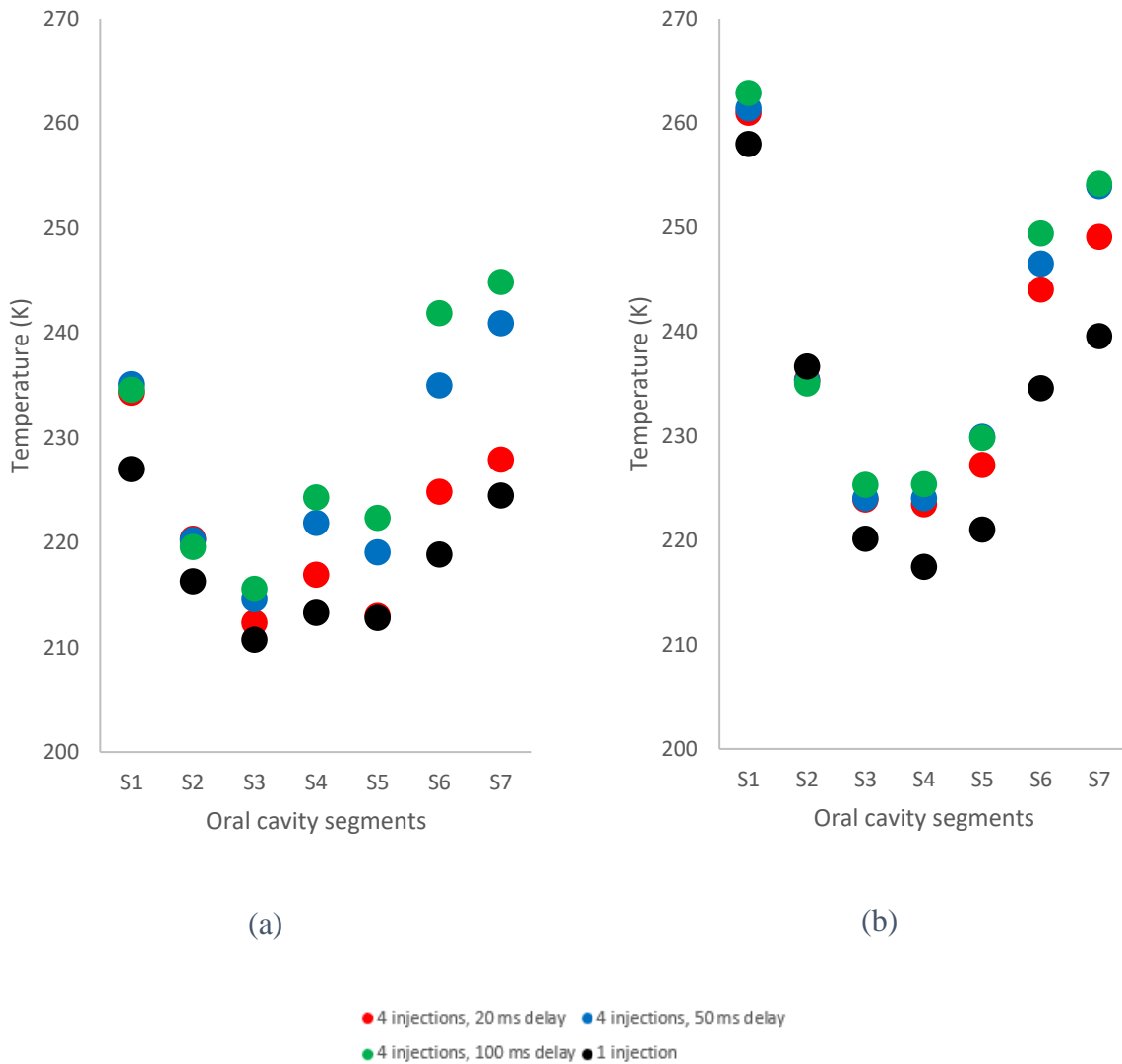


Figure 34. Segmental temperature of aerosol with 4 injections for a) 30 LPM b) 60 LPM

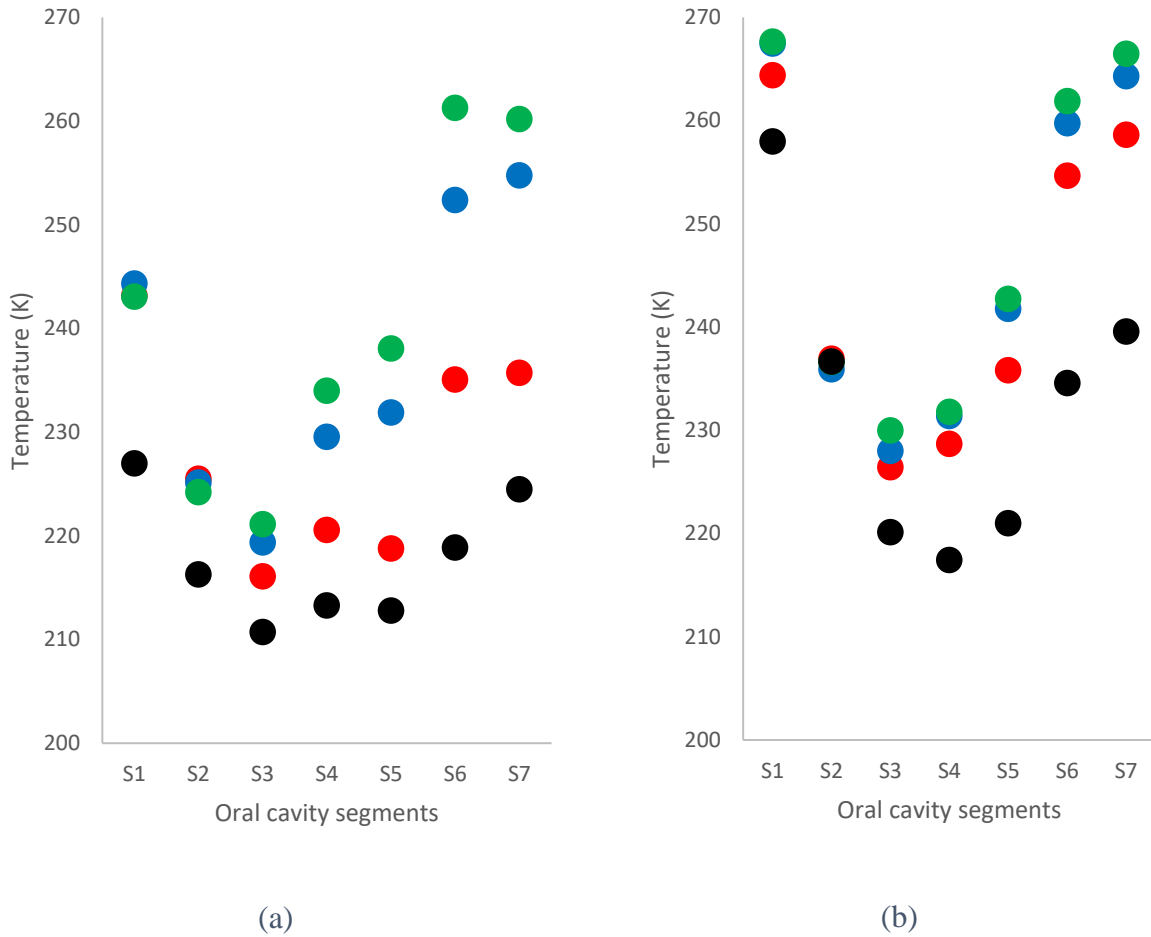


Figure 35. Segmental temperature of aerosol with 8 injections for a) 30 LPM b) 60 LPM

These results prove the effectiveness of the pulsed injection technique and its ability to reduce the ‘cold-freon’ effect that is seen when cold aerosol droplets impact the oropharynx. Since this technique reduces the momentum of the spray, it could be coupled with a spacer device to reduce the velocity even further to result in lower device and throat deposition, and higher temperatures. The efficacy of this method shall be analyzed in future endeavors.

4.2. Nasal Epithelial Drug Uptake

The drug absorption at the nasal epithelium is essential for treating ailments through systemic circulation. The amount of drug that is available for uptake depends mainly on the solubility of the drug. After dissolution, the drug needs to cross the epithelial barrier, which favors the lipophilic drugs, to reach the systemic circulation. Thus, a comprehensive analysis of the effect of various parameters on the absorption characteristics is required to design better drug formulations and inhaler devices.

4.2.1. Airway Surface Liquid Layers Mesh

The airway surface liquid (ASL) comprises of two layers namely the periciliary sol and the mucus as shown in Figure 5. The two layers have different viscosities and hence, two separate meshes were created to obtain the velocity fields. The *extrudeMesh* utility in OpenFOAM was taken advantage of to create the two layers of the ASL as separate structured extrusions from a mesh of the nasal cavity. However, for analyzing the drug absorption at the epithelium, a single extrusion of double the size, comprising of the two layers, was created. The unique numbering scheme of cells in OpenFOAM allowed combining the individual velocity fields of the two layers using a script in Python. The final mesh of the airway surface liquid layers is shown in Figure 36. The thin dark line that is present on the boundary of the nostrils in Figure 36a is the ASL. The magnified image of the structured layers across the ASL is shown in Figure 36b.

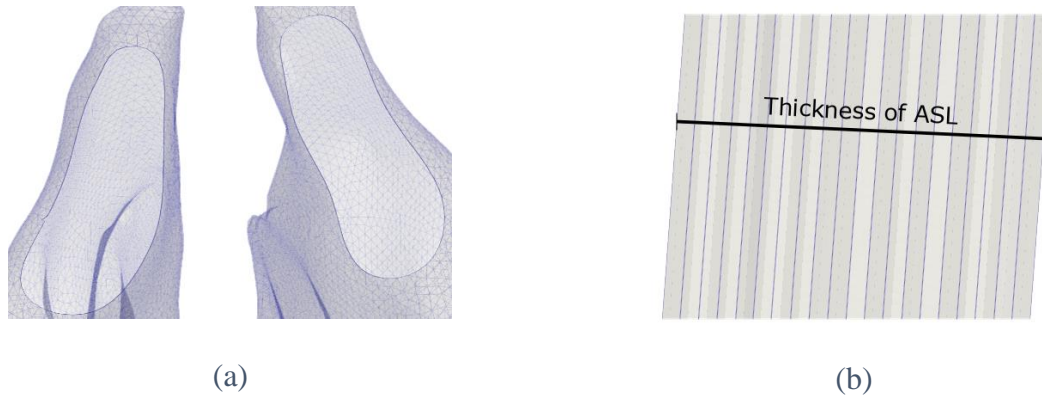


Figure 36. a) Airway surface liquid lining around the nostrils b) Magnified section

4.2.2. Velocity Fields

As mentioned, the velocity fields were obtained separately for the mucus gel layer and the watery periciliary sol layer. This approach was preferred to account for the different viscosities in the two layers and the mucus production in the gel layer. The synchronous beating of the cilia propels the mucus layer towards the nasopharynx at an average velocity of 2-25 mm/min, which in turn drags the sol layer. Thus, a wall-driven velocity of $1e-4$ m/s in the natural direction of flow (see Figure 37) was specified on the bottom and the top surfaces of the ciliated posterior regions for the mucus and sol meshes respectively to simulate the cilia movement at the interface of the two layers.

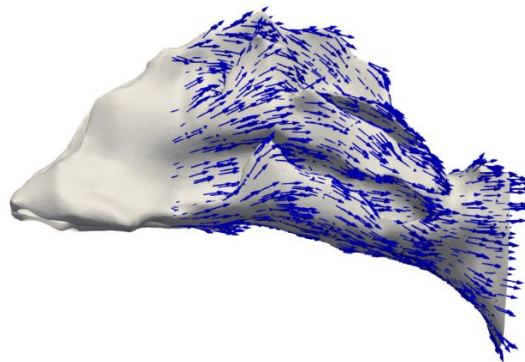


Figure 37. Wall-driven velocity vectors in the posterior region

The average amount of mucus secreted by the goblet cells in the respiratory epithelium is around 15-40 ml/day (70, 71). Halama et al. (72) noted that the maxillary sinus present near the olfactory region produced a large amount of mucus due to the high density of ciliated cells. To simulate the mucus secretion, a velocity of magnitude $5e-8$ m/s was specified for the mucus layer mesh in the direction normal to the faces on the olfactory patch.

To analyze the velocity fields, the average velocity magnitudes were plotted along the axial direction for the various segments marked on a slice of the geometry as shown in Figure 38. The slice presented is at 30 mm from the location of the nasal valve, which is the location of partition of the geometry into the nasal vestibule and the ciliated posterior regions.

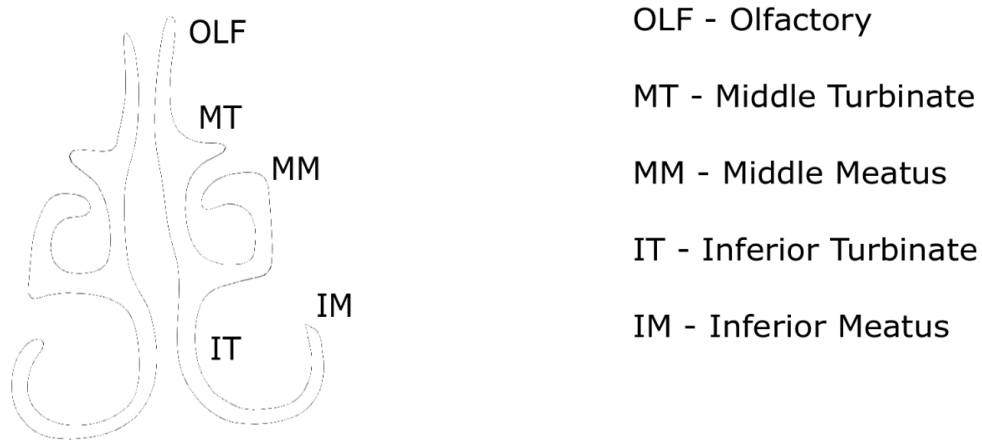


Figure 38. The different segments on the nasal cavity slice

The axial variations of the velocity magnitudes for the different segments in the left and right nasal cavities are shown in Figure 39. Asymmetry of the geometry results in slightly different profiles of velocity in the right and the left cavities. The velocity magnitude in the olfactory region is higher than the others at most of the axial locations because of the additional face-normal component of the velocity specified to simulate the mucus secretion.

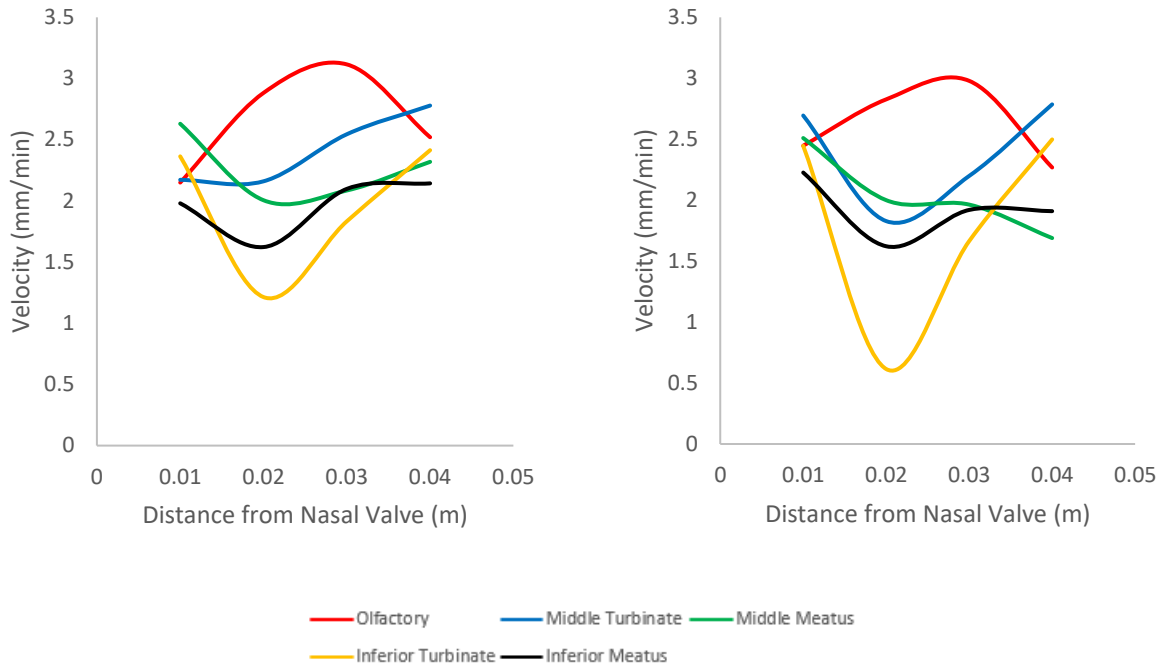


Figure 39. Axial variation of velocity for the segments in a) right and b) left cavity

The velocity of the mucus layer was validated by comparing the data obtained from CFD simulations with the results of the *in vivo* study conducted by Shah et al. (73). The experiment was conducted on human volunteers using radio-labelled drug particles administered *via* nasal spray pumps. The authors noticed that 75% of the mass of the drug was removed within 60 minutes. As the radio-labelled drug particles cannot dissolve, the authors concluded that the mass removal was due to mucociliary clearance in which the synchronous beating of the cilia move the mucus layer and the particles trapped inside, towards the nasopharynx. The velocity of the mucus layer plays an important role in advecting the dissolved drug in addition to sweeping away whole drug particles. The results of the one-way coupled CFD simulations were compared with the *in vivo* study, and the values are listed in Table 12 and plotted in Figure 40.

Table 12. Comparison of the mass remaining in nasal cavity with experimental results

Time (minutes)	% Mass remaining in the nasal cavity	
	Shah et al. (73)	Present study
15	41.11 (18)	49.27
20	37.02 (17)	36.45
30	30.71 (14)	25.50
45	26.42 (11)	21.15
60	25.00 (15)	19.76
90	23.04 (10)	18.61
120	20.54 (9)	15.56
180	17.37 (7)	13.15
360	13.32 (7)	13.14

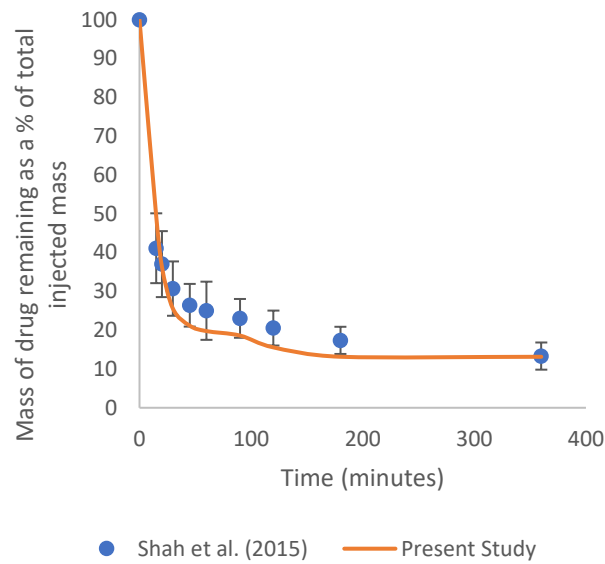


Figure 40. Validation of the nasal mucus layer velocity field

The results obtained from the CFD simulations match well with the data from the *in vivo* study. The computed velocity field predicts the mass remaining in the nasal cavity due to mucociliary clearance with great accuracy and hence, the velocity field was deemed suitable for conducting the drug uptake studies.

4.2.3. Drug Dissolution and Absorption

After validating the velocity fields, the dissolution, advection, and absorption of a solid drug particle was simulated in the airway surface liquid layer mesh using the customized solver, *dissolutionTransportFoam*, developed in OpenFOAM. The solubility of the drug, which controls the rate of dissolution, and the octanol/water partition coefficient (*kow*), which determines the rate of absorption at the epithelium, were specified at the start of each simulation. Table 13 lists the parameters that were tested for which the absorption of drug was studied.

Table 13. Parameters used in the drug absorption simulations

Parameter	Value
Octanol/water partition coefficient (<i>kow</i>)	5000, 2, 0.005
Solubility (mg/ml)	0.02, 0.2
Particle size (μm)	3, 5
Dosage (μg)	45

The values mentioned in Table 13 were in accordance with the currently marketed drugs. Specifically, Mometasone Furoate (MF) is a drug used to prevent and relieve symptoms of sneezing and runny nose, and it has a *kow* of 5000 and a solubility of 0.02 mg/ml. Flunisolide (FN)

is a corticosteroid used to treat seasonal allergy symptoms such as itchy and runny nose, and it has a *kow* of 2 and a solubility of 0.2 mg/ml. Ribavirin is an antiviral drug primarily used for targeting the blood-brain-barrier (74) and it has a *kow* of 0.005.

Various researchers have conducted experimental studies to determine the amount of drug that deposits in the nasal vestibule (NV) region and found that about 65-85% of the drug from a commercial and placebo nasal spray inhalers deposits in this region (75-77). Taking this into consideration, 80% of the drug particles were injected from uniformly distributed locations on the NV surface while the remaining 20% were injected from the ciliated posterior and the olfactory regions in this study.

Effect of partition coefficient

The effect of partition coefficient on the rate of drug uptake for particles of size 5 μm and solubility 0.02 mg/ml is shown in Figure 41.

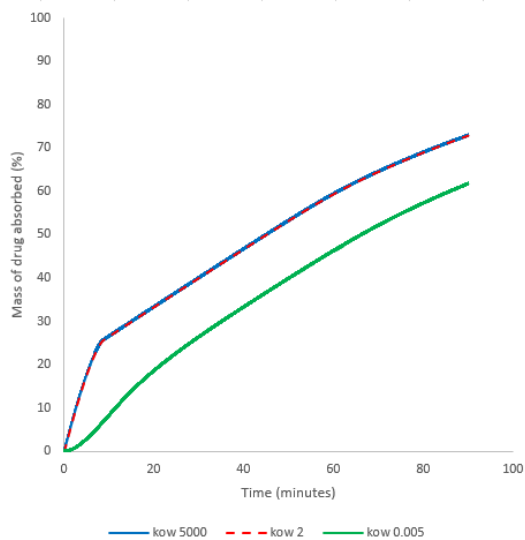


Figure 41. Effect of partition coefficient on the drug uptake

In general, a higher partition coefficient for the drug indicates a greater ability to be absorbed by the epithelium. Thus, the partition coefficients of 5000 and 2 exhibit a faster rate of drug uptake than 0.005. The drugs with partition coefficients 5000 and 2 show similar rates of absorption because the concentration gradient at the epithelium, as determined by the boundary condition described in Chapter 2, is high for both the partition values indicating near-sink conditions. The curves indicate a faster rate of uptake in the first 10 minutes than at other times. This is understood to be because of the distribution of injection positions of the particles at the top of the mucus layer. The lesser number of particles on the surface of the posterior region have a larger volume to freely dissolve and hence the dissolution and the uptake happens very quickly. After the dissolution of the particles injected in the posterior region, the rate of dissolution and absorption depends entirely on the particles injected in the nasal vestibule. However, the epithelium in the nasal vestibule region do not participate in drug absorption and the velocity of the airway surface liquid in this region is very low. Thus, the drug dissolves and is advected into posterior region at a lower velocity to be taken up which results in a slower rate of uptake after 10 minutes.

The evolution of the concentration of the drug at the epithelium is illustrated in Figure 42 for the different partition coefficients. The drug with partition coefficient 0.005 always displays a non-zero concentration at the epithelium, indicating the accumulation of the drug due to poor absorption capacity. The concentrations for the partition coefficients 2 and 5000 are almost zero indicating a high absorption capacity. The temporal evolution and the rates of uptake appear the same for the partition coefficients 2 and 5000. This is because, the concentration gradient at the epithelium, as determined by the boundary condition described in chapter 2, is high for both the partition values indicating near-sink conditions.

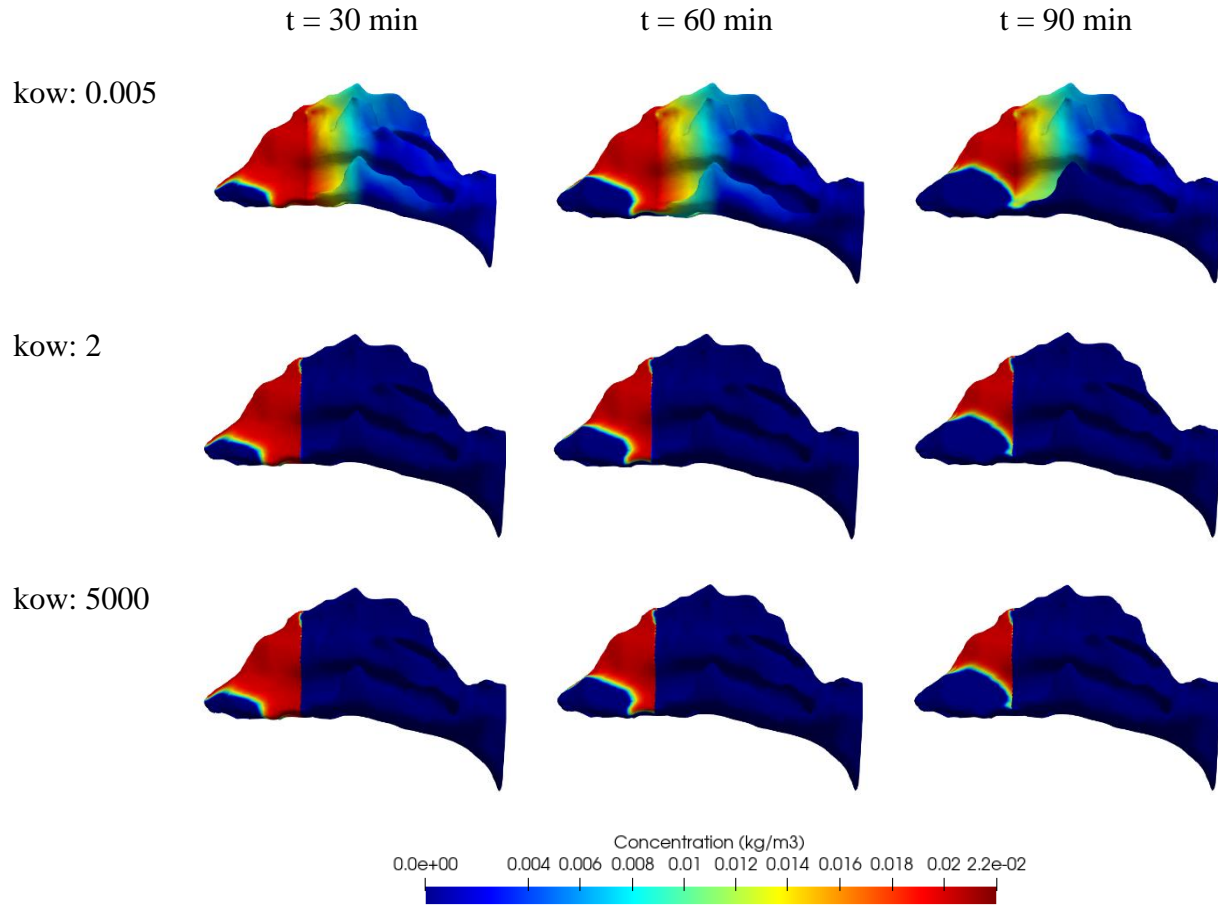


Figure 42. Temporal evolution of the drug on the epithelial surface

The concentration profiles in the different regions in the nasal cavity was analyzed using the slice shown in Figure 38. The contours appear very similar in the left and the right nasal cavities and hence only the left section is shown. The temporal evolution of the concentration in the various segments for the partition coefficients 0.005 and 2 are shown in Figures 43 and 44. The concentration of the drug for the partition coefficient of 0.005 can be seen decreasing with time as more drug dissolves and gets absorbed. In particular, the concentration in the olfactory region appears higher compared to the other segments because of mucus secretion. The face-normal component of the velocity repels the dissolved drug, thus, preventing it from reaching the

epithelium. For the partition values of 2 and 5000, the concentration of the drug in the various segments is close to zero.

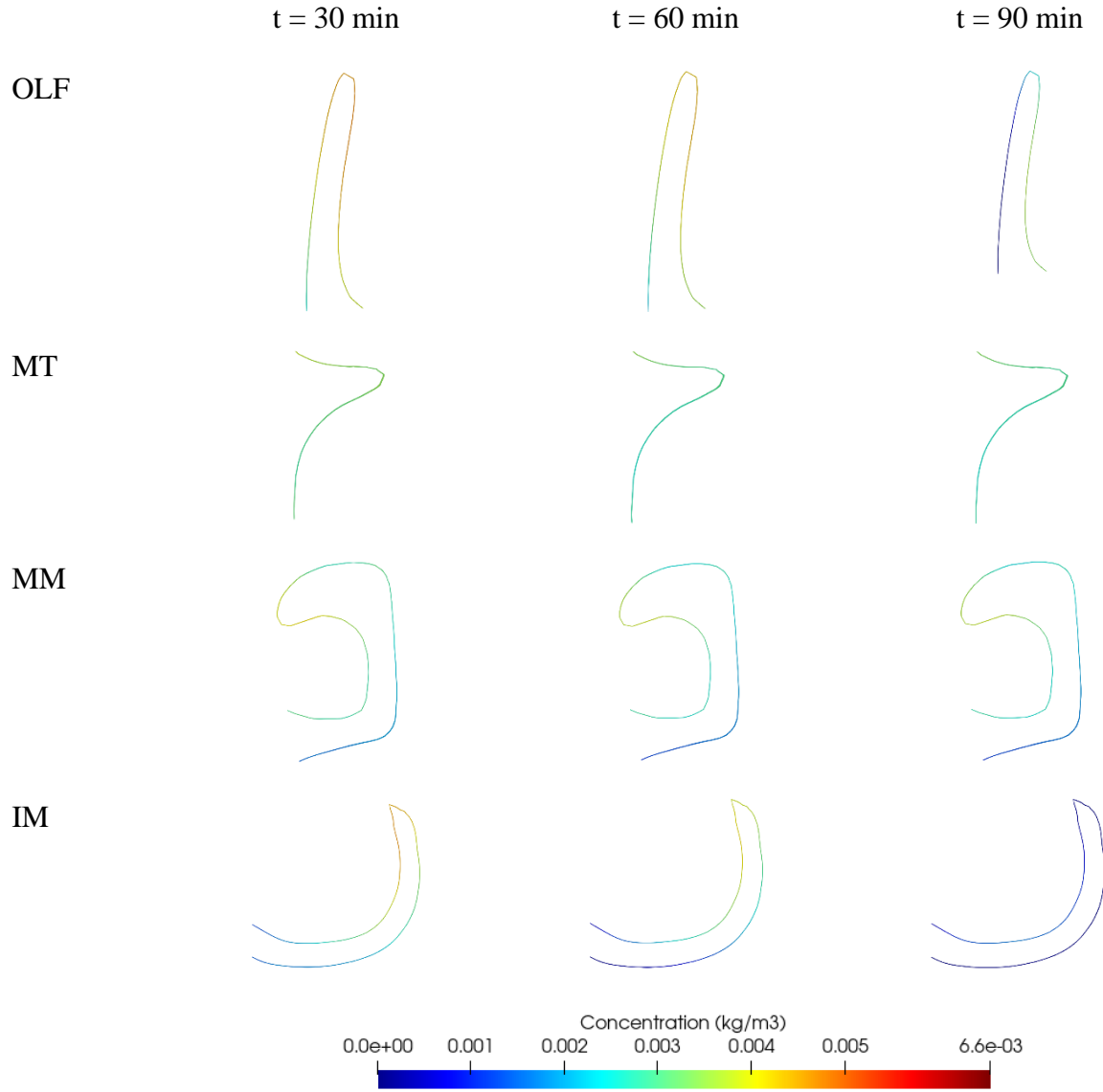


Figure 43. Concentration profiles in the segments on the chosen slice for $k_{ow} = 0.005$

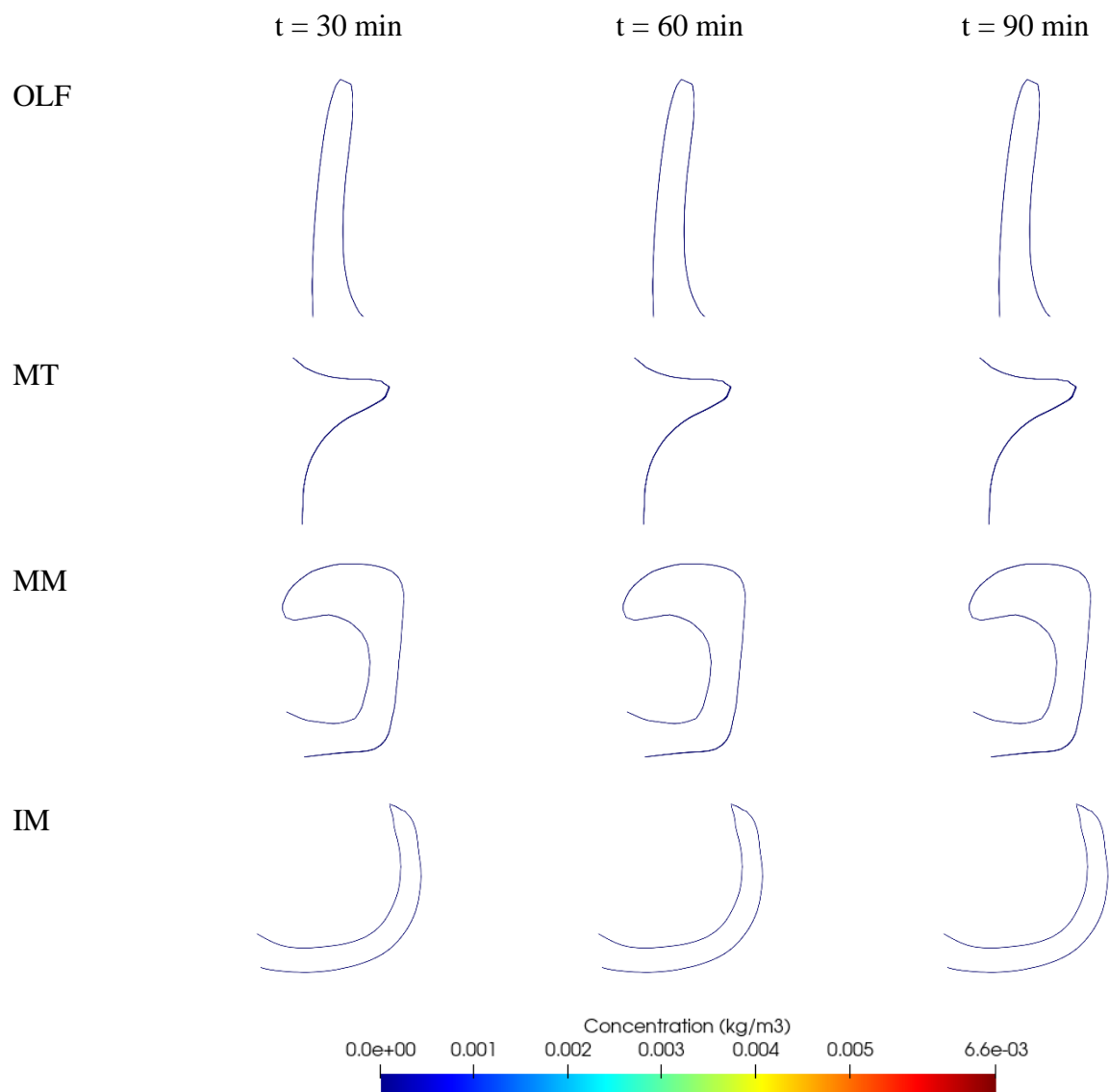


Figure 44. Concentration profiles in the segments on the chosen slice for $k_{ow} = 2$

To better understand the reason for the low concentrations for the partition coefficients 2 and 5000, the mass flux at the epithelium was studied. The instantaneous mass flux at the epithelium at the end 90 minutes is shown in Figure 45. The mass flux is very high, around $150 \mu\text{g}/\text{m}^2\text{s}$, close to the nasal valve for the partition coefficients of 2 and 5000. This shows that the drug hardly reaches the chosen slice (see Figure 38) as the high rate of mass transfer very close to the nasal valve

results in the absorption of the drug at the start of the posterior region. This indicates that the drug is taken up as soon as it gets advected into the posterior region from the anterior region. However, for the partition coefficient of 0.005, the mass flux is low and relatively uniform throughout the posterior region as shown in Figure 45b.

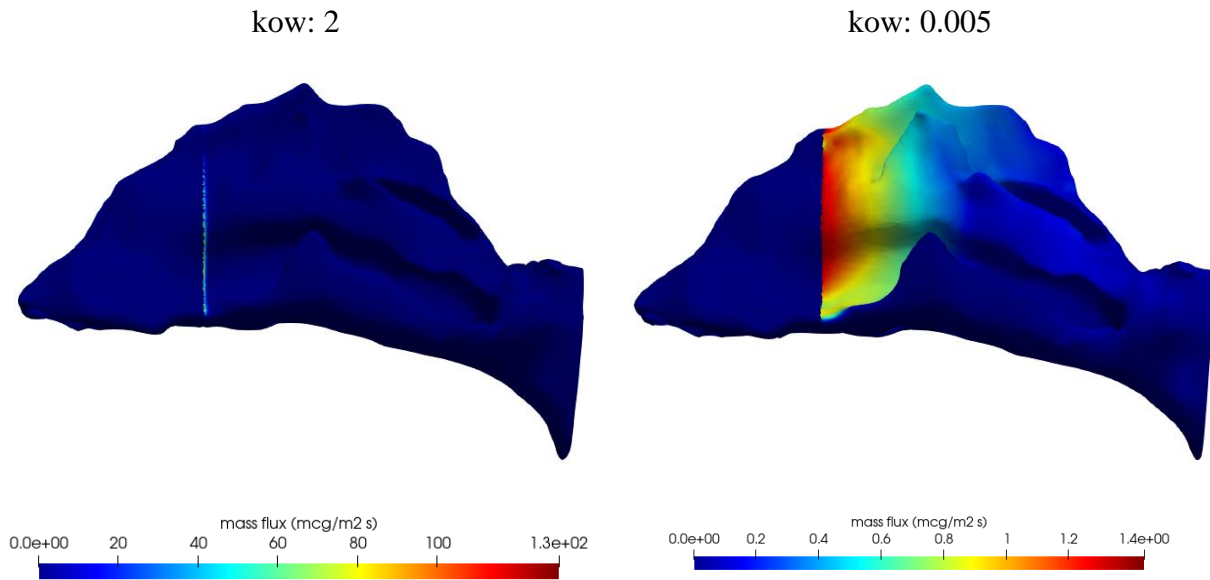


Figure 45. Mass flux at the epithelium for partition coefficients a) 2 b) 0.005

The concentration and the mass flux profiles presented are at time instants by which the 20% of the particles injected from the posterior surface gets completely absorbed. This is also the reason for the near-zero concentration for higher partition coefficients. In the first 10 minutes, the uptake is primarily due to the particles injected from the posterior surface. The temporal evolution of the concentration profiles for a section of the middle meatus at time instants less than 10 minutes are presented in Figure 46.

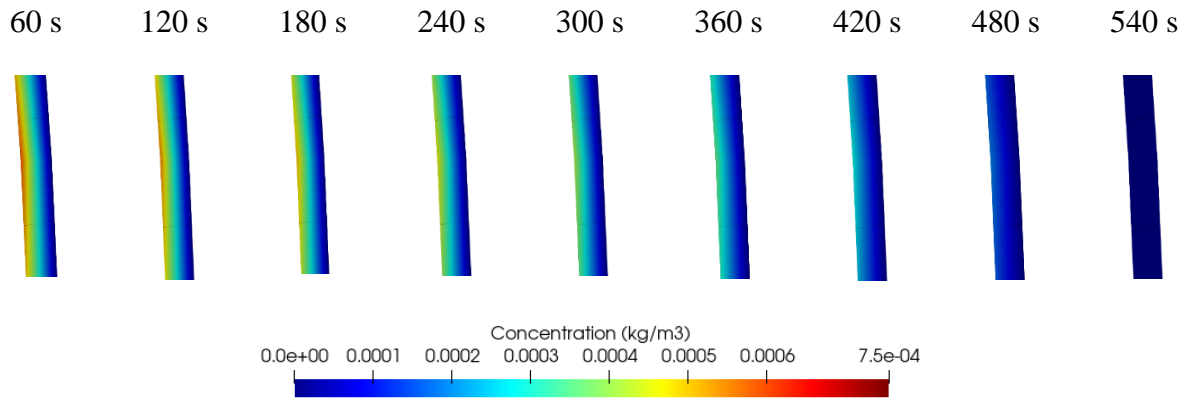


Figure 46. Evolution of concentration within the first 10 minutes for $k_{ow} = 2$

Effect of Solubility

The effect of solubility on the rate drug absorption is shown in Figure 47. The uptake profiles show that increasing the solubility has the capacity to increase the rate of mass absorption even for a hydrophilic drug with a low partition coefficient. The approach of artificially increasing the solubility has also been shown to be practically feasible by the addition of artificial surfactant to the dissolution medium by Franek et al. (48). The cumulative uptake reaches 100% for a partition coefficient of 2 while for 0.005, it hovers around 90%. One reason for this stagnation at 90% could be that the remaining 10% of the dissolved drug is advected out through the nasopharynx because of the velocity field before it could be absorbed.

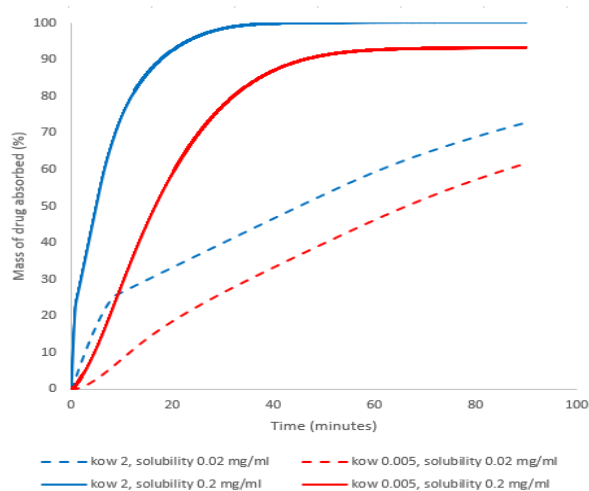


Figure 47. Effect of solubility on the drug uptake

Of particular interest is the drastic improvement in absorption characteristic of the hydrophilic drugs with an increase in solubility. Figure 48 shows a ten-fold increase in the mass flux after 15 minutes from the value when the solubility was 0.02 mg/ml, which is spread over a larger surface area. This could explain the reason the hydrophilic drug with a higher solubility exhibits a faster rate of uptake than a hydrophilic drug with lower solubility. The mass flux reduces to zero as time increase due to the absence of drug in the system.

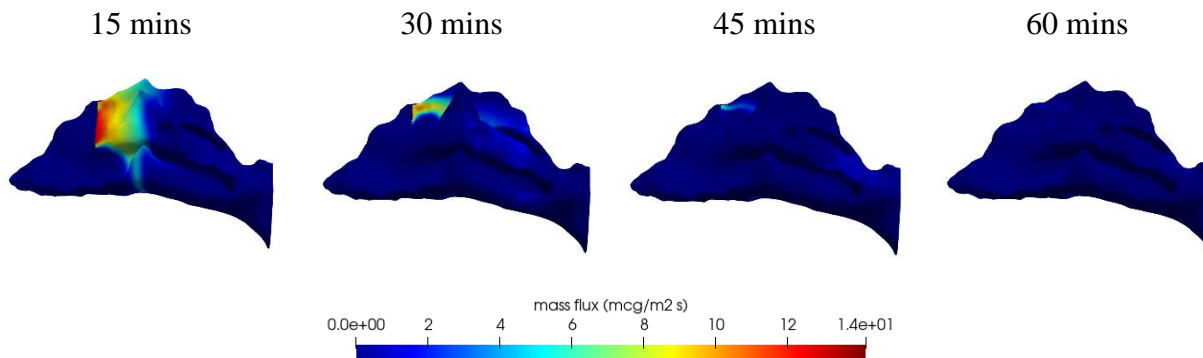


Figure 48. Mass flux for the partition coefficient of 0.005 and solubility 0.2 mg/ml

Effect of Particle Size

The effect of particle size on the rate of uptake is shown in Figure 49 by running the simulations with particles of diameter 3 μm . Considering the same total mass of the drug, the number of smaller particles and hence, their surface area will be high. A greater surface area will result in a faster rate of dissolution and hence, absorption. Thus, the rate of uptake is higher in the first 5 minutes for the smaller particles. Drug particles in the nanometer range can be expected to show a high rate of uptake. Commercial inhalers spray large particles which, as will be shown later, do not influence the absorption favorably. This reiterates the requirement of smaller particles for both deposition and dissolution in the mucus layers.

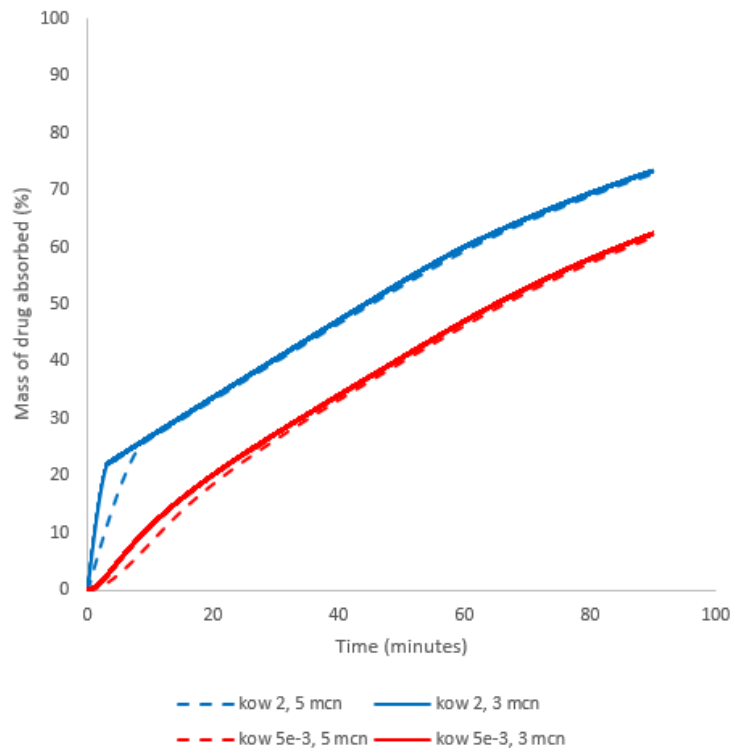


Figure 49. Effect of particle size on the rate of uptake

4.2.4. A Basic Nasal-Spray Application Study

So far, a relative order of magnitude analysis (ROMA) was conducted to elucidate the effects of partition coefficient, solubility, and particle size on the rate of drug absorption. Now as a special test application, results of a more realistic case of deposition and absorption of a drug from a commercially available nasal spray inhaler is presented. Rather than assuming a uniform distribution of injection positions with 80% of the monodisperse particles on the anterior surface, actual deposition sites of polydisperse particles with realistic inhaler parameters were used to analyze the deposition and the uptake of the drug particles.

Nasal spray pumps are inhaler devices which spray aerosol into the nasal cavity for both topical and systemic treatment. These devices do not contain any propellant and instead rely on aerodynamic atomization to yield smaller droplets. Typically, the drug is formulated as a solution or a suspension in water. Various nasal spray devices are currently available in the market for the treatment of allergies such as stuffy nose and itching. In this study, the deposition of drug aerosol and the subsequent absorption by the epithelium of Flonase nasal spray were analyzed. Flonase contains Fluticasone Propionate (FP) as the active pharmaceutical ingredient which is a corticosteroid used in the treatment of itching and sneezing by preventing access to foreign particles such as pollen or dust and reducing swelling.

Spray Parameters

Dayal et al. (78) obtained the diameter distribution of droplets sprayed from Flonase at 15 mm from the nozzle in terms of the cumulative volume percentage as shown in Figure 50. The experimental cumulative volume percentage was converted into probability density values for a

discrete set of diameters in the range specified in the experiment. The *general* size distribution was selected in OpenFOAM and the probability density values were specified. The typical range of diameters observed for Flonase nasal spray is 10 μm – 300 μm .

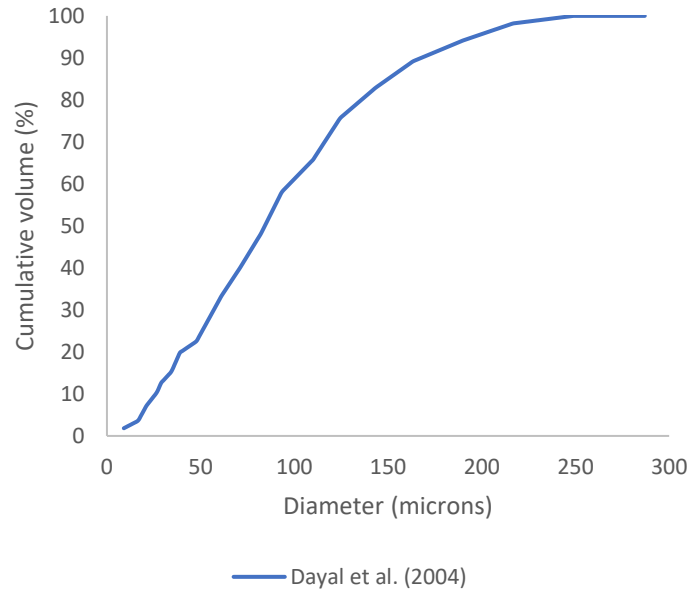


Figure 50. Diameter distribution of droplets from Flonase at 15 mm from nozzle

Flonase contains 50 μg of solid drug suspended in 100 ml of water and generally, 2 doses are administered. This gives a total shot weight of 100 μg and considering the probability densities obtained for the set of diameters, the total aerosol count can be computed as 4 million. The mass fraction of the drug in the suspension is 0.0005 and it was assumed that each of the injected aerosol contains the same fraction of the drug.

In a different experimental study of the deposition of nasal spray drug in a cast of the nasal cavity, Hosseini et al. (79) reported the velocity of the droplets at 30 mm from the nozzle along the centerline to be 10.93 m/s for Flonase. Thus, the injection velocity of the aerosol was fixed as 10

m/s in the simulations. The authors reported the spray angle for Flonase to be 20° which was used in the simulations. The authors also note that an angle of 65° in the sagittal plane and about 5° in the coronal plane directed into the nasal cavity were orientations generally found suitable for spraying. Inthavong et al. (80) notes that 0.28 mm was a common choice for the orifice diameter and hence, the same value was used to describe the diameter of the plane from which the particles were injected.

All the parameters reported in the experimental studies were at a certain distance downstream from the nozzle. The approach of fixing these parameters as injection conditions at the origin of the spray was deemed suitable and valid because of the very low evaporation rates of a water droplet. For this reason, the aerosol spray was assumed to comprise of solid Lagrangian particles rather than droplets. The one-way coupled approach was used, and its validity was established beforehand as described in section 3.4. The droplet breakup model was not specified as the diameters used in the simulation were the result of completed spray atomization and further breakup of the droplets was not observed in test runs when the model was turned on.

Deposition

The airflow was simulated with a flowrate of 20 LPM from the nostrils. The particles were then injected into the converged flow field with the injection parameters described. The two cases considered were angles of 65° and 45° in the sagittal plane. The deposition patterns for both cases are shown in Figure 51. The deposition percentages are reported in Table 14.

diameter greater than 100 μm deposit on the anterior surface. Larger particles can be assumed to contain a higher mass of the drug. Thus, considering the mass fraction of the drug as 0.0005 and the total mass of the particles injected, the mass deposition percentage for the drug can be computed as 98.5% for the anterior region. This indicates that 98.5% of the drug gets deposited in the anterior non-ciliated region while only 1% of the drug gets deposited in the posterior region where the absorption takes place. Also, the deposition in the posterior region happens closer to the olfactory where the uptake is slow.

The deposition pattern for the case with 45° angle, the deposition pattern indicates that the particles are farther away from the olfactory region compared with the case of 65° angle. The mass deposition percentage is also significantly higher in the posterior region with over 25% of the drug depositing in this region. These results are highly dependent on the geometry used. The *in vivo* studies of Leach et al. (81) take into account the variabilities in the geometries of the nasal cavities and the orientation of the inhaler which is comfortable for the volunteers. The ex-actuator results indicate around 95% deposition in the anterior region which agrees well with the simulation results. Also, the value of 85% for deposition in the anterior region reported in the literature (68) falls between the values reported here for the 2 cases.

Dissolution and Absorption

After obtaining the diameters and locations of the deposited particles, the drug absorption simulations were run in the airway surface liquid layer mesh. Fluticasone Propionate (FP) has a partition coefficient of 5000 and an aqueous solubility of 0.00014 mg/ml (46). However, the mucus lining also contains certain surfactants which have the potential to increase the solubility of a drug.

As Franek et al. (48) showed, using an artificial surfactant yielded a solubility of 0.024 mg/ml for the drug and the same was used in the simulations to account for realistic conditions. The mass fraction of the drug was used to calculate the diameter of drug particles from the deposited particles and the particles were injected from their actual deposition sites. The cumulative uptake profiles of FP for the cases with 65° and 45° angles in the sagittal plane are shown in Figure 52.

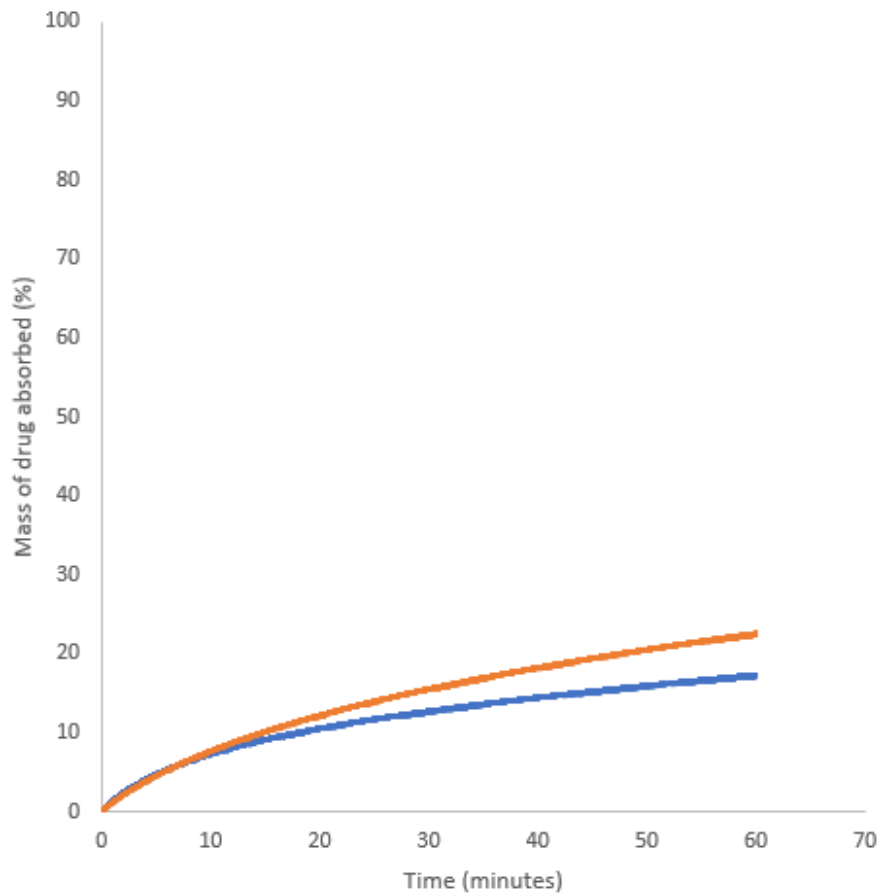


Figure 52. Fluticasone Propionate uptake using realistic deposition sites and diameters

The deposition pattern indicated lower anterior deposition for the case of 45° nozzle angle and hence, a higher rate of uptake is justified. However, a reduction of around 25% in the anterior deposition does not lead to a drastic increase in the absorption profile. This could be because

majority of the particles still deposit within a smaller area on the nasal cavity surface. This will increase the local bulk concentration of the dissolved drug quickly which will slow down the rate of dissolution and hence, absorption. The results indicate that efforts concerning the optimization of the nasal spray device should be directed towards spreading the deposition over a larger surface area and reducing the anterior deposition.

CHAPTER 5: CONCLUSIONS AND FUTURE WORK

Spray inhalers are popular devices for treating respiratory as well as systemic ailments. The drugs, typically embedded in aqueous carrier droplets, are sprayed from a nozzle at a high velocity into the oral or the nasal cavity. Specifically, pMDIs and DPIs deliver drug-aerosols to lung sites with solid tumors, severe inflammation, or pathways to systemic regions. In contrast, nasal pumps and nebulizers are mainly used for treatment of the nasopharynx. The airways, especially the nasal cavities, are lined with the airway surface liquid (ASL) that contains the gel-like mucus layer and the watery periciliary sol layer. After deposition, the drug particles dissolve in the ASL and diffuse towards the epithelial cells which line the airway walls. The moving mucus layer, due to the beating of the cilia, can also advect the dissolved drug. All of these processes are difficult to analyze using experimental tools due to the lack of resolution and high cost involved. Numerical tools, such as computational fluid-particle dynamics (CF-PD) techniques may help to better understand these processes by providing both spatial and temporal variations of parameters, including particle deposition, temperature, and drug concentration. Employing realistic injection parameters from spray inhalers, eg, a commercial pMDI as well as a nasal pump, the thermal evolution of droplet sprays was modeled, simulated, and results analyzed. Applications include administration of oral and nasal sprays. Furthermore, a complete characterization of the transport, deposition, dissolution, and absorption of the drug into the nasal epithelium was achieved.

Specifically, the spray characteristics of Ventolin, a pressurized metered dose inhaler, were simulated. The results highlighted the parabola-like radial profiles for the velocity and the temperature of the droplets while also indicating the recirculatory flow in the mouthpiece. With the validated velocity, temperature and diameter of the spray aerosol, the deposition inside a geometry of the oral cavity was considered which matched very well with the experimental results

for representative cases. The effect of flowrate was then analyzed by assuming steady inhalation. The segmental deposition results indicated high drug accumulation in the oropharynx and in the front of the oral cavity for lower flowrates due to strong recirculatory flows. The segmental droplet temperature results showed higher temperatures for higher flowrates because of enhanced convective flow around the evaporating droplets. The general problem of high oropharyngeal deposition and cold impacting droplets was tackled by devising a new ‘pulsed injection’ strategy in which the spray is broken into pulses with a time delay between them. This approach was analyzed using computational tools and the results indicated a maximum of 20% increase in the lung deposition over conventional drug administration. The temperatures were also higher by a maximum of 20 °C. The boiling and evaporation model was also validated for microdroplets containing water and propellants, thus lending credibility to the simulation results. The study of the spray characteristics of a pMDI has laid the foundation for studying and optimizing any oral or nasal spray inhaler in a similar fashion. The high momentum of the spray needs to be reduced to increase greater penetration of the drug into the lungs. The promise shown through the computational analysis of the ‘pulsed injection’ technique warrants experimental and inhaler design studies to fabricate micro actuators to generate a pulsed spray. The combination of the existing devices such as spacers and the pulsed injection method can also be explored to reduce the velocity of the spray even further which would decrease both device and oropharyngeal deposition. Such techniques also have the capability to reduce the ‘cold-freon’ effect which is associated with low temperature impacting droplets as shown in this research. These measures not only lead to a greater deposition in the lungs but also improve the patient’s comfort while use the inhalers which will only increase their confidence when using these devices.

Focusing on representative nasal cavities, spray-inhaled drug deposition, dissolution and ultimately absorption into the epithelium have been simulated and analyzed. A customized solver and a boundary condition were developed in OpenFOAM (using C++) to simulate the dissolution of a solid particle and absorption, respectively. First, the results obtained using the customized dissolution-transport solver and the boundary condition were validated with recent experimental data. With the validated solver, a parametric analysis of the effects of the drug partition coefficient, solubility and the particle size was conducted in a mesh of the nasal airway surface liquid layers. Wall driven velocity was used to mimic cilia motion while the mucus secretion was simulated using a normal component of velocity. Using one-way coupled Lagrangian particle tracking, the particle dissolution and absorption were analyzed in the validated mucus layer velocity field. The results indicated a higher rate of drug uptake for highly lipophilic drugs. For the drugs with a higher partition coefficient, the absorptive mass flux was very high near the nasal valve while it was more uniform over the epithelial area for drugs with a lower partition coefficient. Increasing the solubility made more drug available for absorption and hence, even for a hydrophilic drug, the rate of uptake improved significantly. Also, a smaller particle size provides a higher total surface area for dissolution and hence, the rate of uptake increased. In general, the segmental concentration profiles indicate an accumulation of the drug concentration in the olfactory region compared to the other segments because of face-normal velocity used to simulate mucus secretion. As a precursor to more detailed studies that will follow, the application of a nasal spray inhaler was also discussed, covering the deposition, dissolution, and absorption of Fluticasone Propionate (FP). The deposition results indicated a good agreement with *in vivo* data and a decrease in the angle of the inhaler in the sagittal plane reported a significant increase in the drug depositing in the posterior region. However, the absorption of the drug in the epithelium indicated only a 5% improvement

for the reduced angle case. This is thought to be because of the congregated deposition locations for the particles which reduce the rate of dissolution. Nevertheless, incorporating actual deposition locations for computing uptake has shown that the profiles can be very different from what is obtained by assuming a uniform deposition. The simple yet insightful case study of a nasal spray inhaler, combined with the parametric analysis conducted before indicate that there is a need to decrease the anterior deposition and make the particles cover a larger surface area of the nasal cavity. A complete study such as this would help in providing deeper insight into the physics of the process and minimize the dependence on time consuming experimental procedures.

As the platform has been set by this study, there are numerous possibilities to extend the work further. Concerning spray inhalers, one such avenue to explore is the computational analysis of the spacer and pulsed injection combination. This approach could indeed negate the downside of using a spacer, which is the high device deposition. The spacer could provide the additional benefit of longer residence times for the droplets which would enhance evaporation rates. The oral cavity deposition can also be extended to analyze the dissolution and absorption in the oral mucus layer in a similar fashion as the nasal mucus layer study conducted here.

Another important area of research is the prediction of the spray parameters from first principles. Very few articles (24, 25, 29) discuss this owing to the complex physics involved in the production a spray in a pMDI. Such a study could reduce the dependence on experimental studies which can, at best, provide values of parameters at discrete locations. This research problem will involve studying the physics of flash evaporation in a multi-component system and aerodynamic breakup of droplets. The former necessitates the use of very small time steps as the rate of evaporation of a propellant is very high. The processes inside the metering chamber or the tank will have to be simulated and the resulting droplet parameters need to be used as injection conditions for the pMDI

or the nasal spray. This would truly serve as an end-to-end model which will be capable of simulating all the processes associated with spray inhalers.

In the present study, the absorption boundary condition was developed by assuming a zero concentration in the epithelium. In reality, the epithelium has some thickness and hence some concentration gradient. The epithelium is separated from the blood stream by a connective tissue which needs to be treated as a porous medium. Thus, a part of the current research efforts is targeted at developing such a realistic model to predict the uptake. A new solver to simulate the absorption at the epithelium in the internal cells rather than the boundary has been developed as part of this research study.

REFERENCES

1. Livraghi A, Randell SH. Cystic Fibrosis and Other Respiratory Diseases of Impaired Mucus Clearance. *Toxicologic Pathology*. 2016;35(1):116-29.
2. Labiris NR, Dolovich MB. Pulmonary drug delivery. Part I: Physiological factors affecting therapeutic effectiveness of aerosolized medications. *British Journal of Clinical Pharmacology*. 2003 Dec;56(6):588-99.
3. Newman SP. Delivering drugs to the lungs: The history of repurposing in the treatment of respiratory diseases. *Advanced Drug Delivery Reviews*. 2018;133:5-18.
4. Newman SP. Principles of metered-dose inhaler design. *Respiratory Care*. 2005 Sep;50(9):1177.
5. Djupesland PG. Nasal drug delivery devices: characteristics and performance in a clinical perspective—a review. *Drug Deliv and Transl Res*. 2012;3(1):42-62.
6. El-Sherbiny IM, Yacoub MH, El-Baz NM. Inhaled nano- and microparticles for drug delivery. *Global Cardiology Science and Practice*. 2015 Jan 29;2015(2015):2.
7. Shi H, Kleinstreuer C. Simulation and Analysis of High-Speed Droplet Spray Dynamics. *J Fluids Eng*. 2007 /05/01;129(5):621-33.
8. Kleinstreuer C, Shi H, Zhang Z. Computational Analyses of a Pressurized Metered Dose Inhaler and a New Drug-Aerosol Targeting Methodology. *Journal of Aerosol Medicine*. 2007;20(3):294-309.

9. Kleinstreuer C, Feng Y, Childress E. Drug-targeting methodologies with applications: A review. *World Journal of Clinical Cases: WJCC*. 2014 16 December;2(12):742.
10. Kublik H, Vidgren MT. Nasal delivery systems and their effect on deposition and absorption. *Advanced Drug Delivery Reviews*. 1998;29(1-2):157-77.
11. Costantino HR, Illum L, Brandt G, Johnson PH, Quay SC. Intranasal delivery: Physicochemical and therapeutic aspects. *International Journal of Pharmaceutics*. 2007;337(1-2):1-24.
12. Longest PW, Bass K, Dutta R, Rani V, Thomas ML, El-Achwah A, et al. Use of computational fluid dynamics deposition modeling in respiratory drug delivery. *Expert Opinion on Drug Delivery*. 2019 Jan 2;16(1):7-26.
13. Stein SW, Thiel CG. The History of Therapeutic Aerosols: A Chronological Review. *Journal of Aerosol Medicine and Pulmonary Drug Delivery*. 2017;30(1):20-41.
14. Gabrio BJ, Stein SW, Velasquez DJ. A new method to evaluate plume characteristics of hydrofluoroalkane and chlorofluorocarbon metered dose inhalers. *International Journal of Pharmaceutics*. 1999;186(1):3-12.
15. Liu X, Doub WH, Guo C. Evaluation of metered dose inhaler spray velocities using Phase Doppler Anemometry (PDA). *International Journal of Pharmaceutics*. 2012 Feb 28;423(2):235-9.
16. DUNBAR CA. ATOMIZATION MECHANISMS OF THE PRESSURIZED METERED DOSE INHALER. *Particulate Science and Technology*. 1997 Jul 1;15(3-4):253-71.

17. Myrdal P, Sheth P, Stein S. Advances in Metered Dose Inhaler Technology: Formulation Development. *AAPS PharmSciTech*. 2014 Apr;15(2):434-55.
18. BARRY PW, O'CALLAGHAN C. Video Analysis of the Aerosol Cloud Produced by Metered-dose Inhalers. *Pharmacy and Pharmacology Communications*. 1995 Mar;1(3):119-21.
19. Crosland BM, Johnson MR, Matida EA. Characterization of the Spray Velocities from a Pressurized Metered-Dose Inhaler. *Journal of Aerosol Medicine and Pulmonary Drug Delivery*. 2009 Jun;22(2):85-98.
20. Smyth H, Hickey AJ, Brace G, Barbour T, Gallion J, Grove J. Spray Pattern Analysis for Metered Dose Inhalers I: Orifice Size, Particle Size, and Droplet Motion Correlations. *Drug Development and Industrial Pharmacy*. 2006;32(9):1033-41.
21. Alatrash A, Matida E. Characterization of Medication Velocity and Size Distribution from Pressurized Metered-Dose Inhalers by Phase Doppler Anemometry. *Journal of Aerosol Medicine and Pulmonary Drug Delivery*. 2016 Dec 1;29(6):51-513.
22. Wigley G, Versteeg HK, Hodson D. Near-orifice PDA measurements and atomization mechanism of a pharmaceutical pressurized metered dose inhaler. *ILASS-Europe*; 9-11 September 2002; Zaragoza.
23. Clark AR. Metered atomization for respiratory drug delivery [dissertation]. Loughborough University of Technology, Loughborough, UK; 1991.

24. Gavtash B, Versteeg HK, Hargrave G, Myatt B, Lewis D, Church T, et al. Transient flashing propellant flow models to predict internal flow characteristics, spray velocity, and aerosol droplet size of a pMDI. *Aerosol Science and Technology*. 2017 Jan 13,;51(5):564-75.
25. Gavtash B, Versteeg HK, Hargrave G, Myatt B, Lewis D, Church T, et al. Transient aerodynamic atomization model to predict aerosol droplet size of pressurized metered dose inhalers (pMDI). *Aerosol Science and Technology*. 2017 May 5,;51(8):998-1008.
26. Martin AR, Kwok DY, Finlay WH. Investigating the Evaporation of Metered-Dose Inhaler Formulations in Humid Air: Single Droplet Experiments. *Journal of Aerosol Medicine*. 2005 Jun 1,;18(2):218-24.
27. Sheth P, Grimes MR, Stein SW, Myrdal PB. Impact of droplet evaporation rate on resulting in vitro performance parameters of pressurized metered dose inhalers. *International Journal of Pharmaceutics*. 2017 Aug 7,;528(1-2):360-71.
28. Brambilla G, Church T, Lewis D, Meakin B. Plume temperature emitted from metered dose inhalers. *International Journal of Pharmaceutics*. 2011;405(1):9-15.
29. Gavtash B, Versteeg HK, Hargrave G, Myatt B, Lewis D, Church T, et al. Multi-physics theoretical approach to predict pMDI spray characteristics. *Drug Delivery to the Lungs 27*, 7th-9th December, 2016; Edinburgh; 2016.
30. Chen Y, Chen Y, Young P, Young P, Murphy S, Murphy S, et al. High-Speed Laser Image Analysis of Plume Angles for Pressurised Metered Dose Inhalers: The Effect of Nozzle Geometry. *AAPS PharmSciTech*. 2017 Apr;18(3):782-9.

31. Moraga-Espinoza D, Eshaghian E, Shaver A, Smyth H. Effect of Inhalation Flow Rate on Mass-Based Plume Geometry of Commercially Available Suspension pMDIs. *AAPS J.* 2018 Sep;20(5):1-12.
32. Newman SP, Clark AR, Talae N, Clarke SW. Pressurised aerosol deposition in the human lung with and without an "open" spacer device. *Thorax.* 1989 Sep;44(9):706-10.
33. Swift DL. Apparatus and method for measuring regional distribution of therapeutic aerosols and comparing delivery systems. *Journal of Aerosol Science.* 1992; 23:495-8.
34. Cheng YS, Fu CS, Yazzie D, Zhou Y. Respiratory Deposition Patterns of Salbutamol pMDI with CFC and HFA-134a Formulations in a Human Airway Replica. *Journal of Aerosol Medicine.* 2001 Jun 1;14(2):255-66.
35. Zhang Y, Gilbertson K, Finlay WH. In Vivo-In Vitro Comparison of Deposition in Three Mouth-Throat Models with Qvar® and Turbuhaler® Inhalers. *Journal of Aerosol Medicine.* 2007;20(3):227-35.
36. Biswas R, Hanania NA, Sabharwal A. Factors Determining In Vitro Lung Deposition of Albuterol Aerosol Delivered by Ventolin Metered-Dose Inhaler. *Journal of Aerosol Medicine and Pulmonary Drug Delivery.* 2017 Aug 1;30(4):256-66.
37. McCabe JC, Koppenhagen F, Blair J, Zeng X. ProAir® HFA Delivers Warmer, Lower-Impact, Longer-Duration Plumes Containing Higher Fine Particle Dose Than Ventolin® HFA. *Journal of Aerosol Medicine and Pulmonary Drug Delivery.* 2012 Apr 1;25(2):14-109.

38. Gupta A, Stein SW, Myrdal PB. Balancing Ethanol Cosolvent Concentration with Product Performance in 134a-Based Pressurized Metered Dose Inhalers. *Journal of Aerosol Medicine*. 2003 Jun 1,;16(2):167-74.
39. Yousefi M, Inthavong K, Tu J. Effect of Pressurized Metered Dose Inhaler Spray Characteristics and Particle Size Distribution on Drug Delivery Efficiency. *Journal of Aerosol Medicine and Pulmonary Drug Delivery*. 2017 Oct 1,;30(5):359-72.
40. Delvadia RR, Longest PW, Hindle M, Byron PR. In Vitro Tests for Aerosol Deposition. III: Effect of Inhaler Insertion Angle on Aerosol Deposition. *Journal of Aerosol Medicine and Pulmonary Drug Delivery*. 2013 Jun 1,;26(3):145-56.
41. Widdicombe JH. Regulation of the depth and composition of airway surface liquid. *Journal of Anatomy*. 2002 Oct;201(4):313-8.
42. Beule AG. Physiology and pathophysiology of respiratory mucosa of the nose and the paranasal sinuses. *GMS Current Topics in Otorhinolaryngology - Head and Neck Surgery*; 9: Doc07; ISSN 1865-1011. 2010; 9: Doc07.
43. Pires A, Fortuna A, Alves G, Falcão A. Intranasal Drug Delivery: How, Why and What for? *Journal of Pharmacy & Pharmaceutical Sciences*. 2009 Oct 12,;12(3):288-311.
44. Moran DT, Rowley JC, Jafek BW, Lovell MA. The fine structure of the olfactory mucosa in man. *Journal of Neurocytology*. 1982 Oct;11(5):721-46.

45. Sadler RC, Prime D, Burnell PK, Martin GP, Forbes B. Integrated in vitro experimental modelling of inhaled drug delivery: deposition, dissolution and absorption. *Journal of Drug Delivery Science and Technology*. 2011;21(4):331-8.
46. Arora D, Shah K, Halquist M, Sakagami M. In Vitro Aqueous Fluid-Capacity-Limited Dissolution Testing of Respirable Aerosol Drug Particles Generated from Inhaler Products. *Pharm Res*. 2010 May;27(5):786-95.
47. Rohrschneider M, Bhagwat S, Krampe R, Michler V, Breitzkreutz J, Hochhaus G. Evaluation of the Transwell System for Characterization of Dissolution Behavior of Inhalation Drugs: Effects of Membrane and Surfactant. *Molecular Pharmaceutics*. 2015;12(8):2618-24.
48. Franek F, Fransson R, Thörn H, Bäckman P, Andersson PU, Tehler U. Ranking in Vitro Dissolution of Inhaled Micronized Drug Powders including a Candidate Drug with Two Different Particle Sizes. *Molecular Pharmaceutics*. 2018 Nov 5;15(11):5319-26.
49. Cumming H, Rücker C. Octanol–Water Partition Coefficient Measurement by a Simple ¹H NMR Method. *ACS Omega*. 2017 Sep 30;2(9):6244-9.
50. Bur M, Huwer H, Muys L, Lehr C. Drug Transport Across Pulmonary Epithelial Cell Monolayers: Effects of Particle Size, Apical Liquid Volume, and Deposition Technique. *Journal of Aerosol Medicine and Pulmonary Drug Delivery*. 2010 Jun;23(3):119-27.
51. Haghi M, Traini D, Bebawy M, Young PM. Deposition, Diffusion and Transport Mechanism of Dry Powder Microparticulate Salbutamol, at the Respiratory Epithelia. *Molecular Pharmaceutics*. 2012 Jun 4;9(6):1717-26.

52. Rygg A, Longest PW. Absorption and Clearance of Pharmaceutical Aerosols in the Human Nose: Development of a CFD Model. *Journal of Aerosol Medicine and Pulmonary Drug Delivery*. 2016 Oct;29(5):416-31.
53. Rygg A, Hindle M, Longest PW. Absorption and Clearance of Pharmaceutical Aerosols in the Human Nose: Effects of Nasal Spray Suspension Particle Size and Properties. *Pharm Res*. 2015 Dec 21;33(4):909-21.
54. Zhang Z, Kleinstreuer C. Laminar-to-turbulent fluid-nanoparticle dynamics simulations: Model comparisons and nanoparticle-deposition applications. *International Journal for Numerical Methods in Biomedical Engineering*. 2011 Dec;27(12):1930-50.
55. Zhang Z, Kleinstreuer C. Low-Reynolds-Number Turbulent Flows in Locally Constricted Conduits: A Comparison Study. *AIAA Journal*. 2003 May 1;41(5):831-40.
56. Zhang Z, Kleinstreuer C. Computational analysis of airflow and nanoparticle deposition in a combined nasal–oral–tracheobronchial airway model. *Journal of Aerosol Science*. 2011 /03/01;42(3):174-94.
57. Kleinstreuer C. *Modern Fluid Dynamics*. 2nd ed. CRC Press; 2018.
58. Gosman AD, Ioannides E. Aspects of Computer Simulation of Liquid-Fueled Combustors. *Journal of Energy*. 1983 November 1;7(6):482-90.
59. Baifang Zuo, A. M. Gomes, C. J. Rutland Engine Research Center, University of Wisconsin – Madison. Studies of Superheated Fuel Spray Structures and Vaporization in GDI engines. 11th International Multidimensional Engine Modeling User's Group Meeting; 2000; ; 2000.

60. Spalding DB. *The Combustion of Liquid Fuels*. 1953; The Combustion Institute; 1953.
61. Zientara M, Jakubczyk D, Derkachov G, Kolwas K, Kolwas M. Simultaneous determination of mass and thermal accommodation coefficients from temporal evolution of an evaporating water microdroplet. *Journal of Physics D: Applied Physics*. 2005 Jun 21,;38(12):1978-83.
62. Calmet H, Inthavong K, Eguzkitza B, Lehmkuhl O, Houzeaux G, Vázquez M. Nasal sprayed particle deposition in a human nasal cavity under different inhalation conditions. *PloS one*. 2019 Sep 6,;14(9): e0221330.
63. Inthavong K, Ge Q, Se CMK, Yang W, Tu JY. Simulation of sprayed particle deposition in a human nasal cavity including a nasal spray device. *Journal of Aerosol Science*. 2011 Feb;42(2):100-13.
64. Kimbell JS, Segal RA, Asgharian B, Wong BA, Schroeter JD, Southall JP, et al. Characterization of Deposition from Nasal Spray Devices Using A Computational Fluid Dynamics Model of The Human Nasal Passages. *Journal of Aerosol Medicine*. 2007 Mar;20(1):59-74.
65. Southall JP, Newell HE, Dickens CJ, Al-Suleimani Y, Abduljalil H, Yule AJ. Characterization of particle deposition and penetration from current nasal spray devices. Part I—Laboratory characterisation of nasal spray pumps. *Journal of Aerosol Medicine*. 2003.
66. Finlay WH. *The Mechanics of Inhaled Pharmaceutical Aerosols: An Introduction*. Academic Press; 2001.

67. Dunbar Ca, Watkins Ap, Miller Jf. An Experimental Investigation of the Spray Issued from a pMDI Using Laser Diagnostic Techniques. *Journal of Aerosol Medicine*. 1997 January 1,;10(4):351-68.
68. Dunbar CA, Miller JF. THEORETICAL INVESTIGATION OF THE SPRAY FROM A PRESSURIZED METERED-DOSE INHALER. *AAS*. 1997;7(4).
69. Ditcham W, Murdzoska J, Zhang G, Roller C, von Hollen D, Nikander K, et al. Lung Deposition of ^{99m}Tc-Radiolabeled Albuterol Delivered through a Pressurized Metered Dose Inhaler and Spacer with Facemask or Mouthpiece in Children with Asthma. *Journal of Aerosol Medicine and Pulmonary Drug Delivery*. 2014 July 23,;27(S1): S-63.
70. Arora P, Sharma S, Garg S. Permeability issues in nasal drug delivery. *Drug Discovery Today*. 2002 Sep;7(18):967-75.
71. Gizurason S. The Effect of Cilia and the Mucociliary Clearance on Successful Drug Delivery. *Biological & Pharmaceutical Bulletin*. 2015;38(4):497-506.
72. Ar H, S D, Jm B, Pa C. Density of epithelial cells in the normal human nose and the paranasal sinus mucosa. A scanning electron microscopic study. *Rhinology*. 1990 /03/01;28(1):25-32.
73. Shah SA, Berger RL, McDermott J, Gupta P, Monteith D, Connor A, et al. Regional deposition of mometasone furoate nasal spray suspension in humans. *Allergy & Asthma Proceedings*. 2015;36(1):48-57.

74. Giuliani A, Balducci AG, Zironi E, Colombo G, Bortolotti F, Lorenzini L, et al. In vivo nose-to-brain delivery of the hydrophilic antiviral ribavirin by microparticle agglomerates. *Drug Delivery*. 2018 Jan 1,;25(1):376-87.
75. Shah SA, Dickens CJ, Ward DJ, Banaszek AA, George C, Horodnik W. Design of Experiments to Optimize an In Vitro Cast to Predict Human Nasal Drug Deposition. *Journal of Aerosol Medicine and Pulmonary Drug Delivery*. 2014 Feb 1,;27(1):21-9.
76. Hallworth GW, Padfield JM. A comparison of the regional deposition in a model nose of a drug discharged from metered serosel and metered-pump nasal delivery systems. *Journal of Allergy and Clinical Immunology*. 1986 /02/01;77(2):348-53.
77. Pu Y, Goodey AP, Fang X, Jacob K. A Comparison of the Deposition Patterns of Different Nasal Spray Formulations Using a Nasal Cast. *Aerosol Science and Technology*. 2014 Aug 12,;48(9):930-8.
78. Dayal P, Shaik MS, Singh M. Evaluation of different parameters that affect droplet-size distribution from nasal sprays using the Malvern Spraytec. *Journal of Pharmaceutical Sciences*. 2004 Jul;93(7):1725-42.
79. Hosseini S, Wei X, Wilkins JV, Fergusson CP, Mohammadi R, Vorona G, et al. In Vitro Measurement of Regional Nasal Drug Delivery with Flonase,[®] Flonase[®] Sensimist,[™] and MAD Nasal[™] in Anatomically Correct Nasal Airway Replicas of Pediatric and Adult Human Subjects. *Journal of Aerosol Medicine and Pulmonary Drug Delivery*. 2019 Dec 1,;32(6):374-85.

80. Inthavong K, Yang W, Fung MC, Tu JY. External and Near-Nozzle Spray Characteristics of a Continuous Spray Atomized from a Nasal Spray Device. *Aerosol Science and Technology*. 2012 Feb;46(2):165-77.
81. Leach CL, Kuehl PJ, Chand R, McDonald JD. Nasal Deposition of HFA-Beclomethasone, Aqueous Fluticasone Propionate and Aqueous Mometasone Furoate in Allergic Rhinitis Patients. *Journal of Aerosol Medicine and Pulmonary Drug Delivery*. 2015 Oct 1;28(5):334-40.